Venus Cloud Structure and Radiative Energy Balance of the Mesosphere

Von der Fakultät für Elektrotechnik, Informationstechnik, Physik
der Technischen Universität Carolo-Wilhelmina
zu Braunschweig
zur Erlangung des Grades einer
Doktorin der Naturwissenschaften
(Dr.rer.nat.)
genehmigte
Dissertation

von Yeon Joo Lee
aus Seoul, Republik Korea

Bibliografische Information der Deutschen Nationalbibliothek

Die Deutsche Nationalbibliothek verzeichnet diese Publikation in der
Deutschen Nationalbibliografie; detaillierte bibliografische Daten
sind im Internet über `http://dnb.d-nb.de` abrufbar.

1. Referentin oder Referent: Prof. Dr. Andreas Hördt
2. Referentin oder Referent: Prof. Dr. Agustin Sánchez-Lavega
eingereicht am: 08. Februar 2012
mündliche Prüfung (Disputation) am: 12. April 2012

Cover image credits:
Venus Express (upper right image) – ESA
Venus in the ultraviolet (lower left image) – ESA/MPS/DLR/IDA
Printed in Germany

Vorveröffentlichungen der Dissertation

Teilergebnisse aus dieser Arbeit wurden mit Genehmigung der Fakultät für Elektrotechnik, Informationstechnik, Physik, vertreten durch die Mentorin oder den Mentor/die Betreuerin oder den Betreuer der Arbeit, in folgenden Beiträgen vorab veröffentlicht:

Publikationen

Lee, Y.J., D.V. Titov, S. Tellmann, A. Piccialli, N. Ignatiev, M. Pätzold, B. Häusler, G. Piccioni, P. Drossart, Vertical structure of the Venus cloud top from the VeRa and VIRTIS observations onboard Venus Express, Icarus, 217, 2, 599–609 (2012)

Tagungsbeiträge

Lee, Y.J., Venus cloud structure and radiative energy balance in mesosphere (Oral), IMPRS S3 seminar, 18 January 2012, Katlenburg-Lindau, Germany (2012)

Lee, Y.J., Latitudinal trend of thermal emission in the Venus cloud layer (Oral), TU Braunschweig, 25 October 2011, Braunschweig, Germany (2011)

Lee, Y.J., D.V. Titov, N. Ignatiev, S. Tellmann, M. Pätzold and G. Piccioni, Meridional trend of thermal emission and cooling rate in the Venus cloud layer (Poster), EPSC-DPS 02-07 October 2011, Nantes, France (2011)

Titov, D.V., N. I. Ignatiev, A. Piccialli, I. Khatuntsev, **Y.J. Lee**, S. Tellmann, S. Limaye, W.J. Markiewicz, G. Piccioni, P. Drossart, M. Pätzold, B. Häusler, Cloud morphology and atmospheric dynamics from the Venus Express observations (Presented by Titov), JpGU 27-28 May 2011, Japan (2011)

Lee, Y.J., D.V. Titov, N. Ignatiev, S. Tellmann, M. Pätzold and G. Piccioni, Thermal fluxes and cooling rate of the Venus cloud layer (Poster), EGU General Assembly 05-09 April 2011, Vienna, Austria (2011)

Lee, Y.J., Radiative energy balance in the Venus cloud layer (Oral), IMPRS S3 seminar, 16 February 2011, Katlenburg-Lindau, Germany (2011)

Lee, Y.J., D.V. Titov, S. Tellmann, G. Piccioni, A. Piccialli, M. Pätzold and P. Drossart, Upper cloud vertical structure and its effects on radiative energy balance (Oral), VIRTIS team meeting 30 November–1 December 2010, Paris, France (2010)

Lee, Y.J., D.V. Titov, S. Tellmann, G. Piccioni, A. Piccialli, M. Pätzold and P. Drossart, Vertical structure of the Venus cloud top from the VeRa and VIRTIS observations onboard Venus Express (Oral), International Venus Conference 20-26 June 2010, Aussois, France (2010)

Lee, Y.J., Radiative energy balance in the Venus atmosphere (Oral), TU Braunschweig, 11 May 2010, Braunschweig, Germany (2010)

Lee, Y.J., D.V. Titov, S. Tellmann, G. Piccioni, A. Piccialli, M. Pätzold and P. Drossart, Vertical structure of the Venus cloud tops from the joint analysis of the VeRa and VIRTIS observations onboard Venus Express (Oral), EGU General Assembly 02-07 May 2010, Vienna, Austria (2010)

Lee, Y.J., D.V. Titov, S. Tellmann, G. Piccioni, A. Piccialli, M. Pätzold and P. Drossart, Vertical structure of the Venus cloud tops from the joint analysis of the VeRa and VIRTIS observations onboard Venus Express (Oral), Venus Monitoring Camera Science Team Meeting #5 29-30 April 2010, Katlenburg-Lindau, Germany (2010)

Lee, Y.J., D.V. Titov, S. Tellmann, G. Piccioni, A. Piccialli, M. Pätzold and P. Drossart, Vertical structure of the Venus cloud tops from the joint analysis of the VeRa and VIRTIS observations onboard Venus Express (Oral), VeRa team meeting 18-19 March 2010, Bonn, Germany (2010)

Lee, Y.J., Radiative energy balance in the Venus atmosphere (Oral), IMPRS S3 seminar, 25 November 2009,Katlenburg-Lindau, Germany (2009)

Lee, Y.J., D. Titov, A. Piccialli, VeRa and VIRTIS teams, Vertical structure of the Venus cloud tops from the joint analysis of the VeRa and VIRTIS observations (Oral), VIRTIS meeting 9-10 November 2009, Brussels, Belgium (2009)

Lee, Y.J., D. Titov, A. Piccialli, VeRa and VIRTIS teams, Vertical structure of the Venus cloud tops from the joint analysis of the VeRa and VIRTIS observations (Presented by Dr. Titov), VIRTIS meeting 28-29 October 2009, Liege, Germany (2009)

Lee, Y.J., D.V. Titov, A. Piccialli, S. Tellmann, A. Migliorini, M. Pätzold, B. Häusler, G. Piccioni, P. Drossart, Vertical structure of the Venus cloud tops from the joint analysis of the VeRa and VIRTIS observations onboard Venus Express (Poster), EPSC 13-18 September 2009, Potsdam, Germany (2009)

Contents

Abstract

A dense cloud layer located at 50–75 km altitude completely covers Venus. The cloud aerosol consists mainly of sulfuric acid mixed with still unknown constituents. Due to their great opacity, the clouds play an important role in the radiative energy balance, the general circulation, and the atmospheric chemistry. The knowledge about the upper part of the clouds is especially important to understand the Venus mesosphere, because it is responsible for thermal cooling and solar heating that eventually results in the strongest retrograde zonal wind near the cloud tops in all altitudes. Remote observations have indicated significant temporal and spatial variations of the cloud structure that should affect radiative energy balance of the mesosphere.

This thesis investigates the upper cloud layer of Venus. Firstly, the vertical structure of the upper clouds and its variation with latitude are retrieved from the Venus Express observations. For this purpose, we have developed a new technique which uses temperature profiles from the radio science occultation experiment VeRa and thermal emission spectra in the 4.4–5.0 μm range collected by thermal infrared spectrometer VIRTIS. We implemented a comprehensive radiative transfer code including line-by-line calculations of gaseous opacities, and taking account for multiple scattering of aerosols. This study shows significant latitudinal trends in the upper cloud structure. Secondly, we investigated the influence of clouds, and their variability on the thermal fluxes and cooling rates calculated in a broad spectral range (50–2590 cm^{-1} or 3.86–200 μm). We developed and used an atmospheric model based on the derived parameters of the upper cloud and the observed temperature field. The clouds and gases, CO_2, H_2O, and SO_2, are considered as the most important opacity sources.

The highlights of the results are the following:

1. The structure of the upper cloud layer of Venus changes significantly with latitude. The cloud top altitude decreases from ~67 km at low latitudes to ~62 km in the polar regions, while the aerosol scale height decreases poleward from ~4 km to less than 1–2 km.

2. We found some particular cases of cloud top structure with very small aerosol scale height (≤1.0 km) and low cloud top (~63 km) in the "cold collar" region. Here, the position of the cloud top coincides with a sharp temperature inversion.

3. A comparison of the cloud top altitude derived in this work with those from previous studies at different wavelengths suggests the mean size of particles is larger in the upper cloud layer at high latitudes.

4. Thermal radiative energy calculations show strong cooling (>5 K/day on average) at and above the cloud tops, caused by thermal emission to space from the clouds and CO_2. Thermal emission from the lower atmosphere is absorbed by clouds. The thermal flux absorption by clouds results in thermal heating (~1 K/day) at the bases of lower and upper cloud layers.

5. Thermal cooling at the cloud tops is stronger at the pole (11 K/day) than at low latitudes (5–8 K/day).

6. The latitudinal trend of the total outgoing thermal flux shows a minimum (135 W/m^2) at the "cold collar", and maxima (154–164 W/m^2) at the pole and at the equator, in agreement with earlier studies.

7. A comparison between the thermal cooling rate derived in this study and the solar heating rate calculated by Tomasko et al. (1985) reveals a radiative energy unbalance in the mesosphere: heating prevails at low latitudes while cooling is dominant at the poles. A Hadley-type general circulation that transports heat from equator to pole is required to maintain the observed temperature field.

We suggest further studies. Since solar heating strongly depends on the cloud top structure, an accurate radiative energy balance requires new calculations of the solar heating fluxes for the same atmospheric model. In addition, the opacity of the middle and lower cloud layers strongly varies, as demonstrated by the VIRTIS/Venus Express observations. These variations need to be considered in future studies.

1   Planet Venus and its atmosphere

Venus has been familiar to humans as a morning or evening star over the world from prehistoric times. It is the third brightest celestial object, after the Sun and the moon, and its apparent magnitude reaches −4.6. Venus is always easy to find in the sky when the Sun is near the horizon and can be observed even during the middle of the day due to its brightness. Venus moves across the background stars, so the path of Venus was recognized and the observation of Venus was recorded from early times. The astronomical observation records on Venus were started from just after 3000 BC in Babylonian astrology, which is about the appearances of Venus in the sky and its influences on society (Cruikshank 1983). Other ancient documents about Venus were also found in Asia, Meso-America, and Greece. Ancient civilizations held Venus as an important symbol: the goddess of beauty and love (Babylonian, Greek and Roman), a guru which represents wealth, pleasure, and reproduction (Indian), or a metal star as one of the five basic elements (East Asian).

Despite a long history of observation of Venus, only little about the Venus atmosphere was known until the 20th century. The existence of the atmosphere of Venus was proven by Mikhail Lomonosov through the observation of a Venus transit across the Sun in the 18th century (Marov 2005), but Venus appeared as a featureless white disc in the visible wavelength range due to clouds. Thick cloud layers encircle the whole globe and lead to a high visible albedo. Our understanding of the Venus atmosphere has increased dramatically with the start of the Space Age. It was Mariner 2 that led the planetary exploration in 1962 (Colin 1983). Venera 4 acquired direct measurements for the first time with a lander in 1967. Pioneer Venus in 1978, the Venera series (5–16) from 1969 to 1985, and Vega 1 and 2 in 1985 followed, all with entry probes. The space missions provided fundamental information about the Venus atmosphere. In the mean time, in 1984, ground observations made it possible to monitor the deep atmosphere of Venus through the 2.3 μm near infrared (IR) atmospheric window, which was originated within the clouds (Allen and Crawford 1984, Marcq et al. 2006, Taylor 2006). It was found that there were huge variations of the Venus' middle and lower cloud features. Since then, other near-IR atmospheric windows have been discovered after, and they contain information on even deeper atmospheric layers (Meadows and Crisp 1996).

The reality of Venus was exposed by the descent probes of the spacecrafts. A 92 bar surface pressure, 737 K surface temperature, and thick sulfuric acid clouds in the 48–70 km altitude range are not the right conditions for human beings. Direct and remote observations have yielded estimates for atmospheric parameters like temperature and pressure profiles, wind profiles, solar and thermal flux profiles, aerosol particle distributions, chemical composition of the atmosphere, and so on. However, direct measurements obtained these parameters in the limited area without temporal sequence. Moreover, remote

Table 1.1: Summary of Pioneer Venus and Venera descent probes (Taylor 2006).

Atmosphere	
Surface pressure	92 bar
Surface density	~65 kg/m^3
Scale height	15.9 km
Total mass of atmosphere	~4.8×1020 kg
Average temperature	737 K (464°C)
Diurnal temperature range	~0
Wind speeds (surface)	0.3–1.0 m/s
Mean molecular weight	43.45 g/mol
Atmospheric composition (near surface, by volume)	
Major (%)	Carbon dioxide(CO_2) 96.5
	Nitrogen (N_2) 3.5
Minor (ppm)	Sulphur dioxide (SO_2) 150
	Argon (Ar) 70
	Water (H_2O) 20
	Carbon monoxide (CO) 17
	Helium (He) 12
	Neon (Ne) 7

sensing data revealed a striking temporal and spatial variability of the Venus atmosphere, and its meteorology presents us with unsolved physical problems. Examples are the zonal super-rotation with strong jets at the middle latitudes near the cloud top, the hemispheric vortices, the unknown ultraviolet (UV) absorber in the upper clouds, surface-atmosphere physical and chemical interaction, radiative energy balance, the cloud chemistry, etc. Many questions are addressed by earlier studies (Taylor 1998, Esposito et al. 2007, Svedhem et al. 2007) including about the comparison between Venus and Earth: how and why the two planets have their distinct characteristics (Svedhem et al. 2009). It requires intensive investigations to solve the unsolved questions on Venus atmosphere, and the needs are encountered the new observation from Venus Express. Venus Express, the first European space mission to Venus, has been monitoring the Venus atmosphere since April 2006. With its new data we try to understand Venus' cloud structure and the radiative energy balance.

1.1 The lower atmosphere of Venus (< 100 km altitude)

The Venus atmosphere can be divided into the upper atmosphere (>100 km altitude) and lower atmosphere (<100 km) (Schubert et al. 2007), according to the dominant atmospheric circulation. The upper atmosphere is dominated by subsolar-to-antisolar circulation driven by day/night insolation contrast (Lellouch et al. 1997). The lower atmosphere rotates in the zonal retrograde direction. The speed of the strong retrograde flow can reach more than 100 m/s at the cloud tops, and travels the globe in four Earth days, which is

60 times faster than the solid body rotation of the planet. This circulation is the one of the key dynamic features of the lower atmosphere, but its driving mechanism is unknown yet.

The composition of the lower atmosphere is mainly CO_2 (96.5%) and N_2 (3.5%), with small amounts of noble gases, Ar, He and Ne, and chemically active species, H_2O, CO, OCS, SO_2, HCl and HF (Table 1.1). This chemical composition coupled with the high atmospheric mass (~100 times larger than that of the Earth) results in a strong greenhouse effect in the lower atmosphere of Venus. This is mainly due to CO_2, which is an effective infrared (IR) radiation absorber. Venus does not have seasonal change due to its small obliquity (177.36°) and has very slow rotating solid body (one Venusian day equals to 243 Earth days). Therefore, the solar local time (for example, sub-solar point is local noon) is an important factor when considering the solar incoming radiance. The day/night temperature changes are pronounced in the upper atmosphere.

1.1.1 Temperature structure

The temperature profile of the Venus lower atmosphere is shown in Fig. 1.1. The figure shows the temperature decreasing with altitude, from 737 K at the surface to 120 K at
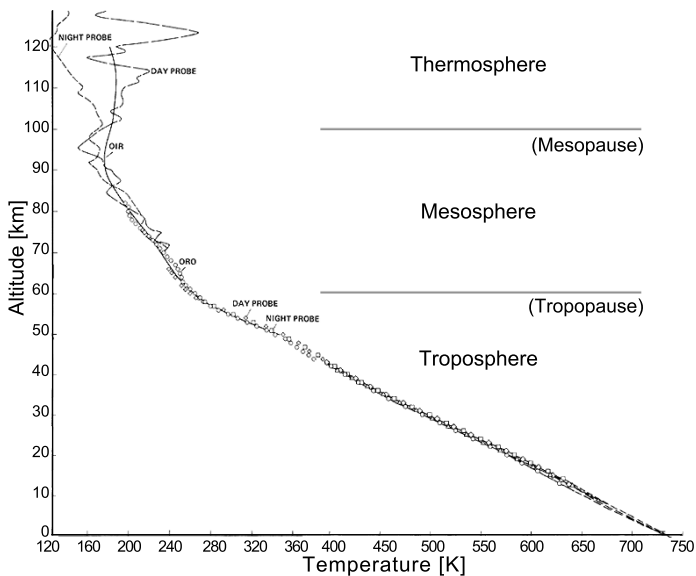
Figure 1.1: Vertical temperature profile of Venus (Seiff et al. 1985). Above 40 km altitude, temperatures were measured at 30° latitude by the night and day probes of Pioneer Venus, and Pioneer Venus orbiter radio occultation (ORO) and infrared sounding (OIR). Below 40 km, temperatures were measured by the four Pioneer Venus Probes. The altitudes of troposphere, mesosphere, and thermosphere are indicated.
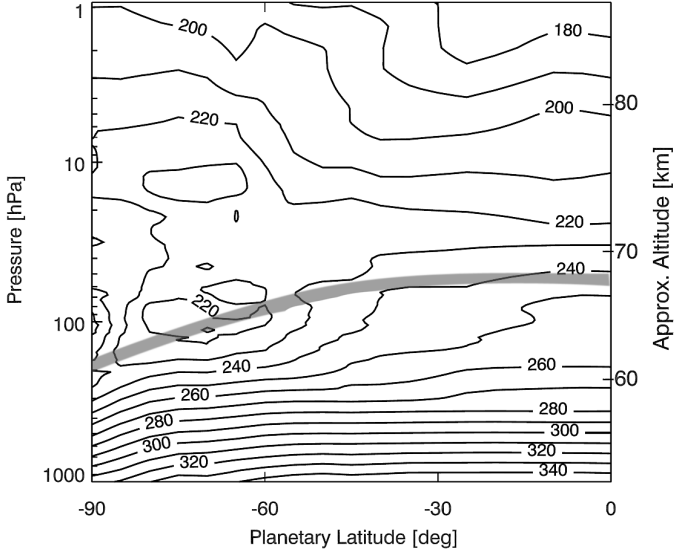
Figure 1.2: Global averaged temperature field (K) during night time (local time range is 22:30–05:00) from 12 temperature profiles observed by the Venus Express radio science experiment (VeRa) during the third occultation season (day of year (DOY) 116–146 2007) (Tellmann et al. 2009). The approximate cloud top altitude is marked as a gray solid line (Lee et al. 2012).

120 km altitude. The lower atmosphere of Venus can be divided into two regions. The lowest region, from the surface to the upper cloud layer (60 km altitude), is the troposphere (Fig. 1.1) with a steep lapse rate of ~10 K/km. In the upper troposphere, the lower and middle cloud layers are located in the 48–60 km altitude range. Convection dominates in this region. The upper region, from the upper cloud layer to 100–110 km altitude, is the mesosphere (Fig. 1.1). The unknown UV absorber in the upper cloud layer absorbs almost half of the incoming solar energy. Here, UV radiation is a dominant driver of chemical reactions. The lapse rate in the mesosphere decreases from ~8 K/km to ~4 K/km with increasing altitude (Pätzold et al. 2007). There is the thermosphere above 100–110 km altitude.

The thermal structure of the upper troposphere and mesosphere changes as a function of altitude and latitude as shown in Fig. 1.2. The temperature in the deep atmosphere is almost constant horizontally from equator to around 50° latitude, and slowly decreases to the poleward direction. There is a significant variation with latitudes above 60 km altitude. The temperature field in the 60°–80° latitude region at 60–70 km altitude has a most striking feature, a strong temperature inversion called the "cold collar". The cold collar shows an increasing temperature with altitude (see, Fig. 2.9). The temperature at the bottom of the cold collar is up to 30 K colder than the equator at the same altitude. Adiabatic

heating at around 70 km altitude caused by descending flow is supposed to be the origin of the temperature inversion at the cold collar, but the mechanism has not been uncovered yet (Tellmann et al. 2009). The temperature profile in polar region is quasi-isothermal at 65–75 km altitude. Another peculiar aspect of the thermal structure is the increasing temperature toward the poles in the 75–90 km altitude range. This temperature versus latitude field has been observed consistently over several decades by the Pioneer Venus Orbiter Infrared Radiometer and the Radio Occultation, the Infrared Fourier Spectrometer Experiment of Venera 15, radio occultation experiments of Venera 9, 10, 15 and 16, the Galileo Near-Infrared Mapping Spectrometer, the Magellan radio occultation, and the Venus Express radio science experiment (Seiff et al. 1985, Lellouch et al. 1997, Tellmann et al. 2009).

1.1.2   Cloud layers

Cloud layers and hazes are located in the transition region between troposphere and mesosphere. They extend down to 30 km and up to 90 km altitude, with the main cloud deck located in the 48–70 km altitude range (Esposito et al. 1983). The tropopause overlaps with the upper boundary of the middle cloud layer (~60 km). Different chemical processes can be distinguished across the tropopause: 'photochemistry' above the tropopause, where photon-driven processes are important, and 'thermochemistry' below, where thermal processes and vertical transport are important (Esposito et al. 1983).

In-situ measurements of the Pioneer Venus cloud particle size spectrometer (LCPS), and the Venera 9, 13, 14 and Pioneer Venus nephelometers allow us to divide the cloud structure into upper, middle, and lower cloud layers (Knollenberg and Hunten 1980). Figure 1.3 displays the vertical structure of the Venus cloud layers as number density, extinction coefficient, and mass loading profiles (Knollenberg and Hunten 1980). There are two planetary transition levels at 56 and 50 km altitudes, dividing the cloud deck into the upper, middle, and lower cloud layers: 'T_{um}' for the upper transition region and 'T_{ml}' for the lower transition region, respectively. In the upper cloud layer, the number density, extinction coefficient, and mass loading profiles show maxima at around 60 km altitude, and decreases gradually above and sharply below. The middle cloud layer has the number density increasing with decreasing altitude, while the extinction coefficient and mass loading are almost constant for the entire layer. The lower cloud layer has almost the same particle number density as the upper cloud layer, but much higher extinction coefficients and mass loading due to the presence of large size particles ("mode 3") (Knollenberg and Hunten 1980).

The cloud particles have a diameter ranging from less than 1 μm to over 30 μm. The upper cloud layer has a bimodal size distribution with a dominant 1-μm size particle. The middle and lower cloud layers have a trimodal size distribution with the two modes existing in the upper cloud layer and an additional larger sized mode (Knollenberg and Hunten 1980, Pollack et al. 1980b). There is a strong confirmation of the composition of 75% H_2SO_4 and 25% H_2O for the intermediate size cloud particles, "mode 2" ($\bar{r}$~1.05 μm), in the upper cloud layer (Ragent et al. 1985, Mills et al. 2007). The composition of the smaller, "mode 1" ($\bar{r}$<0.2 μm), and the bigger size particles, "mode 3" ($\bar{r}$~3.8 μm) are uncertain (Ragent et al. 1985, Taylor 2006). There is a controversy concerning mode 3 particles: are they solid or liquid? This controversy started when direct evidence was found

for asymmetric (possible crystalline) particles (Knollenberg and Hunten 1980). However, the evidence for solid particles were indirect, although LCPS detected large size particles, and there were internal inconsistencies in the LCPS measurements as well as inconsistencies between the LCPS measurements and measurements made by other instruments (Mills et al. 2007). Moreover, the temperature in the middle and lower clouds are too warm for ices of H_2SO_4 to be stable. Another cloud constituent must be considered for the crystalline mode 3 particles (McGouldrick et al. 2011).

There is a cycle of oxidation of SO_2 to H_2SO_4 followed by condensation, subsidence, evaporation, and decomposition. The primary sulfur species in the Venus atmosphere is SO_2. From the lower atmosphere, SO_2 is transported upward and becomes the source for H_2SO_4. H_2SO_4 is mostly produced in a thin layer of 2 km depth near the cloud top via photochemistry reactions,

$$CO_2 + SO_2 + h\nu \longrightarrow CO + SO_3,$$
$$SO_3 + H_2O \longrightarrow H_2SO_4. \tag{1.1}$$
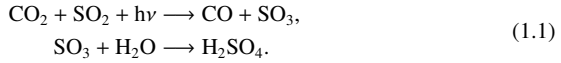
H_2SO_4 forms aerosols in the cloud layers by condensations. These aerosols are transported by the meridional circulation to the polar region where they descend into the lower atmosphere. Thermodynamic equilibrium reactions in the lower atmosphere decompose H_2SO_4, and turn H_2SO_4 back to SO_2 (Mills et al. 2007).
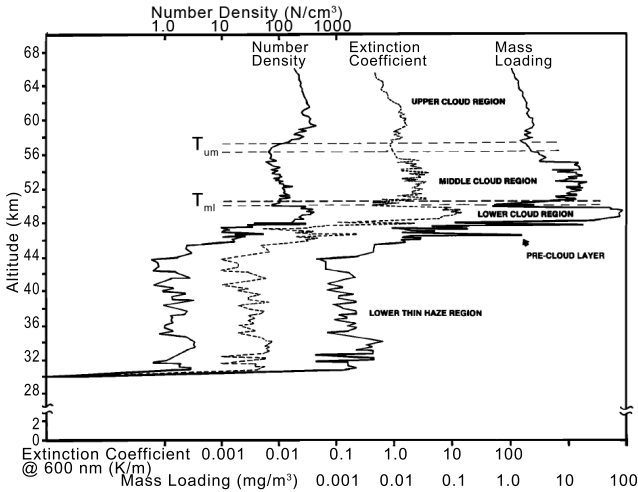
Figure 1.3: Vertical structure of Venus' cloud layers from direct computations based on the Pioneer Venus Cloud Particles Size Spectrometer (LCPS) data (Knollenberg and Hunten 1980). The transition boundaries between the upper and middle cloud layers, T_{um} (about 1 km thickness), and between the middle and lower cloud layers, T_{ml} (several hundred meters thickness), are shown. The extinction coefficient and mass loading profiles are based on the assumption of spherical particles with a density of 2 g/cm^3.

UV dark features in the clouds were discovered in the 1920s (Taylor 2006). The UV contrasts are due to inhomogeneous spatial/vertical distribution of the unknown UV absorbers in the clouds. Figure 1.4 shows a striking variability in the brightness and morphology of the cloud tops at UV wavelengths (Titov et al. 2008), from dark at low latitudes through bright and uniform at mid-latitudes to dark in the polar region. The UV absorber has not yet been identified (Mills et al. 2007). Absorption is observed in the upper cloud layer at wavelengths longward of 320 nm. UV absorption by SO_2 and SO cannot account for these features. Several candidates (S_8, S_3 and S_4, $FeCl_3$, and so on) have been suggested, but they could not explain the phase angle dependence of the UV dark markings, short lifetime of UV absorber (from hours to days) and the solar flux absorption in the 58–62 km altitude range (Mills et al. 2007).

There is a general similarity of main cloud features over the globe, with a stratiform cloud deck that extends over 20 km thickness vertically. However, the optical depth varies from place to place both vertically and horizontally due to the balance between the transport, and the production and loss processes of cloud materials (Ragent et al. 1985, Taylor 2006). The upper boundary of the cloud deck decreases toward the poles, but the lower boundary of the entire cloud deck is sharp and almost constant at the low and middle latitudes (Ragent et al. 1985, Taylor 2006, Ignatiev et al. 2009). The middle cloud layer overlaps with unstable region against to generally stable atmosphere (Seiff et al. 1985, Zasova et al. 2007). Radio science observations by Venus Express show there are the shallow convective layers in the ~52–54 km altitude range, and their thickness increase from 5 km in the equatorial region to 10 km at the poles (Tellmann et al. 2009).

1.1.3   Atmospheric dynamics

In the early 1960s, Earth-based observations detected a large scale albedo feature in the UV images, known as the dark horizontal 'Y'-feature that rotates around the planet in a period of 4–5 Earth days. Its presence implies a retrograde zonal rotation (westward) of the cloud level atmosphere with a 100 ± 10 m/s wind velocity, the so-called 'superrotation' or 'strong retrograde zonal wind'. This is a surprisingly high speed compared to the slow rotation of the solid body of Venus, around 2 m/s (Taylor 2006). The Venera and Pioneer Venus probes measured the vertical profiles of zonal flow (westward wind), as shown in Fig. 1.5(a). A westward wind is the predominant mode of atmospheric circulation at all altitudes from ~10 km to the clouds. The wind velocity is increasing with altitude, from near the surface toward the clouds. The maximum speed of the zonal wind occurs near the cloud tops, and the wind decelerates sharply above the clouds. The decrease of wind speed above the cloud tops is related to the thermal structure. There is a temperature gradient in the 70–95 km altitude range (above the cloud tops), 15–20°C warmer at the poles than at the equator. This thermal structure results in the pressure gradient, which is sufficient to decelerate the zonal winds completely by 85–90 km altitude (Taylor 2006). Strong zonal wind at the cloud top and deceleration above clouds are in agreement with the cyclostrophic flow which the pressure gradient sustains the centripetal acceleration and is balanced with the centrifugal force under the condition of negligible friction and Coriolis force (Holton 1992, Piccialli 2010).

Mariner 10, Pioneer Venus, Galileo, Venus monitoring camera (VMC) and VIRTIS onboard Venus Express, and ground-based observations have all shown large scale UV
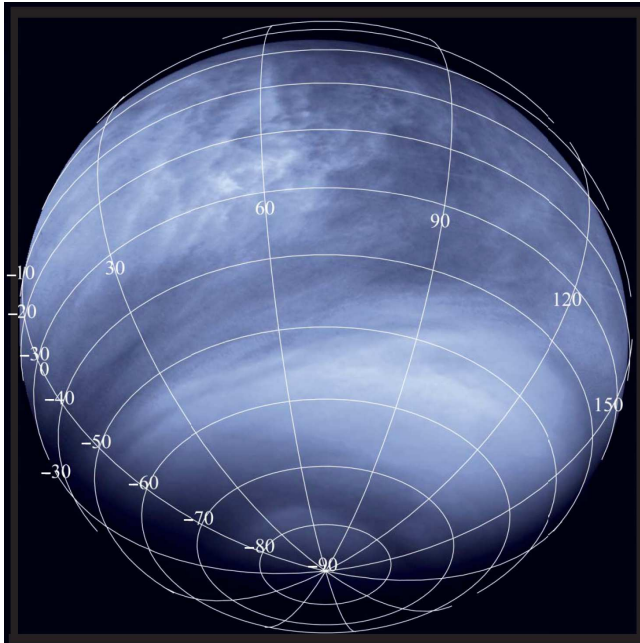
Figure 1.4: Variable features of Venus cloud top in the UV (0.365 μm) as seen at ~30,000 km distance by the VMC (Venus Monitoring Camera), on board Venus Express (Titov et al. 2008). The unknown UV absorber within the upper clouds produces the UV contrast.

markings below 50° latitude for several decades (Schubert 1983, Taylor 2006, Markiewicz et al. 2007b). Tracking the motions of UV markings has been used to detect wind velocities at the cloud tops (Markiewicz et al. 2007b). Spacecraft data is suitable to yield a latitudinal distribution of the zonal wind due to the high spatial resolution (Limaye 2007). Flyby spacecrafts (Mariner 10 in 1974 and Galileo in 1990), the Pioneer Venus Orbiter, which tracked clouds for nine years, and the Venus Express VIRTIS and VMC reveal the cloud top level circulation (Limaye 2007, Sánchez-Lavega et al. 2008). Figure 1.5(b) shows latitudinal wind profiles at three cloud levels. The zonal velocity at the cloud tops (around 66 km altitude) is almost constant at 90–110 m/s from the equator to the middle latitudes, and quickly decreases toward the poles (Markiewicz et al. 2007b, Sánchez-Lavega et al. 2008). A similar latitude dependence of the zonal flow is found at lower altitudes. The zonal winds at the bottom of the upper cloud layer (~61 km) and at the base of lower cloud layer (~47 km) have a nearly constant speed of ~60 m/s, from the equator to the middle latitudes. Toward the South Pole, the zonal winds in the cloud deck diminish in speed to almost zero.

Several possible mechanisms are discussed to explain the superrotation. Angular mo-
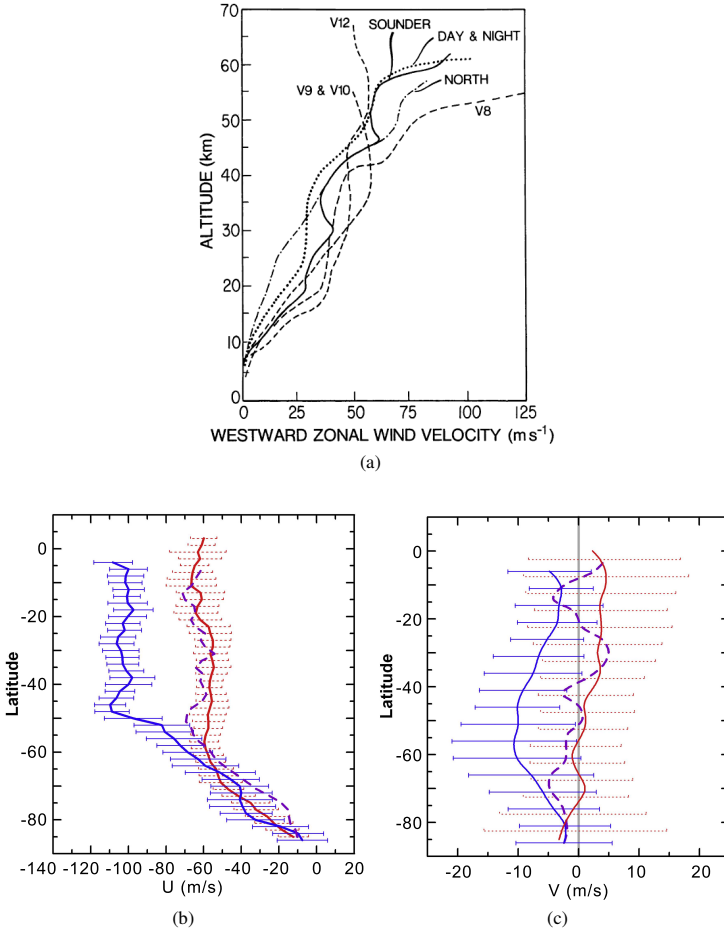
Figure 1.5: (a)Vertical wind profiles from Doppler tracking of Venera 8, 9, 10 and 12 (V8, V9, V10, V12), and interferometric tracking of Pioneer Venus entry probes (Sounder, Day & Night, North) (Schubert 1983). (b) Averaged zonal wind profiles at three cloud levels as a function of latitude: blue – 380 nm (corresponds to ~66 km altitude), violet – 980 nm (~61 km), and red – 1.74 μm (~47 km). (c) The meridional wind velocity profile as a function of latitude for the same three wavelengths as (b). (b) and (c) were measured from the visible and infrared spectrometer (VIRTIS) onboard Venus Express observations using cloud tracers (Sánchez-Lavega et al. 2008).

mentum delivered to the atmosphere from the solid body of the planet is suggested as the acceleration source of the atmospheric circulation to upward direction. This explanation is reasonable because of the same direction of the zonal flow as the rotation of the planet for the entire altitude. Cyclostrophic balance prevails to maintain the atmospheric rotation in nonequatorial regions, and the mean meridional circulation and planetary-scale waves may be involved in sustaining the zonal flow (Schubert 1983). Thermal tides have also been suggested as a source of wind acceleration (Taylor 2006, Schubert et al. 2007). However, no global circulation model simulation has been able to completely replicate the observations, and the true mechanism is still unknown yet (Schubert et al. 2007).

The mean meridional velocities (Fig. 1.5(c)) at around 61 km and 47 km altitudes do not show conclusive latitudinal trends. However, the meridional velocity at the cloud tops peaks at ~10 m/s at 55°S and decreases to zero at equator and pole. This result agrees with the recent reanalysis of Pioneer Venus data (Limaye 2007, Sánchez-Lavega et al. 2008). The poleward motion at 66 km altitude is related to the upper branch of a Hadley cell (Gierasch et al. 1997). Hadley circulation is the simplest form of circulation that can occur in a planetary atmosphere: heated air rises at the equator, travels to high latitude, cools down at the poles, and then descends at there. Hadley circulation leads to a pole-to-equator flow near the surface, and an equator-to-pole flow at higher altitudes. The Hadley regime can exist as a global size single cell in the Venus atmosphere because of the small Coriolis force. On Earth, Hadley circulation breaks down at around 30° latitude due to the Earth's spin (Taylor 2006). The expected Hadley cell for Venus has not been observed directly (Gierasch et al. 1997, Esposito et al. 2007), although there are strong indications of that through poleward wind at the cloud top levels (Esposito et al. 2007). A Hadley cell transports momentum vertically from lower altitudes to higher altitudes, and horizontally from low latitudes to the poles. Therefore, a possible Hadley cell would be related to the superrotation and polar circulation, including the polar vortex. Adiabatic heating and cooling due to vertical motions of Hadley cell can be the reason for the temperature structures of the cold collar and for the reversed equator-pole temperature gradient (Taylor et al. 1997, Taylor 2006, Esposito et al. 2007).

IR and UV observations have revealed bright vortices over each pole, which are symmetric, and showed spiral bands. However, it is difficult to determine the vertical extent of this structure (Markiewicz et al. 2007b, Piccioni et al. 2007). The vortex eye is located between the poles and 70° latitude and is surrounded by a UV-dark ring (Titov et al. 2008), and it has a quasi-oval shape eye, or rarely an elongated 'S' shape eye, which is known as a polar dipole. There are similarities between Earth's tropical cyclones and Venus' polar vortex, such as an inward flow toward the center, a large vertical extent, a jet of zonal wind existing near 70° latitude, dipole features or swirls within the eye, and the presence of transverse waves extending radially outward from the center (Limaye 2007, Limaye et al. 2009). However, the physical scale of the Venus polar vortex is much larger (~12,000 km radial size, compared to less than 1,000 km for the largest tropical cyclones), and the lifetime of the polar vortex is much longer (it has been observed since 1974). The longevity of the polar vortex is caused by that it being situated over the pole, which means the vortex never loses its energy source because it is traveling with the steering winds (Schubert et al. 2007). Several mechanisms of the origin of the polar vortex are discussed. The zonal momentum transported from lower to higher latitudes by Hadley cell may generate rapidly rotating descending air, and form the polar vortex (Tay-
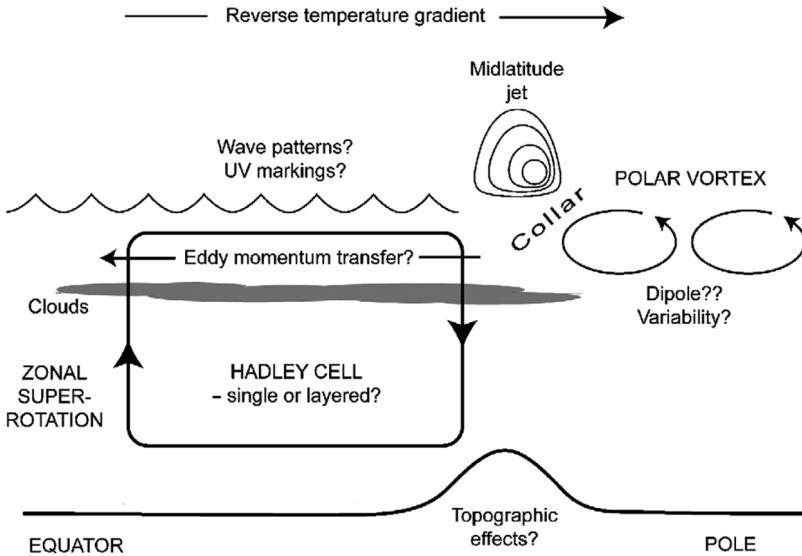
Figure 1.6: A schematic view of the main features of atmospheric circulation of Venus (Taylor 2006).

lor 2006). Or, the heat sources for the polar vortex could be the solar energy deposition in the dayside cloud layer and thermal energy deposition from hot surface in lower altitudes (Limaye 2007). We need more observations to understand the vertical structure and the mechanism of the polar vortex on Venus.

Figure 1.6 displays the main features of the atmospheric circulations from the equator to the pole: superrotation, Hadley circulation, and the polar vortex. Open questions are given in the figure. Also, a general circulation model that incorporates realistic radiative transfer schemes, cloud dynamics, and chemistry, is necessary to identify missing elements in current simulation that fail to reproduce the observed superrotation.

1.1.4 Radiative energy balance in the mesosphere

Venus is the second nearest planet to the Sun: its mean orbital distance is 0.722 AU. Venus receives almost twice the solar flux received by Earth (2622 ± 6 W/m^2 versus 1368 ± 3 W/m^2) (Moroz et al. 1985). Notwithstanding the high solar flux, the thick clouds of Venus' atmosphere reflect most incoming solar radiance back into the space, absorbing only ~24% of solar flux. Moroz et al. (1985) estimate the integral Bond albedo as 0.76. As a result, the outgoing emission corresponds to a black body around 230 K as the mean effective temperature ($\bar{T}_e$) for the radiative energy balance in the planetary atmosphere. $\bar{T}_e$ satisfies the equation

$$4\sigma \bar{T}_e^4 = S(1 - A) \tag{1.2}$$
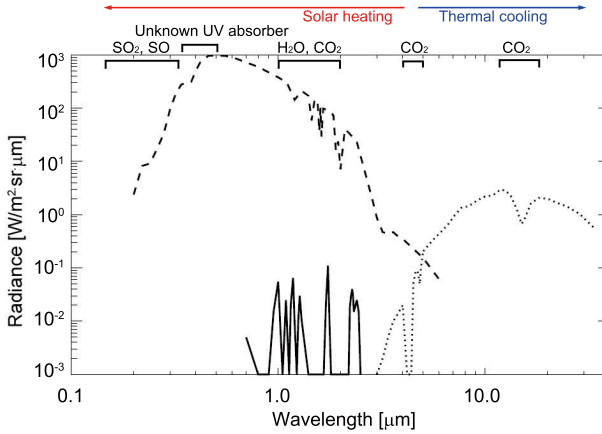
Figure 1.7: The mean spectra of Venus as seen from space (Titov et al. 2007). The reflected solar radiance (dashed line), the thermal emission from the cloud tops and mesosphere (dots), and the night side emission from the lower atmosphere (solid line) are compared.

where σ is the Stefan-Boltzmann constant, S is the solar flux at the mean orbital distance of Venus, and A is the integral Bond albedo. Figure 1.7 shows the general view of the Venus spectrum as seen from space. This spectrum shows absorption features due to several sources: SO_2 and SO gases above the cloud tops absorb solar radiation below $0.32\,\mu m$ wavelengths, the unknown UV absorber absorbs in the 0.32–$0.50\,\mu m$ wavelength range at the cloud tops, CO_2 and H_2O absorb at near infrared wavelengths between 1 and $2\,\mu m$, and H_2SO_4 cloud aerosols absorb at wavelengths longer than $2.5\,\mu m$ (Mills et al. 2007, Titov et al. 2007). The reflected solar radiance becomes comparable with thermal radiance in the 4–5 μm range, and thermal emission dominates at wavelengths over 5 μm.

The thermal emission of Venus atmosphere is close to the temperature of the cloud tops ($\sim$230 K), which is much cooler than the surface temperature ($\sim$735 K). This is in agreement with a classical assumption in the meteorological literatures (Goody and Yung 1989). The strong CO_2 bands at 4.3, 4.8 and 15 μm induce significant absorption features above the cloud tops in thermal emission spectrum (Fig. 1.7). The high temperature of the deep atmosphere and the surface below the cloud decks emits the thermal radiation even in the 1–5 μm wavelength range. Although absorptions by atmospheric gases and clouds are strong, this thermal emission leaks from lower altitudes to space through atmospheric windows. Figure 1.7 shows how the thermal emission originated in the deep atmosphere, below the cloud deck, is presented in the spectrum. These near-IR atmospheric windows were discovered in 1980s (Allen and Crawford 1984), and have been used to investigate the deep atmosphere down to the surface (Svedhem et al. 2009). However, these observations can only be made on the night side of Venus because the thermal emissions are four orders of magnitude weaker than the reflected solar radiance.

The absorbed solar flux of Venus is 157 ± 6 W/m^2 averaged over the whole globe (Mo-
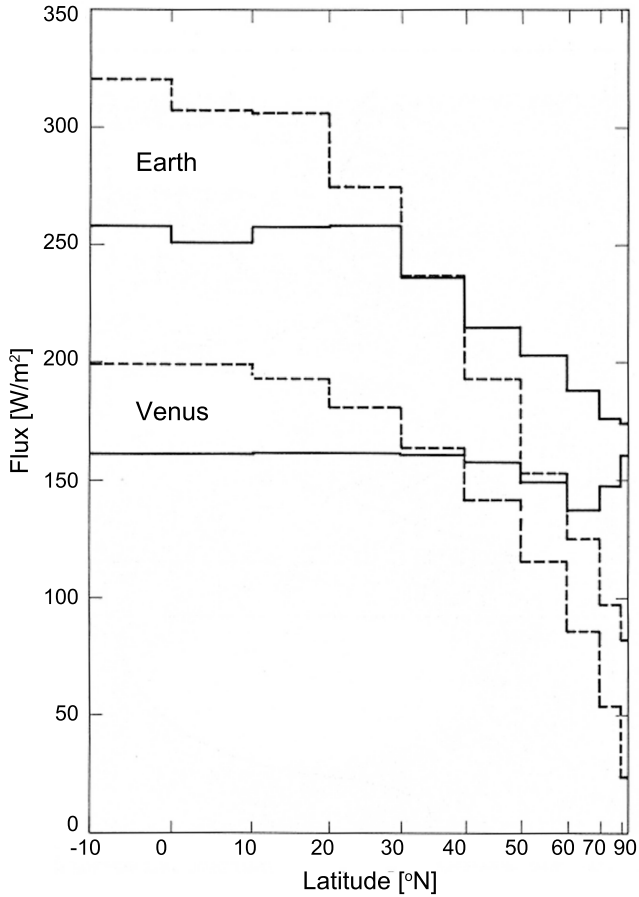
Figure 1.8: Latitude dependence of the zonally averaged thermal flux of Venus (solid line), absorbed solar flux (dashed line) assumed a homogeneous albedo of 0.762, and an incident solar flux of 2642 W/m^2. Corresponding curves of the thermal flux (solid line) and absorbed solar flux (dashed line) of Earth are given for comparison (Schofield and Taylor 1982).
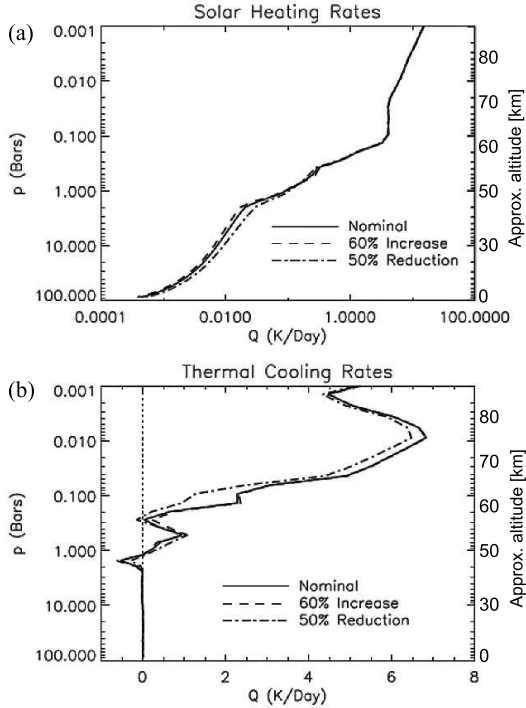
Figure 1.9: Globally averaged (a) solar heating and (b) thermal cooling rate. This vertical profiles are calculated based on the nominal aerosol optical depth (solid line), 60% increased middle and lower cloud aerosol optical depth (dashed line), and 50% reduced middle and lower cloud aerosol optical depth (dashed-dot line) (Crisp and Titov 1997). The nominal aerosol model used the equatorial cloud top level (28 mbar) with three cloud layers, the upper (58–71 km), middle (50–58 km) and lower (48–50 km) cloud (Crisp 1986).
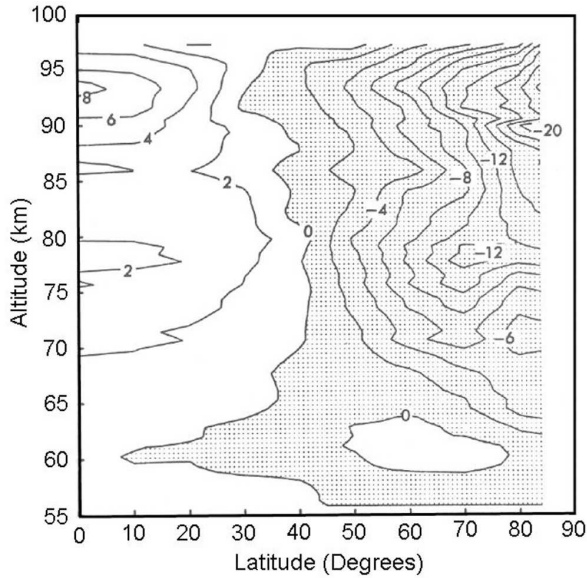
Figure 1.10: The net radiative heating rate (a difference between thermal cooling rate and solar heating rate) in [K/day]. The region where thermal cooling exceeds solar heating is indicated by the shaded area. These calculations are based on the Pioneer Venus OIR experiment data (Crisp 1989).

roz 2002). Due to high albedo, it is even less than that of Earth (240 W/m^2, the Earth albedo being ~26%). The distribution of solar flux absorption is a monotonic decreasing function of latitude, being largest at the equator and least at the pole. Figure 1.8 shows that both Earth and Venus receive the largest solar flux at the equator with decreasing trends in poleward direction. A remarkable difference between Venus and Earth is how the thermal emission varies with latitude. The thermal emission of Venus is almost constant at low latitudes, decreases quickly at the cold collar, and increases at the pole. The thermal emission of Earth is almost constant at low latitudes, decreasing from middle latitudes to the pole with a smaller slope than the absorbed solar flux is. This behavior implies that the lower atmosphere of Venus stores incoming solar energy, which is latitude dependent, and distributes it well over the latitudes through atmospheric dynamics (Schofield and Taylor 1982, Titov et al. 2007). Most of the incoming solar flux on Venus is reflected, and the remainder is absorbed by UV absorbers and gases in the atmosphere (~21%). Only ~3% of solar flux is absorbed by the surface. The unknown UV absorbers in the upper cloud layer are the most effective absorption source of solar radiation in the Venus atmosphere. Almost 50% of the total solar energy is deposited in the upper cloud level. This results in a solar heating rate of around 8 K/day [1] in the 60–70 km altitude range, as shown in

---

[1] 'Day' is equal to the Earth day (24 hours).

Fig. 1.9(a). The absorbed solar energy in the upper cloud layer generates thermal tides, which can support the superrotation by momentum fluxes (Zasova et al. 2007, Schubert et al. 2007). The heating rate decreases sharply downward of the upper cloud layer, and becomes negligible below the clouds. Here, the thermal cooling rate is comparable to the solar heating rate below the clouds (Fig. 1.9(b)), both being near to zero. However, solar heating overwhelms thermal cooling above the cloud tops at low latitudes (Fig. 1.10). The thermal cooling rate shows a peak around the cloud tops, $\sim$7 K/day, and decreases below. Cloud aerosols are an important source for both IR extinction and scattering. Also considering its spatial variability of opacity, a cloud can cause significant variation in the thermal radiative forcing within and below cloud levels (Crisp 1989, Titov et al. 2007). Figure 1.9 shows that opacity changes in the middle and lower cloud layers can modify both solar heating and thermal cooling rates, but the thermal cooling rate is twice more sensitive to this than solar heating. Far above the cloud tops, CO_2 induces both thermal cooling and solar heating rate in the upper mesosphere (Crisp 1986, 1989).

Figure 1.10 shows the net radiative heating in the Venus mesosphere. The unbalance of radiative energy in the mesosphere introduces radiative heating by $\sim$8 K/day at the equator and radiative cooling by $\sim$20 K/day in the polar region. The radiative energy unequilibrium needs another mechanism to maintain observed temperature field, by cooling the atmosphere up to 8 K/day at the equator mesosphere and by warming it up to 20 K/day at the polar mesosphere. Vertical motion of a pole-to-equator meridional circulation can support this mechanism: air rises at the equator (adiabatic cooling) and subsides at the pole (adiabatic warming) (Crisp 1989, Titov et al. 2007).

The thermal emission in the deep atmosphere is strongly affected by the greenhouse effect. The large thermal opacities by CO_2 and H_2O maintain the high surface temperature, which is almost 500 K higher than the mean effective temperature for the radiative balance. Pollack et al. (1980a) calculated how the surface temperature would increase when removing each opacity source of the atmosphere, and found that the key opacity sources are CO_2, H_2O, clouds, SO_2, CO, and HCl, ranked in the order of importance. CO_2 decreases the surface temperature most, by 463 K, followed by H_2O (218 K), clouds (113 K), and SO_2 (52 K). There are small contributions from CO (13 K) and HCl (0.1 K) to the greenhouse effect. A similar test had been done by Bullock (1997), who showed a decrease of the surface temperature: 423 K by CO_2, 143 K by clouds, 69 K by H_2O, 12 K by OCS, 3 K by SO_2 and CO, and 2 K by HCl. The absorption bands of these components may overlap each other; therefore, the accumulated greenhouse effect is much larger than 500 K. It should be noticed that the calculations considered only the change of opacity, and neglected possible actual effects on atmosphere. For example, removing SO_2 may result in the disappearance of clouds because it is a major component of cloud particles. Also, the competition between albedo and greenhouse forcing needs detailed calculations (Titov et al. 2007).

1.2 The goal of the thesis

This thesis is focusing on the upper cloud layer in the Venus mesosphere. The upper clouds of Venus are intriguing not only because of the variable opacities and physical properties revealed by observations, but also because of the strong connection to radiative

energy balance and atmospheric dynamics. The upper cloud layer dominates the solar energy deposition by absorption and reflection, as well as determines the outgoing thermal flux. The uneven energy deposition in this level becomes an energy source to support the superrotation, the polar vortex, and the Hadley-like meridional global circulation. This circumstance results in that the cloud tops are very crucial altitudes to understand the radiative energy balance and the mechanism of atmospheric dynamics. This motivates the retrieval of the upper clouds structure from the most recent observations of Venus Express. We developed a new technique which uses the joint analysis of the thermal IR spectrometer and the radio science experiment onboard Venus Express. We merged the fast line-by-line gaseous absorption calculation and the radiative transfer model to obtain a synthetic spectrum in the 4.4-5.0 μm wavelength range. Through this method, the upper cloud structures as a function of latitude are retrieved (Lee et al. 2012). This result has been taken for the thermal flux calculation. We calculate in particular thermal emissions in the 0–99 km altitude range for the broad band (3.86–200.0 μm or 50–2590 cm^{-1}), and demonstrate the sensitivities of thermal emission to the cloud top structures. Then, we calculate the thermal cooling rates as a function of latitude and altitude based on the observed temperature field. The results allow a better understanding on how the radiative effects of the latitude dependent clouds influence to the lower mesosphere.

The thesis content is as the following:

Chapter 1 provides the background knowledge on the lower atmosphere of Venus: thermal structure, clouds, atmospheric dynamics, and radiative energy balance. Unsolved questions in each topic are addressed. The aim of the thesis is described at the end.

Chapter 2 shows how the cloud top structures are retrieved. We develop a joint analysis of the spectrometer and the radio science experiment onboard Venus Express. For the methodology, a radiative transfer model is merged with a line-by-line method. The detailed algorithm, sensitivity tests results, and the latitudinal distribution of the cloud top parameters are shown.

Chapter 3 describes methods and databases for the thermal flux calculation over a broad band. The atmospheric thermal structure and cloud models are developed to consider the deep atmosphere of Venus. The databases of gaseous absorption and the merged routine of the line-by-line method and radiative transfer model are improved from Chapter 2 for more accuracy, and expanded to consider the full infrared range and increased parameters of aerosols and gaseous extinctions.

Chapter 4 presents the results of model calculations concerning the thermal emission of Venus' lower atmosphere, from a monochromatic radiance spectrum to a wavenumber-integrated thermal cooling rate profile. We evaluate the radiative effects of the different gas constituents and various cloud top structures, and calculate the sensitivity of thermal flux and cooling rate to the cloud top structures. The thermal radiative forcing is calculated with the latitudinal upper cloud structure from Chapter 2.

Chapter 5 gives the radiative energy balance which compares the thermal cooling rate obtained from Chapter 4 and a solar heating rate from Tomasko et al. (1985). We discuss about cloud variability, atmospheric dynamics, and climates, which are related with the radiative energy balance. The effects of clouds and gases on the planetary atmospheres are addressed. We finish with a summary and further studies.

2 Structure of the upper clouds from Venus Express observations

The upper cloud layer of Venus is an important region to estimate the radiative energy balance and to monitor dynamic circulation patterns. An unknown ultraviolet (UV) absorber in the upper cloud layer absorbs almost half of the solar flux received by the planet (Esposito et al. 2007), and induces the cloud top levels to the major place of solar radiation absorption. In parallel with solar heating, the cloud tops reflect around 80% of the incident solar radiation (Crisp and Titov 1997) and the temperature of the cloud tops determines the outgoing thermal flux. Since solar and thermal radiation play dominant roles in the chemical and dynamical processes of the Venus atmosphere, the knowledge about the structure of the upper cloud layer is of fundamental importance to understand the physics of the Venus atmosphere. The lower atmosphere of Venus is in a state of retrograde circulation. There are strong zonal winds with speeds over 100 m/s, so-called 'superrotation', which is very rapid for the slow solid body rotation of the planet ($\sim$2 m/s). The maximum speed of superrotation occurs near the cloud tops where the UV markings originate. Cloud tracking through UV contrasts has been used for the wind speed retrieval (Markiewicz et al. 2007b), but we have poor knowledge of the altitude where they form (Titov et al. 2008).

This part introduces a new technique to analyze the vertical structure of the upper cloud layer. It uses a joint-analysis of observations from Imaging spectrometer (VIRTIS) and radio science instruments (VeRa) onboard Venus Express. A radiative transfer model has been merged with line-by-line calculations for this retrieval. Below we describe the results and make comparisons with previous studies.

2.1 Venus Express mission and payloads

Venus had been explored by 25 spacecrafts in 1960–90, with ambitious scientific and technical achievements. The results, however, have raised many questions about past, present, and future of Venus, which may yield further insight into the evolution of the terrestrial planets in general (Titov et al. 2006, Svedhem et al. 2009). Venus Express, the first European mission to Venus, opened an opportunity to investigate Venus with a wealth of data. The spacecraft is acquiring data since April 2006 and is still orbiting Venus in good condition. There are seven instruments in the payload, categorized into three different observation types: spectrometers and spectral imagers for remote sensing, plasma and magnetic field instruments for in-situ measurements, and the ultrastable oscillator used for radio science. The imaging spectrometer (VIRTIS) and radio science instruments
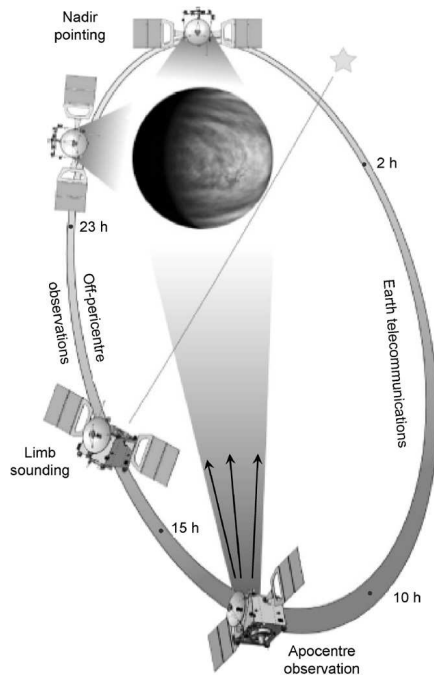
Figure 2.1: Sketch of Venus Express orbit (Markiewicz et al. 2007b). Main types of observation along its orbit period are marked.

(VeRa) provide the infrared spectrum and thermal structure data, respectively. These are essential data for the investigation about Venus mesosphere, and are used in this study. Simple descriptions of onboard instruments now follow based on Svedhem et al. (2009) and bibliographies of each instrument.

VIRTIS Visible (0.27–1.1 μm) and infrared (1.05–5.2 μm) medium resolution imaging spectrometers and an infrared (1.8–5.0 μm) high resolution imaging spectrometer (Drossart et al. 2007).

VeRa Radio science instrument to determine the temperature and the density of 40–90 km altitude range, and to determine electron density in the ionosphere by means of radio occultation of the telemetry signal (Häusler et al. 2006).

VMC Wide angle CCD camera with UV, visible, and infrared (365, 513, 965, and 1000 nm) narrow band filters (Markiewicz et al. 2007a).

SPICAV/SOIR Three spectrometers provide thermal profiles and composition in the upper atmosphere through observation in stellar and solar occultation mode (Bertaux et al. 2007).

PFS High spectral resolution double pendulum spectrometer with a short wave (0.9–5.5 μm) and a long wave (5.5–45 μm) channel. However, it failed to operate due to mechanical problem (Formisano et al. 2006).

ASPERA In-situ plasma and neutral energetic atoms detector combined with an ion mass analyzer, neutral particle imager, neutral particle detector, and electron spectrometer (Barabash et al. 2007).

MAG Dual sensor fluxgate instrument with the main sensor mounted on the tip and an auxiliary sensor mounted on the foot (Zhang et al. 2006).

Venus Express has a highly elliptical polar orbit. Its altitude approaches 250 km altitude in pericenter ($\sim$78°) and is as high as 66,000 km in apocenter (Fig. 2.1). According to position of the orbit, the science observation mode changes during its 24 hr orbit period. Around the apocenter (10–14 h) the full Venus disk is in the field of view, and this phase is used for global mapping. The observations from the apocenter to off–pericenter (15–23 h, the ascending branch) are of key importance for atmospheric dynamic and cloud evolution analysis. Around the pericenter (23–1 h) it is possible to have high spatial resolution observation and occultation measurements. The descending branch of the orbit (2–12 h) is reserved for telecommunication and data downlink (Titov et al. 2006, Svedhem et al. 2009). This orbit offers good global coverage and optimizes each instrument measurement from long duration to close-up studies, and complements Pioneer Venus, which had an equator pericenter (Svedhem et al. 2009). It has very good coverage especially in the southern hemisphere for latitude and solar local time, but limited coverage for the northern hemisphere. This is because there is more time to measure in the southern hemisphere where the satellite has a larger distance from the planet.

2.1.1   Visible and infrared thermal emission spectrometer: VIRTIS

VIRTIS has two channels and three focal planes (Piccioni et al. 2006). The mapping channel has two 2-D focal planes in the visible (VIRTIS-M-vis) and infrared (VIRTIS-M-IR). An additional spectroscopic channel has a single aperture with high spectral resolution in the 2–5 μm range (VIRTIS-H). VIRTIS-M has a field of view of 64 $\times$ 64 mrad, and the maximum pixel size is 0.25 $\times$ 0.25 mrad at a resolution of 256 $\times$ 256 pixels. Table 2.1 shows characteristics of VIRTIS channels in brief. The output of VIRTIS-M is described in Fig. 2.2. It can be considered as a large set of stacked monochromatic 2-D images along the wavelength axis (0.25–5 μm range) with moderate spectral resolution. VIRTIS-H has a high spectral resolution. Its field of view is centered in the VIRTIS-M image, corresponding to the green color line in the figure.

The large wavelength range of VIRTIS helps to address a number of scientific problems and find interesting features: dramatic images and video sequences of the south polar vortex, non-LTE emission patterns, profiles of abundance of several atmospheric gases, wind field maps, temperature profiles over the southern hemisphere, images of cloud structure at several altitudes and surface temperature and emissivity maps, and so on (Svedhem et al. 2009). The usage of VIRTIS output can be determined according to the observation mode of the spacecraft. The off-pericenter observation mode, which is
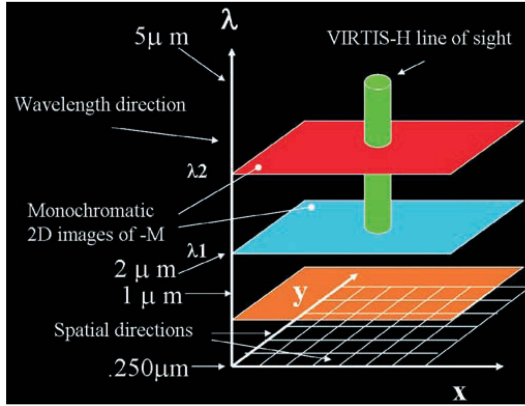
Figure 2.2: The concept of VIRTIS-M output, together with VIRTIS-H (Piccioni et al. 2006). The spatial direction is in the x-y plane, and the wavelength direction is the z-axis. Colored planes (red, light blue, and orange) represent monochromatic 2-D images of VIRTIS-M. The VIRTIS-H field-of-view centers in VIRTIS-M image at high spectral resolution in the small frame, which is displayed as a green cylinder.

the most intensively used, allows VIRTIS-M to perform spectral mapping at the best spatial resolution. In the apocenter observation mode, full disk of the southern hemisphere is available through 3×3 images. This mode is considered essential for the global dynamics as full atmospheric rotation is provided with repetition.

Figure 2.3 shows a radiance spectrum in the wavelength range from 1 to 5 μm on the night side. This infrared spectrum provides a wealth of information on the atmosphere from the surface to the mesosphere. The 3–5 μm range is sensitive to both temperature and cloud opacity variations (Piccioni et al. 2007). It approximately follows a Planck function of cloud top temperature, but also depends on the thermal structure above the clouds near the strong CO_2 bands at 4.3 and 4.8 μm. Radiation in the 1.18, 1.74, and

Table 2.1: VIRTIS characteristics

	VIRTIS-M-vis	VIRTIS-M-IR	VIRTIS-H
Spectral range (μm)	0.28–1.1	1.05–5.13	2–5
Spectral resolution $\lambda/\Delta\lambda$	150–500	100–500	1300–3000
Field of view (mrad × mrad)	64 (slit)×64 (scan)	64 (slit)×64 (scan)	0.44×1.34
Maximum spatial resolution (mrad × mrad)	0.25 (slit)×0.25 (scan)	0.25 (slit)×0.25 (scan)	-
Image size (pixels)	256×256	256×256	-
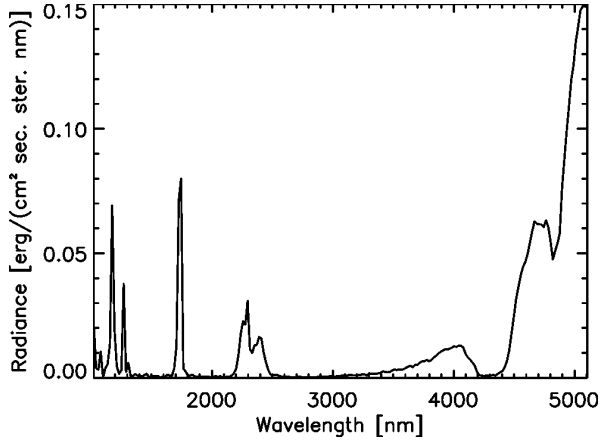
Figure 2.3: VIRTIS-M-IR spectrum example taken from the night side (Grassi et al. 2008)

2.3 μm atmospheric windows are emitted from below the cloud deck and even from the surface. These atmospheric windows are valuable for surface and atmospheric species abundance studies (Drossart et al. 2007).

Grassi et al. (2008) successfully retrieved vertical temperature profiles from VIRTIS-M-IR spectra in the 4.25–5 μm range. The initialization input for the radiative transfer calculation was assumed as a known quantity, and air temperature (T) was acquired in an iterative loop

$$T_l^{i+1} = T_l^i \frac{\sum\limits_{ch=1}^{m} \frac{T_{\mathrm{B},ch}(I_{\mathrm{observed},ch})}{T_{\mathrm{B}ch}(I_{\mathrm{expected},ch}^i)} W_{ch,l}}{\sum_{ch=1}^{m} W_{ch,l}}, \qquad (2.1)$$

where i, l, and ch represent the number of the cycle, pressure level index, and sampling channel, respectively. T_{B} is the brightness temperature derived from the radiance (I_{observed}, Appendix C) observed by VIRTIS and the modeled radiance (I_{expected}) is calculated from a current air temperature profile. W is the weighting function given by

$$W_{\mathrm{ch},l} = -\frac{\partial t_{\mathrm{ch}}}{\partial \log_{10} p}\bigg|_{p=p_1}, \qquad (2.2)$$

where p is the pressure at level l and t is the total atmospheric transmittance from space to the given pressure level (Zasova et al. 1999, Grassi et al. 2008). The atmosphere was modeled by a stack of 67 pressure levels (49–106 km). Cumulative errors, which were calculated from the average of the statistical population of retrieval errors, were below 1 K in the 66–77 km range, and increased outside this range (Grassi et al. 2008). Four example temperature profiles acquired on VIRTIS observations are shown in Fig. 2.4.
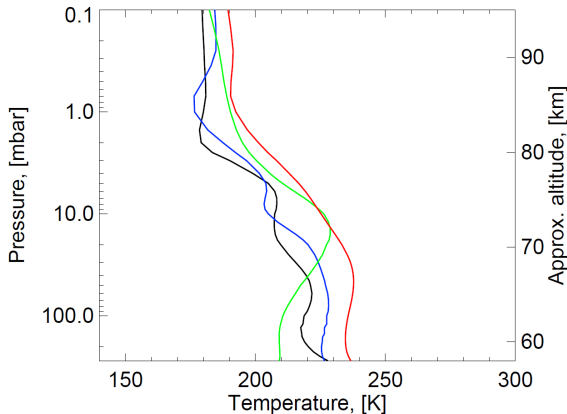
Figure 2.4: Retrieved temperature profiles from VIRTIS-M-IR spectra at four latitudes: 10°(black), 35°(blue), 65°(green), and 85°(red) (Piccialli 2010)

2.1.2   Radio science experiment: VeRa

The Venus Express Radio Science Experiment (VeRa) uses radio signals at 3.6 cm and 13 cm wavelengths to investigate the Venus atmosphere. This has provided an opportunity to use the same wavelength as the radar mission Magellan, a decade after it ended (Häusler et al. 2006). The neutral atmosphere and the ionosphere of Venus are sounded by VeRa during Earth occultation. During the ingress occultation experiment, the spacecraft passes behind the ionosphere, the neutral atmosphere, and it disappears behind the planetary disk as seen from the Earth; the spacecraft then re-emerges in the reverse sequence during the egress occultation. During these occultation events, gases are located between the radio source and receiver (Fig. 2.5). The gradient of refractive index of gas within the atmosphere and ionosphere changes the direction of propagation of the radio waves (Tellmann et al. 2009). This signal, which penetrated the Venus atmosphere, is recorded by ground stations using closed loop receiving technique. The signal properties and their changes as a function of time, together with accurate knowledge of the spacecraft orbit during occultation, enable one to retrieve vertical profiles of atmospheric density, pressure, and temperature in the range of 40–90 km in altitude.

Tellmann et al. (2009) calculated the degree of bending (α), the ray periapsis (r_0) and impact parameter (a), and the projection of the ray path onto the planetary surface, based on the assumption of local spherical symmetry. The refractivity of the atmosphere at the ray periapsis is optained from the bending angle via an Abel transform (Fjeldbo et al. 1971). The refractivity profile $\mu(h)$ is

$$\mu(h) = -C_3 \frac{N_e(h)}{f_o^2} + C_1 n(h) k_B, \tag{2.3}$$
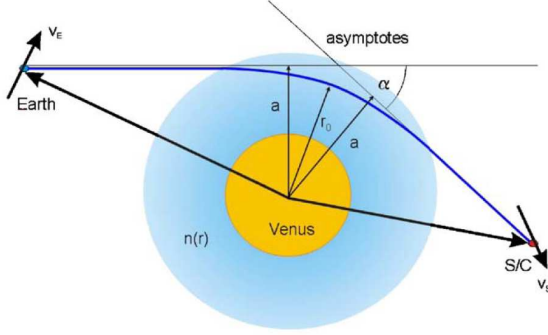
Figure 2.5: Sketch of ray bending (blue solid line) in the Venus atmosphere (Häusler et al. 2006). Deflection angle (α) is related to impact parameter (a) and index of refraction ($n(r)$). r_0 is the closest approach distance.

where h is the altitude, $N_e(h)$ is the electron density in the ionosphere, k_B is the Boltzmann constant, $n(h)$ is the neutral number density, f_o is the frequency of the radio signal, $C_3 = 40.31$ m^3/s^2, and $C_1 \approx 1312 \times 10^{-6}$ kms^2/kg for Venus atmospheric conditions. The first term in the right hand side is the contribution of the ionosphere, and the second term represents the atmospheric contribution, which is much stronger than the other in the neutral atmosphere below 100 km altitude. Therefore, Eq. 2.3 can be simplified into the below equation in the neutral atmosphere

$$\mu(h) = C_1 n(h) k_B. \tag{2.4}$$

Since the ideal gas law, $p(h) = k_B \cdot n(h) \cdot T(h)$, relates pressure to temperature and neutral number density, and the hydrostatic equilibrium assumption[1] is very accurate in well-mixed atmosphere, temperature and pressure vertical profiles can be derived directly from the following equations

$$T(h) = \frac{\mu_{up}}{\mu(h)} \cdot T_{up} + \frac{\bar{m}}{k_B \cdot n(h)} \int_h^{h_{up}} n(h') \cdot g(h') dh', \tag{2.5}$$

$$p(h) = \frac{1}{C_1} \mu(h) T(h), \tag{2.6}$$

where T_{up} equals $T(h_{up})$ as a boundary condition, $\bar{m}$ is the mean molecular mass of neutral atmospheric species, $g(h)$ is the acceleration of gravity, and all altitudes relate to the mean Venus radius of 6051.8 km. From 40 km to 90 km VeRa provides accurate temperature and pressure data sets at a high vertical resolution of a few hundred meters. The uncertainties are ~1 K and 0.1% for temperature and pressures, respectively. Altitudes below ~32 km are inaccessible to occultation measurement due to critical fraction of dense atmosphere (Tellmann et al. 2009).

---

[1]Gravity is balanced by a pressure gradient force ($\partial P/\partial z = -\rho g$).
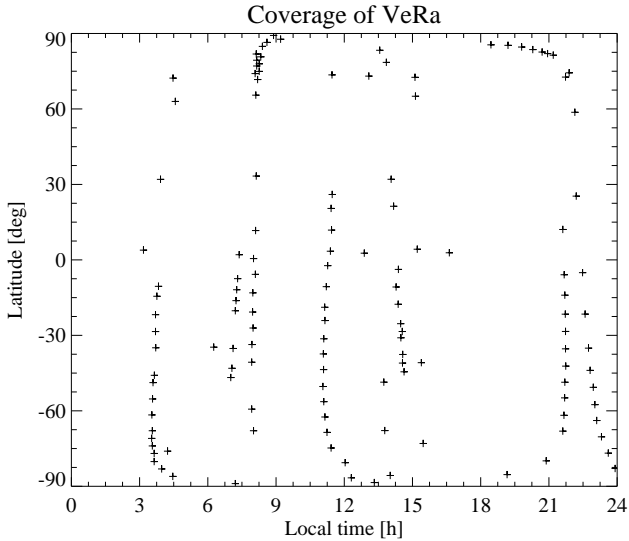
Figure 2.6: The coverage of VeRa radio occultation data in local time versus latitude.

VeRa coverage is shown in Fig. 2.6 for both hemispheres as a function of local time. The figure shows two years of observations from Jul. 2007 to Sep. 2009, and shows that the southern hemisphere has good coverage. Compared to the southern hemisphere, however, the northern hemispheric data is confined to the high latitude, with only a few observations distributed from the equator to ~60°N.

Figure 2.7 shows one example of VeRa measurements at high latitude between 40 km and 100 km altitude. There are cloud layers in the ~48–70 km range (blue gradient box), and radio science can detect atmospheric thermal structure without being affected by aerosols. Three profiles are derived with different upper boundary temperature conditions of 170 K, 200 K, and 230 K. These profiles merge below 90 km altitude, so the effect from the upper boundary is negligible below this level (Tellmann et al. 2009). This thermal profile gives clear evidence that the boundary between troposphere and mesosphere is located at around 60 km. The lapse rate is around 10 K/km from lower altitude up to the tropopause, and temperature is quasi-isothermal up to ~75 km. This temperature structure also shows two correlations with cloud structure. Firstly, the tropopause is considered to be the boundary between upper and middle cloud layers. The atmosphere is extremely stable above the tropopause. Secondly, within the upper cloud layer there are fine-scale temperature perturbations. This results from strong cloud influence on the thermal structure and stability, even well above and below the clouds (Tellmann et al. 2009).

Figure 2.7 also shows levels of unity optical depth in the 4.3–5.0 μm range that is used for the temperature profile retrieval from VIRTIS-M IR channels (Grassi et al. 2008). The calculation of temperature retrieval considered the presence of both aerosols and carbon
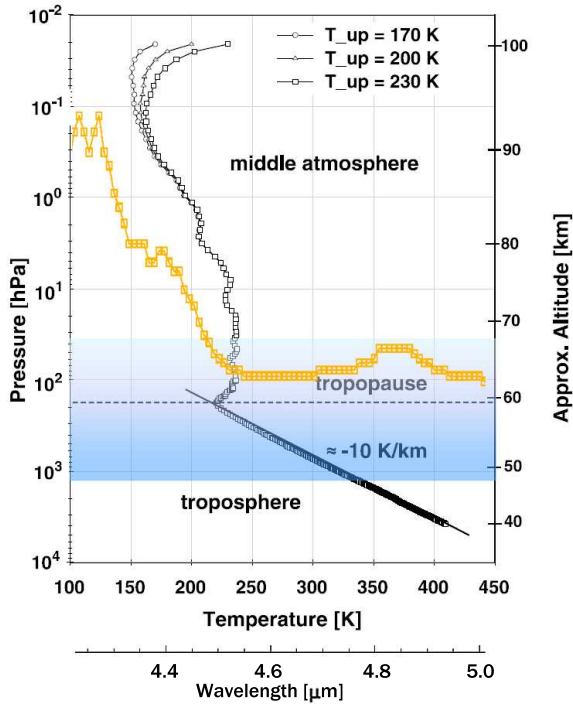
Figure 2.7: Temperature profiles (black) from the VeRa radio occultation measurement from DOY 150, 2007, at 85.85°N and local time 1550h (Tellmann et al. 2009). The altitude of unity optical thickness in the 4.3–5.0 μm range (orange) for typical Venusian conditions is also shown (Grassi et al. 2008). The cloud layer is represented by a blue gradient box.

dioxide at these levels (~64–95 km) in the VIRTIS 4.3–5.0 μm range of observation. Since this wavelength of VIRTIS cannot penetrate clouds, the VIRTIS spectra are originated from the cloud tops within the range where the levels of unity optical depth are located in the clouds. The difference of VIRTIS-M IR spectrum and VeRa radio occultation is revealed from the influence of the clouds on the data set; the VIRTIS spectrum contains the influence of the cloud top temperatures, but the VeRa radio occultation does not get effects from aerosols.

Summary

Venus Express is monitoring the atmosphere of Venus from 2006. The observational data obtained from the radio science experiment (VeRa) and the thermal infrared spectrometer (VIRTIS) onboard Venus Express provide an opportunity to investigate the upper troposphere and mesosphere. This study uses different properties of each observation: thermal

structure obtained from VeRa is independent of aerosol effects and the infrared spectrum from VIRTIS contains the atmospheric absorption amounts.

2.2   Upper cloud structure retrieval

This chapter will start with the motivation of this study, relating to the discrepancy between temperature profiles from VeRa and VIRTIS observations. Uncertainties about the variation of the upper cloud structure are the reason of this discrepancy. Based on the characteristics of each instrument, a joint-analysis method for VeRa and VIRTIS data is developed to retrieve the upper cloud structure. The detailed descriptions on data sets and methodology are followed.

2.2.1   Motivation and idea of approach
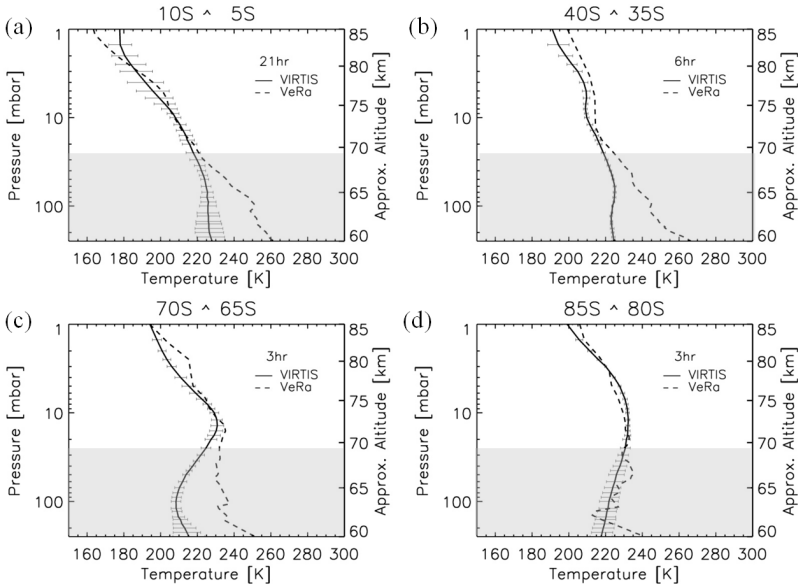
Figure 2.8: Comparison of temperature profiles derived from VIRTIS (solid line) and detected by VeRa (dashed line) in the same latitudinal bin and local time (shown in the right upper corner of each figure). (a) Low latitude case with VIRTIS orbit ♯824_07 and VeRa orbit ♯927, (b) middle latitude case with VIRTIS ♯634_03 and VeRa ♯641, (c) cold collar case with VIRTIS ♯664_04 and VeRa ♯665, and (d) polar region with VIRTIS ♯664_04 and VeRa ♯662 data. Clouds are indicated by a gray box.

Two experiments onboard Venus Express remotely sound the Venus mesosphere temperature. Thermal emission spectroscopy in the region of the 4.3 μm CO_2 band by VIRTIS

allows one to retrieve vertical profiles of atmospheric temperature in the altitude range from 90 km to the cloud tops (70–65 km) (Grassi et al. 2008, 2010). Radio-occultation sounding by the VeRa experiment penetrates deeper into the clouds down to an altitude of ~40 km (Tellmann et al. 2009). Comparing the results of the two remote sensing techniques reveals systematic differences in the deriving temperature structure below 70 km as shown in Fig. 2.8. Figure 2.8 compares selected temperature profiles from the two experiments for four local times and latitudinal zones. Below 70 km, where the cloud tops are supposed to be (gray boxes in the figures), the VIRTIS temperatures are systematically lower than those derived by VeRa.

The explanation for this fact can be twofold. Firstly, the observations by the two experiments are not simultaneous and co-located, so the difference can be due to temporal and spatial variations of the mesospheric temperature field. Secondly, the disagreement can be explained by the fact that the radio-occultation technique is not sensitive to the presence of clouds while thermal emission spectroscopy is. The retrieval of temperature profiles from VIRTIS spectra is based on an a priori assumption about aerosol structure and properties at the cloud tops (Grassi et al. 2008). Any uncertainties in the cloud model would affect the retrieved temperature profile. We note that, in general, thermal emission spectroscopy allows one to retrieve both temperature and aerosol structure in a self-consistent way. However, this requires a broad spectral range in which aerosol extinction varies significantly as in the case of the infrared Fourier spectrometer onboard Venera-15 (Zasova et al. 1993). VIRTIS covers only a narrow part of the Venus thermal emission spectrum (3–5 μm) that does not allow us to distinguish between temperature and aerosol effects on the emission spectra. Since the disagreement in the temperature structure derived from two experiments is systematic and correlates with the clouds, we conclude that the discrepancy is due to inaccuracy of the aerosol model used in the VIRTIS temperature retrievals.

The discrepancy discussed above motivated the development of a method of joint analysis to study the cloud top structure. The approach is based on radio-occultation technique providing atmospheric temperature profiles independent of aerosol properties, while thermal emission spectra depend on both temperature and cloud structure. This study uses the radio-science temperature profiles and fits the VIRTIS spectra by tuning parameters of the cloud top model. Since VeRa and VIRTIS cannot perform simultaneous observations, special attention was paid to selection of subsets of both observations in order to make them as close as possible in space and time.

2.2.2   Data sets

Input data sets for the atmospheric thermal structure have been taken from VeRa observations. Temperature profiles are grouped into ~5° latitudinal bins with latitudinal representativeness. VIRTIS spectra have been selected for comparison with synthetic spectra under the conditions: the same latitudinal bin with the temperature groups, short exposure time (<0.36 s), and restricted range of the emission angles.
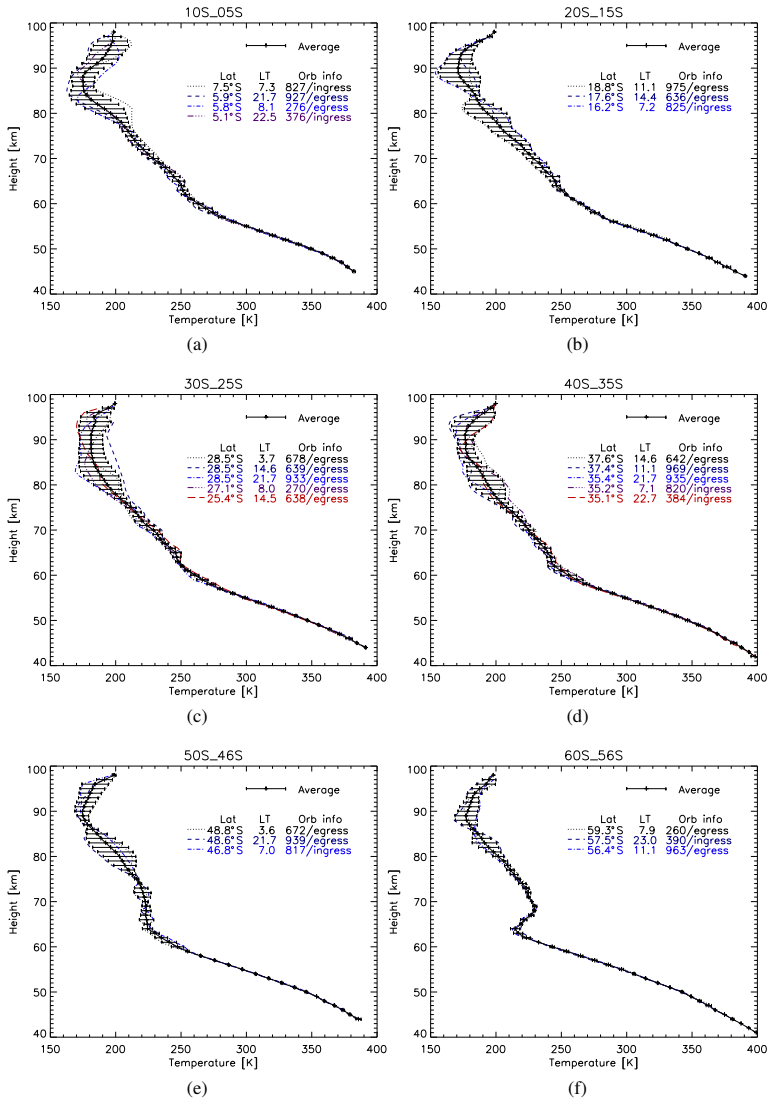
Figure 2.9: VeRa temperature profiles for every second latitude bin (figures on the top of each sub-plot). Individual observations are shown with their legends in the upper right corner. The thick black line and horizontal bars are the mean profile and standard deviation.

(g)

(h)

(i)

(j)
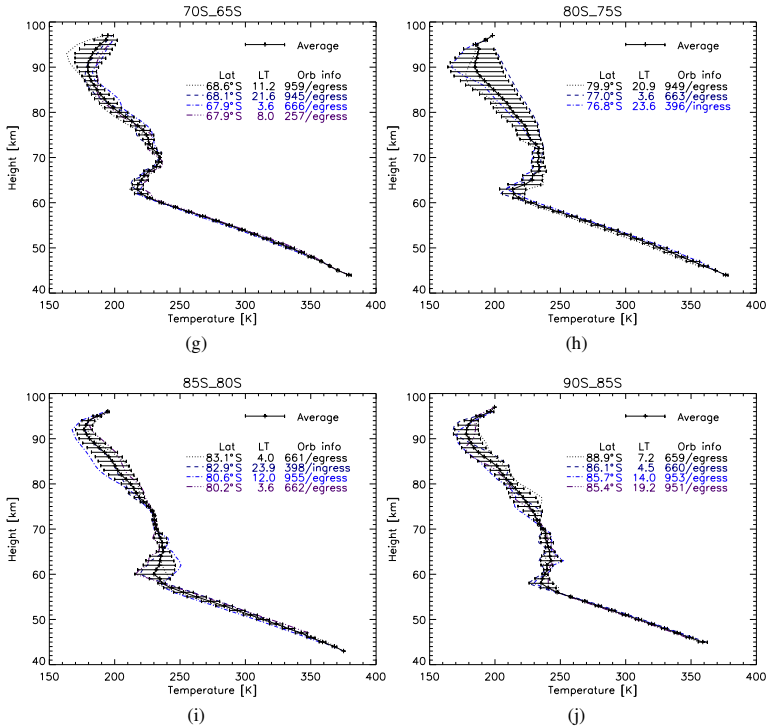
Figure 2.9: *(continued)*.

2.2.2.1 Temperature profiles from VeRa

VeRa performed more than 175 Earth occultation experiments from the beginning of the orbital mission in April 2006, resulting in more than 350 atmospheric profiles. They provide good latitudinal coverage in the Southern hemisphere. In the Northern hemisphere occultations are mainly clustered at high latitudes. The data set covers roughly all local times.

For this study we selected a sub-set of 113 VeRa temperature profiles taken in orbits ♯254 (2006-12-31) through ♯986 (2009-01-01), and distributed them into 5 degrees latitude bins (except 40°–46°S, 46°–50°S, 50°–56°S, and 56°–60°S bins, according to the depth and location of the temperature inversion layer). Since mesospheric temperatures depend mainly on latitude (Seiff 1983), we neglect local time dependence of the temperature field. This gives 2–8 VeRa observations in each bin. Our analysis is limited to the Southern hemisphere for two reasons: 1. VeRa coverage of Northern hemisphere is poor, especially between equator and 60°N, and 2. VIRTIS observations cover mainly the Southern hemisphere. Figure 2.9 shows individual and mean temperature profiles

(a)

(b)

(c)

(d)
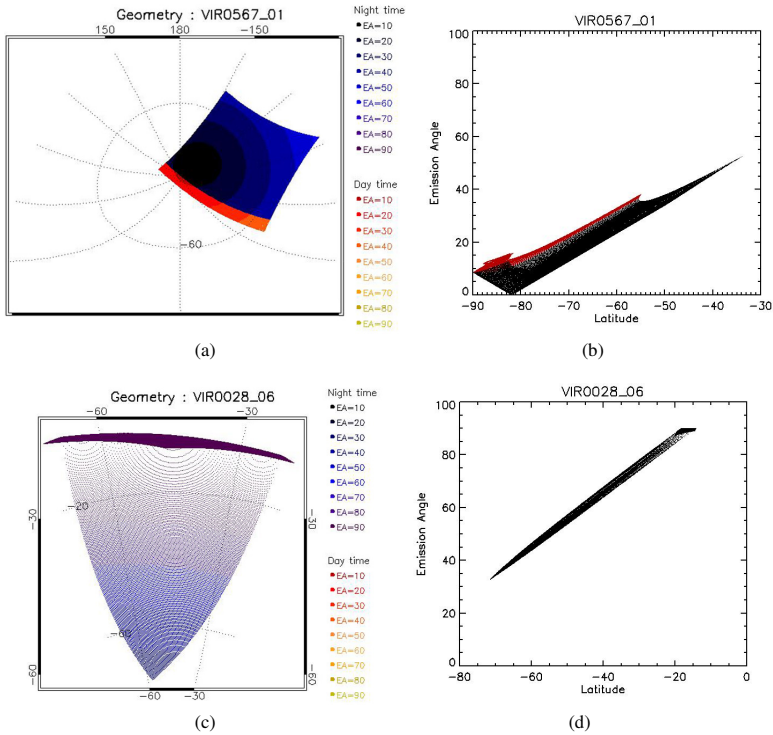
Figure 2.10: Geometry (left plots) and emission angle distribution (right plots) examples of VIRTIS-M-IR observations. (a) and (b) is obtained from ♯567_01 which is located above the polar region including terminator. (c) and (d) is obtained from ♯028_06 which is located at the middle latitude region of night side. Colors in (a) and (c) indicate 10° emission angle (EA) bins, and red points in (b) are from day side in (a).

for each latitude bin indicating strong variations with latitude. Atmospheric temperature monotonically increases with depth at low latitudes (<45°S). Middle and high latitudes up to ~80°S are characterized by temperature profiles with strong and sharp inversions at 60–65 km. Poleward from 80°S the temperature profiles are almost isothermal for 10–15 km above the tropopause, which approximately coincides with the cloud tops.

2.2.2.2   Infrared spectrum from VIRTIS

The 3–5 μm wavelength range has sufficient brightness temperature sensitivity to estimate the Venus cloud top thermal emission (Piccioni et al. 2007, Grassi et al. 2008). This study used only night side observations with less than 0.36 s exposure time to avoid contamination by detector saturation. We distributed the selected VIRTIS-M-IR spectra, collected
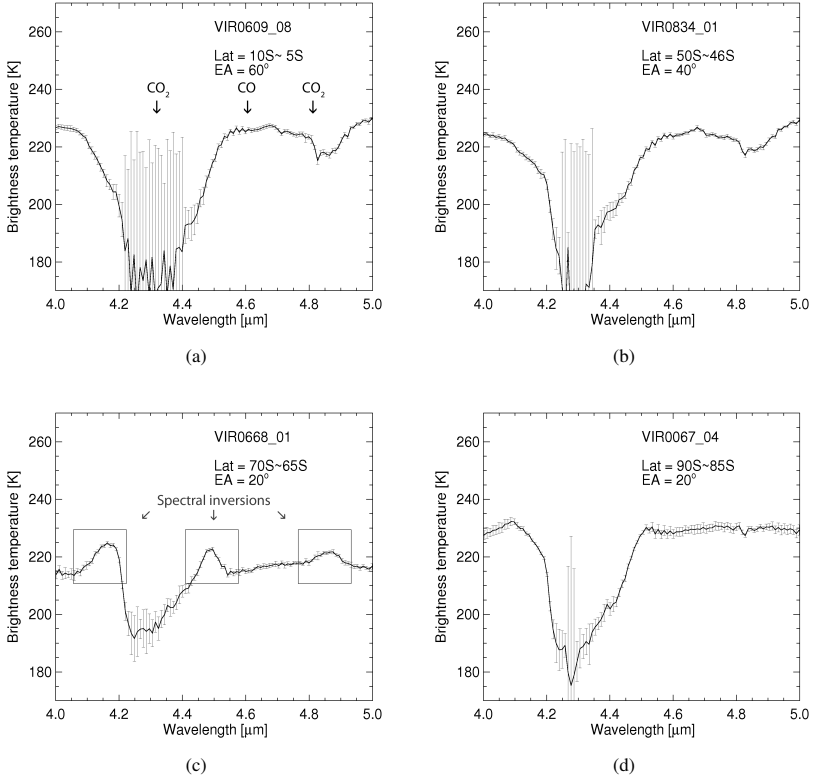
Figure 2.11: Examples of the VIRTIS-M-IR brightness temperature spectra around the 4.3 μm CO_2 band. VIRTIS data file labels, latitude bin (Lat) and emission angle (EA), are given in the legends in the upper right corner of each sub-plot. Solid lines and bars represent the mean and standard deviations within the selected group. The positions of gaseous absorption bands and spectral inversions are shown in panels (a) and (c), correspondingly.

till 27 October, 2008 (orbit ♯921), in ~5° size latitude bins, as for the VeRa temperature profiles (Fig. 2.9). Within each latitude bin the spectra were also grouped according to an emission angle. Figure 2.10 shows that the pixels of VIRTIS measurements in the polar region mostly have low emission angles, but those at the equator region have high emission angles due to their locations between the satellite and Venus. In this study we assumed that VIRTIS spectra are independent of local solar time. Thus, latitude and emission angle were two parameters used to group the spectra. The range of emission angle variations within each group was limited to ±0.1° around the median value. Therefore, each latitude bin contained 13–31 groups of spectra, and each group was averaged from 30 to 300 spectra according to the latitude bin and the emission angle range. The total number of VIRTIS spectrum groups included in the analysis is 252.

Figure 2.11 shows examples of the VIRTIS-M-IR spectra within selected latitude bins, with pronounced features typical of Venus emission spectra. In Figs. 2.11(a) and (b), the CO_2 bands at 4.2–4.4 μm and 4.8–4.9 μm are clearly seen "in absorption" as usual for a monotonic temperature profile. In the continuum outside of CO_2 bands (i.e. at ~4 μm, 4.6–4.7 μm, and ~5 μm) the spectrum is formed by emission from warm cloud tops, while inside the bands the spectrometer sees colder atmosphere above the clouds. Cold collar spectra show inversions in the "shoulders" of the 4.3 μm band at ~4.15 μm and ~4.5 μm, while the weaker 4.8 μm band appears "in emission" indicating temperature inversions right above the cloud tops (Fig. 2.11(c)). The most constant brightness temperature in the spectral range from 4.5 μm to 5 μm in Fig. 2.11(d) suggests the quasi-isothermal layer above the cloud tops. We note that the features in the VIRTIS spectra and their latitudinal changes (Figure 2.11) are in qualitative agreement with the temperature structure measured by VeRa (Fig. 2.9).

VIRTIS spectra show oscillations (for instance, at 4.5–4.6 μm in Fig. 2.11) caused by a slightly different sensitivity of odd and even lines of the detector that remain even after radiometric calibration (Gilli et al. 2009). In this work we used only odd lines which show more pronounced shape of the weak 4.8 μm CO_2 absorption band.

2.2.3   Radiative transfer modeling

The equation of transfer can be expressed with the extinction coefficient and the source function is

$$-\frac{1}{e_{v,\lambda}}\frac{dI_\lambda(P,\mathbf{s})}{ds} = I_\lambda(P,\mathbf{s}) - J_\lambda(P,\mathbf{s}), \qquad (2.7)$$

where I_λ is the radiance at P in the $\mathbf{s}$ direction, J_λ is the source function, and $e_{v,\lambda}$ is the volume extinction coefficient at λ wavelength. While it sets the pattern of the formalism used in transfer problems, its physical content is simple and can be written in any of the other notations (Goody and Yung 1989). Under the condition of an isotropic source and stratified atmosphere, the equation is modified into

$$-\frac{\xi}{e_{v,\lambda}}\frac{dI_\lambda(z,\xi)}{dz} = I_\lambda(z,\xi) - J_\lambda(z,\xi), \qquad (2.8)$$

where ξ is the cosine of the zenith angle (positive ξ means upward traveling stream of radiation, and negative ξ means downward traveling stream) and z is the vertical coordinate.
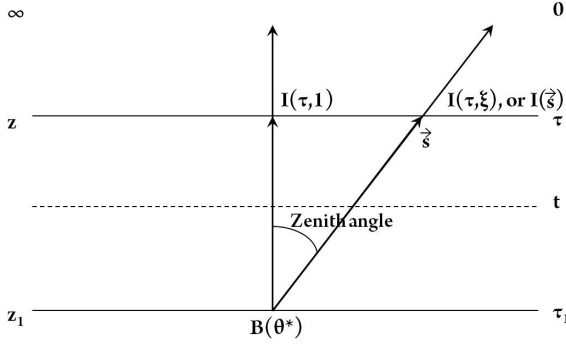
Figure 2.12: Thermal radiation in a stratified atmosphere, based on Goody and Yung (1989)

With the optical depth definition,

$$\tau_\lambda(z, \infty) = \int_z^\infty e_{v,\lambda} dz, \tag{2.9}$$

Eq. 2.8 becomes

$$-\xi \frac{dI_\lambda(z, \xi)}{d\tau_\lambda} = I_\lambda(z, \xi) - J_\lambda(z, \xi). \tag{2.10}$$

Figure 2.12 shows a sketch of radiation under the assumption of a stratified atmosphere. z_1 is the level of lower boundary and z is the level where radiance is observed, $I_\lambda(\tau, \xi)$ in ξ direction. The optical depth τ_1 is integrated from z_1 to the top of the atmosphere, and τ is integrated from z upward. The subtraction $(\tau_1 - \tau)$ gives the optical depth between z and z_1. The upward radiance at z can be expressed as

$$I_\lambda(z, \xi) = B_\lambda(\theta^*) \exp[-(\tau_1 - \tau)/\xi] + \int_\tau^{\tau_1} J_\lambda(t, \xi) \exp[-(t - \tau)/\xi] \frac{dt}{\xi}, \tag{2.11}$$

with the boundary conditions of $I_\lambda(\tau_1) = B_\lambda(\theta^*)$. The integral form of Eq. 2.11 along the distance $\mathbf{s}$ is

$$I_\lambda(\mathbf{s}) = I_\lambda(0) \exp\left[-\int_0^{\mathbf{s}} e_{v,\lambda}(\mathbf{s}')d\mathbf{s}'\right] + \int_0^{\mathbf{s}} J_\lambda(\mathbf{s}') e_{v,\lambda}(\mathbf{s}') \exp\left[-\int_{\mathbf{s}'}^{\mathbf{s}} e_{v,\lambda}(t)dt\right] d\mathbf{s}'. \tag{2.12}$$

Equation 2.12 is the integral form of the radiative transfer equation. This equation is used in the radiative transfer model to calculate the radiance I_λ along discrete ordinates from the source function J_λ. Radiative transfer routine SHDOM (Spherical Harmonic Discrete Ordinate Method, more information is in Appendix A) developed by Evans (1998) is adopted in this study. This routine is merged with the line-by-line calculation to take into account both the fine structure of the gaseous absorption bands and multiple scattering in the clouds.

For each wavenumber grid, the combined algorithm with SHDOM and the line-by-line method carried out the following steps. First, the vertical profile of gaseous absorption coefficient was calculated for the atmospheric model based on the VeRa temperature profile. Temperature and pressure corrections were applied for both line intensity and half-width. The line shape factor is used for the wing of CO_2 bands. The detailed descriptions are in Sect. 2.2.3.1. Second, the vertical profile of aerosol volume absorption coefficient was calculated for the selected cloud model (see, Sect. 2.2.4.1 Upper cloud model). Then, SHDOM returned the intensity of outgoing radiation at the selected wavelength for a certain emission angle. The above described procedure, repeated for all wavelengths in the 4.3–5.0 μm range, yielded monochromatic spectrum of the Venus thermal emission. Synthetic spectrum was convolved with a Gaussian function with 15 nm of the full width at half maximum (FWHM) to get VIRTIS synthetic spectrum $I_{syn}(\lambda)$ (Ignatiev et al. 2009).

2.2.3.1 Gaseous absorption

Synthetic spectra are derived from the transmission functions associated with atmospheric gases and aerosol extinctions. The optical depth of the atmospheric gases in this study is based on the line-by-line method. The gaseous optical thickness between the z level and the top of the atmosphere ($z = \infty$) is defined as

$$\tau_\lambda(z, \infty) = \int_z^\infty n(z')k_v dz',$$

(2.13)

where n is the number density of a chemical species and k_v is the monochromatic absorption cross-section per molecule of a chemical species at wavenumber v. k_v can be expressed in terms of the individual lines, i,

$$k_v(z) = k_v(p, T, v) = \sum_i Q_i(T)S_i(T)f_i(p, T, v)\chi(v - v_{0,i}),$$

(2.14)

where $Q_i(T)$ is the total internal partition sum for molecule, $S_i(T)$ is the line intensity, $f_i(p, T, v)$ is the shape of the spectral line and $\chi(v - v_{0,i})$ is the line shape factor[2], which corrects the absorption coefficient in the line wings for the deviation from the pure Lorenz functions (Titov and Haus 1997). Since many experiments revealed that the continuous absorption in the extreme tails of strong lines is much less than that calculated with the Lorentz line shape (Winters et al. 1964), it is necessary to combine the line shape factor for the far wings of strong bands.

$$S_i(T) = S_i(T_{\text{ref}})\left(\frac{Q(T_{\text{ref}})}{Q(T)}\right)\left(\frac{\exp[-c_2 E_i/T]}{\exp[-c_2 E_i/T_{\text{ref}}]}\right)\left(\frac{1 - \exp[-c_2 v_i/T]}{1 - \exp[-c_2 v_i/T_{\text{ref}}]}\right).$$

(2.15)

The above equation is the temperature correction of S_i from the reference temperature ($T_{\text{ref}} = 296$ K) to temperature T (Rothman et al. 1998, 2009). E_i is the lowest state energy [cm^{-1}], and c_2 is the second radiation constant ($ch/k = 1.4388$ cm·K).

---

[2]χ can be also called as sub-Lorentzian formfactor (Ignatiev et al. 1999), correction for non-Lorentzian shape (Kamp and Taylor 1990), sub-Lorentzian profile (Pollack et al. 1993) and line-shape correction factor (Tonkov et al. 1996).

The shape of a spectral line can be categorized into three main formation mechanisms. The first is a natural broadening due to the uncertainty of the energy level. The second is a Doppler broadening caused by a relative velocity between absorber and observer. It depends on temperature more than on pressure because temperature correlates with random motion of the radiator (Armstrong 1967). The third is a Lorentz (or collisional, pressure) broadening related to the collisions of molecular particles. The Lorentz line shape of an individual line is described below

$$f_L(\nu - \nu_0) = \frac{\alpha}{\pi[(\nu - \nu_0)^2 + \alpha^2]},$$

(2.16)

where ν_0 is the position of the line center and α is the Lorentz half width. Note that the halfwidth needs to be corrected for pressure p and temperature T through

$$\alpha(p, T) = \alpha_0 \left(\frac{p}{p_{ref}}\right)\left(\frac{T_{ref}}{T}\right)^n,$$

(2.17)

where n is the coefficient of temperature dependence of the halfwidth, and α_0 is the halfwidth, either air-broadening or self-broadening, at the reference condition (p_{ref} = 1 atm= 1013 mbar and T_{ref} = 296 K). Therefore, the shape of a spectral line is actually a function of pressure, temperature, and wavenumber. The Voigt line profile results from a superposition of independent Lorentz and Doppler line broadening profiles (Armstrong 1967). The Voigt line function (f_V) is shown below, where f_D denotes the Doppler line shape, ν^* is the shifted location from ν_0 due to Doppler effect, and f_L denotes the Lorentz line shape

$$f_V(\nu - \nu_0) = \int_{-\infty}^{+\infty} f_D(\nu^* - \nu_0) f_L(\nu - \nu^*) d\nu^*.$$

(2.18)

It can be rewritten as:

$$f_V(\nu - \nu_0) = \frac{1}{\alpha_D} \sqrt{\frac{\ln 2}{\pi}} \frac{y}{\pi} \int_{-\infty}^{+\infty} \frac{e^{-t^2}}{y^2 + (x - t)^2} dt,$$

(2.19)

where

$$y = \frac{\alpha_L}{\alpha_D} \sqrt{\ln 2}, \quad x = \frac{(\nu - \nu_0)\sqrt{\ln 2}}{\alpha_D}, \quad \alpha_D = \frac{\nu_0}{c} \sqrt{\frac{2k\theta \ln 2}{m}},$$

$$t^2 = \frac{mu^2}{2k\theta}, \quad u = (\nu^* - \nu_0)\frac{c}{\nu_0}$$

(2.20)

and u is a molecular speed. Since the Doppler profile depends on temperature related to the speed of molecules and the Lorentz profile depends on molecular collisions, the Doppler profile is formed primarily at high altitudes where it has low pressure, whereas the Lorentz profile becomes an important process of broadening at low altitudes where it has high pressure. Therefore this study adopts the Voigt line profile for general gaseous calculations for both cases.

The method of Titov and Haus (1997) is adopted for the fast line-by-line calculations. This method divides the absorption cross-section into two functions:

$$k(p, T, \nu) = G(p) \cdot F(T, \nu)$$

$$= \frac{p}{p_{ref}} F(T, \nu)$$

(2.21)

where $G(p) = p/p_{\text{ref}}$ is a function of pressure, and $F(T, v)$ is a function of temperature and wavenumber. Advantages of this method are associated with the computed matrix of $F(T, v)$ for the chosen temperature and wavenumber grids. This matrix can be interpolated to a certain temperature value at each wavenumber grid to calculate the absorption cross-section as

$$k(p, T, v_j) = G(p)[\text{interpolation for } T\{F(T_i, v_j)\}] \tag{2.22}$$

where i is the temperature grid index and j is the wavenumber grid index. Equation 2.22 needs a simplification to make the line halfwidth (α) as a function of temperature only ($\alpha_{\text{M}}(T)$):

$$\alpha_{\text{M}}(T_i) = \alpha_0 \left(\frac{p_{\text{M}}(T_i)}{p_{\text{ref}}} \right) \left(\frac{T_{\text{ref}}}{T_i} \right)^n \tag{2.23}$$

where $p_{\text{M}}(T)$ is the pressure value of a standard atmospheric model at T, and is replacing pressure p in Eq. 2.17. The Voigt function can be expressed with α_{M}

$$f_{\text{V}}(p, T, v - v_0) = \left(\frac{p}{p_{\text{ref}}} \right) \alpha_0 \left(\frac{T_{\text{ref}}}{T} \right)^n \cdot \frac{\ln 2}{\alpha_{\text{D}}^2} \frac{1}{\pi^{(3/2)}} \int_{-\infty}^{+\infty} \frac{e^{-t^2}}{y_{\text{M}}^2 + (x - t)^2} dt \tag{2.24}$$

where y_{M} is the same as y, but with α_{M} substituted for α_{L}. The $F(T, v)$ matrix for the Voigt function can be shown in this form:

$$F(T, v) = \frac{1}{\pi} \sum_i \alpha_{0i} \left(\frac{T_{\text{ref}}}{T} \right)^{n_i} Q_i(T) S_i(T) \chi_i(v - v_{0i})(L_v^{(1)} + L_v^{(2)} + L_v^{(3)}) \tag{2.25}$$

where $L_v^{(1)}$, $L_v^{(2)}$, and $L_v^{(3)}$ are the decomposition of the Voigt profile: $L_v^{(1)}$ defines the Doppler component, $L_v^{(2)}$ is related to the Lorentz function, and $L_v^{(3)}$ contributes the intermediate term (details in Titov and Haus (1997)).

In the 4.3–5.0 μm range main source of opacity are CO_2, CO, and clouds. This study takes into account the fundamental CO_2 absorption band at 4.3 μm, the weak band at 4.8 μm, and the CO band at 4.6 μm. The $F(T, v)$ matrices for each molecule was calculated with Eq. 2.25 first. The spectral line parameters for CO_2 and CO were taken from the HITRAN2008 database (Rothman et al. 2009). All isotopes were included under the assumption that Venus has same ratio of isotopes composition as the Earth (Owen 1978). Temperature and pressure corrections were applied for line intensity, self-broadened half-width for CO_2 and air-broadened half-width for CO. The line shape factor for CO_2 was taken from Winters et al. (1964)

$$\chi_i(v - v_{0,i}) = \begin{cases} \exp\left\{ -a[|v - v_{0i}| - v_{\text{min}}]^b \right\} & , \text{for } |v - v_{0i}| \geq v_{\text{min}} \\ 1 & , \text{for } |v - v_{0i}| \leq v_{\text{min}} \end{cases} \tag{2.26}$$

where $v_{\text{min}} = 5$ cm^{-1}, $a = 0.08$, and $b = 0.8$. The line cut-off value was set to 200 cm^{-1} and the wavenumber step was 0.1 cm^{-1}. Figure 2.13 is a test result of this calculation and a cross-checking with separate calculation made by Ignatiev (private communication). Although the two extinction coefficient spectra used different line parameter sources and cut-off values, it provided confidence in the use of $F(T, v)$ matrix.
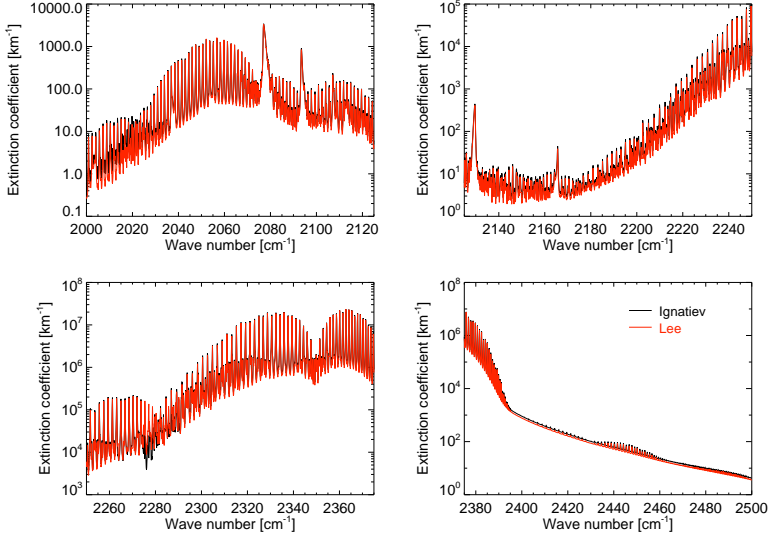
Figure 2.13: CO_2 extinction coefficient comparisons at 50 km altitude; (black) from Ignatiev and (red) from this calculation (CO_2 100% condition for both spectra).

2.2.3.2   Scattering and absorption by sulfuric acid aerosol

Atmospheric extinction coefficient (e_λ) is the sum of the absorption coefficient (k_λ) and the scattering coefficient (s_λ): $e_\lambda = k_\lambda + s_\lambda$. The dense Venusian atmosphere induces huge gaseous absorption, especially in case of thermal emission. The sulfuric acid aerosols are also very important because they are strong absorption and scattering sources in the infrared (Crisp 1989). Therefore, both gaseous absorption and aerosol effects should be calculated carefully. Crisp and Titov (1997) also showed the importance of multiple scattering effects due to cloud particles at infrared wavelengths. To consider cloud influences on the radiation field, this study uses three cloud particle optical properties: extinction (τ_{ext}), single scattering albedo (ω_{ext}), and asymmetric factor (g_λ). The single scattering albedo and asymmetric factor are defined as (Goody and Yung 1989)

$$\omega_\lambda = \frac{\tau_{\lambda,sca}}{\tau_{\lambda,ext}}, \tag{2.27}$$

$$g_\lambda = \frac{1}{2} \int_{-1}^{1} P(\cos\theta)\cos(\theta)d(\cos(\theta)) \tag{2.28}$$

where θ is the angle of scattering from the incident light direction. ω gives the ratio of scattering: $\omega = 0$ for total absorption and $\omega = 1$ for total scattering. g is positive for forward scattering, negative for backward scattering, and $g = 0$ is an isotropic scattering. The Henyey-Greenstein phase function is used to approximate Mie scattering phase

function for the radiative transfer model computation:

$$
\begin{aligned}
P_{HG}(\cos\theta; g) &= \frac{1 - g^2}{(1 + g^2 - 2g\cos\theta)^{3/2}} \\
&= \sum_{l=0}^{\infty} (2l + 1)g^l P_l(\cos\theta)
\end{aligned}
\tag{2.29}
$$

where P_l is a Legendre polynomial.

The upper cloud is dominated by mode 2 (mean radius~1.05 μm) particles (Pollack et al. 1980b, Ragent et al. 1985). We used the mode 2 optical properties to calculate thermal emission spectra. Figure 2.14 shows the single scattering albedo and asymmetry factor for mode 2. Mie model calculations were done to get single scattering albedo and asymmetric factor from the aerosol size distribution and refractive index database (Ignatiev, private communication).
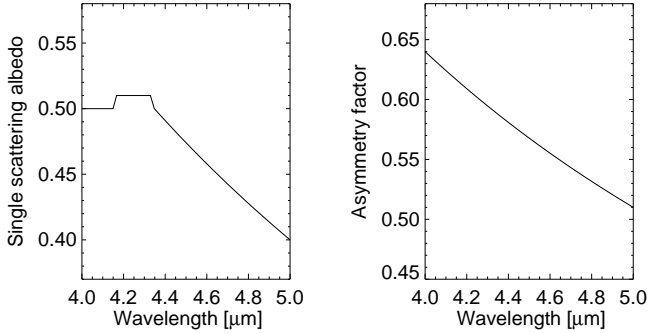
Figure 2.14: Single scattering albedo and asymmetry parameter for mode 2 particles (Ragent et al. 1985)

The sum of vertical profiles of monochromatic aerosol and gaseous extinction coefficients was used as input for SHDOM. The optical properties vary with the vertical coordinate (z) as

$$
\begin{aligned}
e_{v,z} &= e_{v,z,\text{gas}} + e_{v,z,\text{cloud}}, \\
\omega_{v,z} &= \frac{\omega_{v,z,\text{cloud}} \cdot e_{v,z,\text{cloud}}}{e_{v,z}}, \\
g_{v,z} &= g_{v,z,\text{cloud}}.
\end{aligned}
\tag{2.30}
$$

2.2.4 Method of the cloud top structure retrieval

We use the temperature profiles measured by the radio-science experiment VeRa. Synthetic spectra are derived with the upper clouds structure models. The aerosol model parameters are retrieved by fitting synthetic spectra to the VIRTIS observations.

2.2.4.1   Upper cloud model

The cloud deck of Venus has a complex vertical structure consisting of three layers, each with different microphysical and optical properties (Ragent et al. 1985, Esposito et al. 1997). The clouds also show strong temporal and spatial variations. Since the outgoing thermal emission is formed mainly in the upper part of the clouds, above ~60 km, we used a simplified cloud model. We assumed an exponential volume extinction profile for aerosols above 60 km, and constant extinction below this altitude:

$$E(z) = \begin{cases} E_0 \exp[(z-65)/H] & , z > 60 \text{ km} \\ E(60) & , z < 60 \text{ km} \end{cases} \qquad (2.31)$$

where $E(z)$ is the vertical profile of the volume extinction coefficient, H is the scale height, and E_0 is the extinction at 65 km altitude. We assume a constant aerosol volume extinction in the 4.4–5.0 μm range and define the "cloud top altitude" as the height of the unit optical depth ($z_{\tau=1}$, means $\tau(z,\infty) = 1$ level). Thus, our cloud model has two parameters: cloud top altitude (Z) and aerosol scale height (H). Figure 2.15 shows examples of vertical profiles of the aerosol volume extinction coefficient.
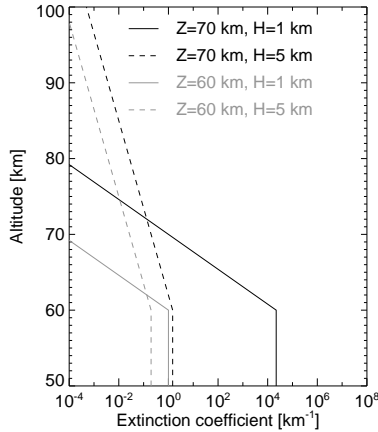
Figure 2.15: Example of vertical profiles of aerosol volume extinction.

2.2.4.2   Sensitivity to the model parameters

A VIRTIS synthetic spectrum depends on the cloud top model. We determine two model parameters, cloud top altitude $Z_{\tau=1}$ and aerosol scale height H, by fitting the synthetic spectra to VIRTIS measurements in each latitude bin. The sensitivity of the synthetic spectra to the upper cloud structure parameters strongly depends on latitudes, which induce different temperature structures. Hence, the accuracy of the cloud top parameter retrieval is latitude dependent. Figure 2.16 shows several typical situations encountered in our retrievals. At low latitudes characterized by monotonic temperature profile (Fig. 2.9(a)–(e)), the synthetic spectra significantly depend on the cloud top model
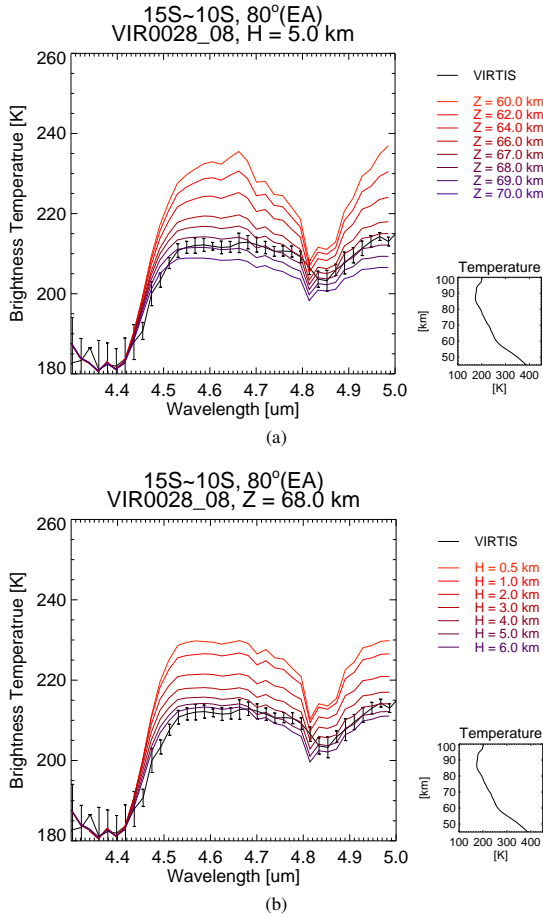
Figure 2.16: Synthetic spectra and VIRTIS measurements for the low latitude case. (a) the aerosol scale height H is fixed and the cloud top altitude Z is varied. (b) H is varied and Z is fixed. The legends show latitude bin, emission angle (EA), VIRTIS data file, and values of constant H or Z. The solid line is the VIRTIS spectrum and other lines correspond to synthetic spectra with different parameter values (see legends in the upper right of each sub-panel). The temperature structure is shown in the lower right of each sub-panel.

(Fig. 2.16(a) and (b)). On the contrary, in the polar regions with their quasi-isothermal atmosphere above the clouds (Fig. 2.9(i) and (j)), the sensitivity to the aerosol structure is rather weak (Fig. 2.16(c) and (d)).
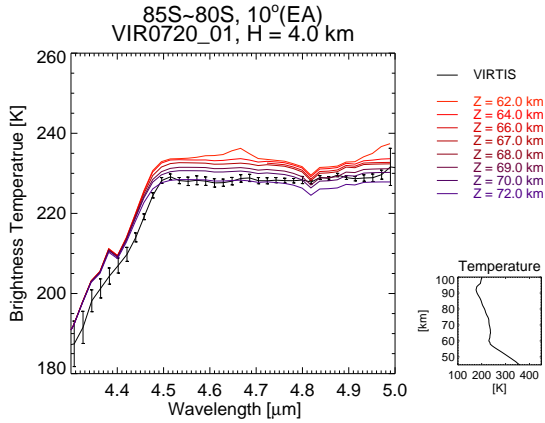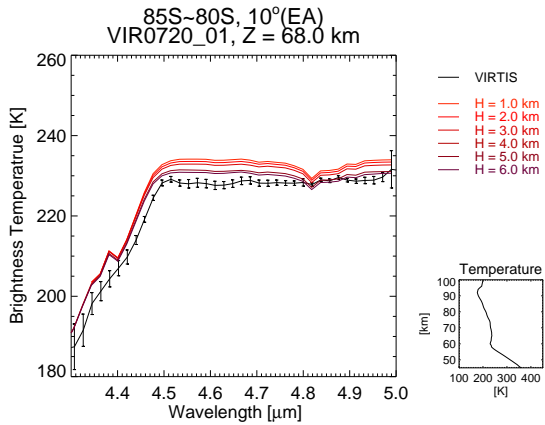
Figure 2.16: *(continued)* Same as Fig. 2.16(a) and (b), but for the polar case. (c) the aerosol scale height *H* is fixed and the cloud top altitude *Z* is varied. (d) *H* is varied and *Z* is fixed.

80S~75S, 15°(EA)
VIR0668_01, H = 0.2 km

(e)

80S~75S, 15°(EA)
VIR0668_01, Z = 62.0 km

(f)
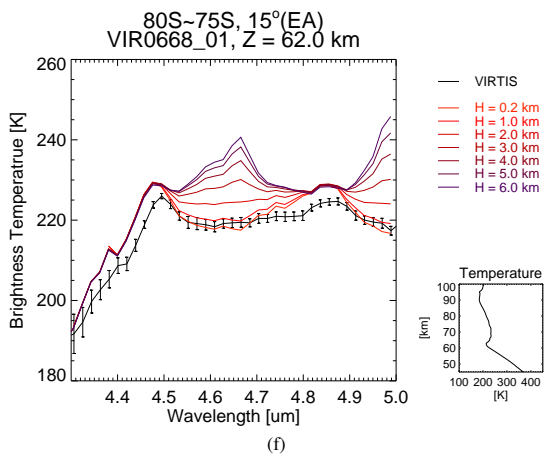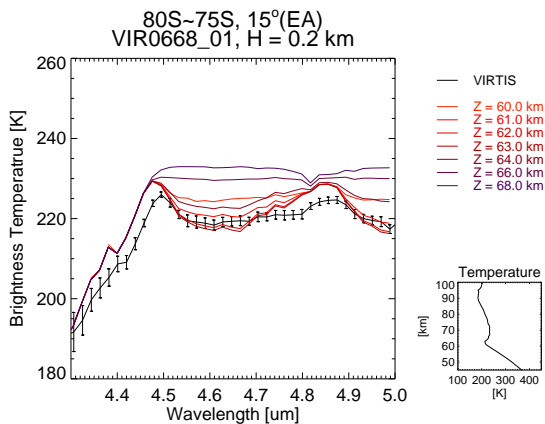
Figure 2.16: *(continued)* Same as Fig. 2.16(a) and (b), but for the cold collar case. (e) the aerosol scale height H is fixed and the cloud top altitude Z is varied. (f) H is varied and Z is fixed.

The strong dependence of synthetic spectra on the cloud model parameters (Fig. 2.16(e) and (f)) is also typical for the "cold collar" region, with its strong temperature inversions (Fig. 2.9(f)-(h)). However, retrievals of the aerosol parameters are more complex here. Fitting the synthetic spectra to the VIRTIS spectrum gives often ambiguous results, with two almost equally good formal solutions: the first one having a small aerosol scale height and low cloud top altitude and the second having a large aerosol scale height and high cloud top altitude. This ambiguity of particular cases at the cold collar will be discussed

in the next subsection.

2.2.4.3 Retrieval of cloud model parameters

The discrepancy between the synthetic spectrum (I_{syn}) and the observed one (I_{obs}) is quantified as:

$$D(Z, H) = \left(\sum_{i}^{N} |I_{obs,i} - I_{syn,i}(Z,H)|^2 \right) / N \qquad (2.32)$$

where N is the number of spectral data points. Only the points in the continuum (4.4–4.8 μm and 4.9–5.0 μm) are included in the sum. The procedure of cloud model determination involves minimization of the discrepancy function $D(Z, H)$ in a two-parameter space. $D(Z, H)$ is first calculated on a coarse grid with $\Delta Z = 2$ km and $\Delta H = 1$ km to find the approximate minimum of the discrepancy function. Then a fine grid with steps ≤1 km is made by inverse parabolic interpolation around the approximate minimum to find its position more accurately (Press et al. 1992). The process proceeds until grid size becomes less than 0.05 km.

Figure 2.17(a) shows typical examples of the two-dimensional discrepancy function $D(Z, H)$. At low latitudes, where air temperature monotonically increases with depth, the minimum of the discrepancy function is well defined. The fact that isolines of D are almost horizontal indicates that the cloud top altitude is better constrained than the scale height. In the same figure, (b) and (c) illustrate the exact procedures for finding the minimum point of discrepancy, starting from the black dot in (a), searching with finer Z and H resolution, respectively. In this case, the minimum D is associated with $H = 3.9$ km
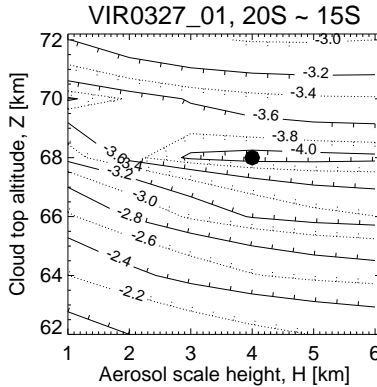
Figure 2.17: (a) Example of the discrepancy function $D(H, Z)$ in logarithmic scale, with a black dot marking the minimum. This is the result of the low latitude case (20–15°S) compared to VIRTIS data file VIR0327_01, with emission angle 60°. Starting from the black dot, finer resolutions of Z and H are used to find the minimum of $D(H, Z)$ more accurately with (b) fixed H and (c) fixed Z.
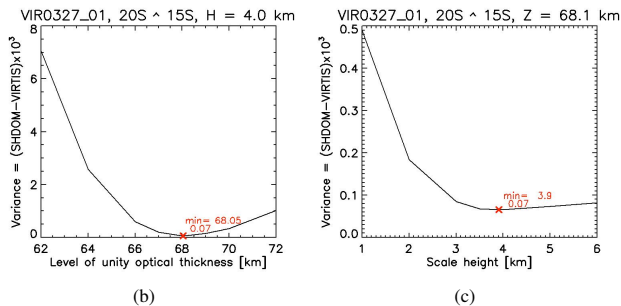
Figure 2.17: *(continued)* Finer resolutions of Z and H are used to find the minimum of $D(H, Z)$ more accurately from the black dot in (a). (b) uses fixed H and (c) uses fixed Z.

and $Z = 68.1$ km. In most cases, especially at low and middle latitudes, we followed this procedure to find the minimum of the discrepancy.

Figure 2.18 shows the more difficult case of a strong temperature inversion in the cold collar region. The discrepancy function can have two local minima: one for small (black dot) and one for large (grey dot) values of H. This illustrates the qualitative discussion in the previous subsection.

In many cases we resolve this ambiguity by using qualitative arguments and giving priority to the pair of model parameters, "small aerosol scale height and low cloud top altitude", which succeed to reproduce inversion in the wings of the 4.3 μm CO_2 band.
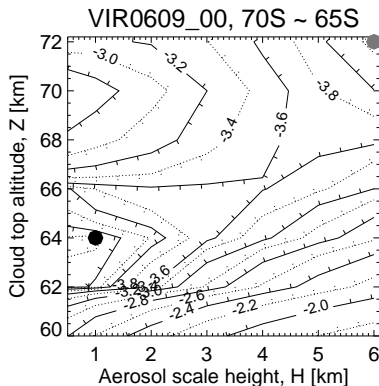
Figure 2.18: Example of the discrepancy function $D(H, Z)$ in logarithmic scale, with the black dot marking the minimum and the grey dot marking the secondary local minimum. This is the result of the cold collar case (70–65°S) compared to VIRTIS data file VIR0609_00, with emission angle 20°.

Figure 2.19 compares synthetic spectra for these two minima cases: small and large values of the aerosol scale height. In the case of $H = 1$ km the model with $Z = 63$ km fits the observed VIRTIS spectrum well (Fig. 2.19(a)). For $H = 6$ km the synthetic spectra approach the VIRTIS spectrum quite closely, but fail to reproduce its main feature – inversion in the shoulders of the 4.3 μm band (Fig. 2.19(b)). This behavior can be qualitatively explained by the following consideration. The sharp cloud top placed right at the temperature minimum of inversion allows thermal emission to form in the pure gaseous atmosphere in the inversion region above the cloud top thus resulting in spectral inver-
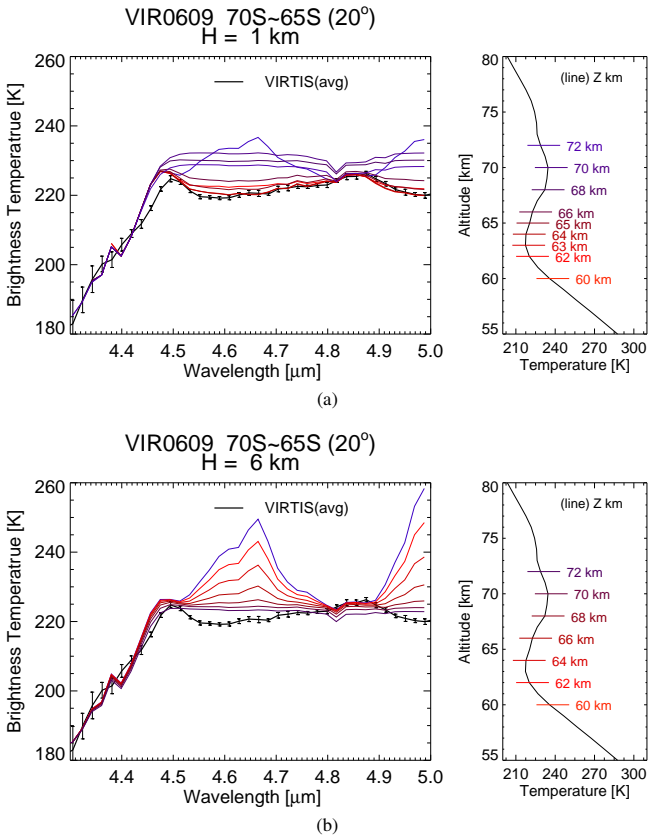
Figure 2.19: Comparisons of synthetic spectra with VIRTIS observation in the cold collar region for small (a) and large (b) aerosol scale height. Left panels show brightness temperature spectra. Thick solid lines are VIRTIS spectra from the file VIR0609_00. Colored lines are synthetic spectra for several cloud top altitudes, shown in the right panels together with the VeRa temperature profiles.
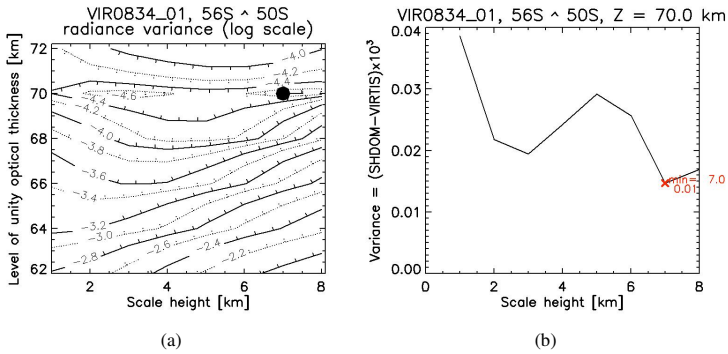
Figure 2.20: (a) Example of the discrepancy function $D(H, Z)$ in logarithmic scale, with the black dot marking the minimum. This is the result of the cold collar case (50–56°S) compared to VIRTIS data file VIR0834_01, with emission angle 30°. (b) The profile for a fixed cloud top altitude of 70.0 km is shown for variable aerosol scale heights.
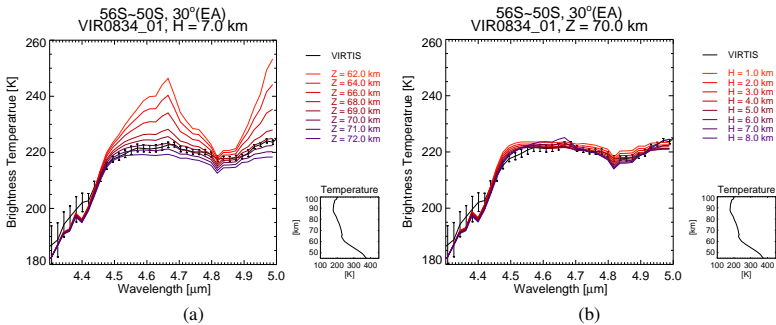
Figure 2.21: Comparison of synthetic spectra and VIRTIS measurements. The result is from the same source as Fig. 2.20. (a) The aerosol scale height H is fixed (7 km) and the cloud top altitude Z is varied. (b) The cloud top altitude Z is fixed (70 km) and the aerosol scale height H is varied. Notations are the same as in Fig. 2.16.

sion. When aerosols are distributed with a large scale height, they dominate opacity in the temperature inversion region and simply mask the temperature inversion.

The selection based on qualitative arguments is not valid for all cases in the cold collar area. Figure 2.20 shows one such case in the cold collar region. Figure 2.20(a) shows $D(H, Z)$ with the minimum point mark as a black dot ($H = 7$ km, $Z = 70$ km), and (b) presents there is a secondary minimum ($H = 3$ km, $Z = 70$ km). The spectrum from VIRTIS measurement, in Fig. 2.21(a) and (b), have none of the spectral inversion features shown in Fig. 2.11(c). This IR spectrum indicates that the origin of radiance is located above temperature inversion layer, or that the inversion layer is not deep enough.

If there are no clear spectral inversions, then the cloud model parameters are retrieved by the quantitative minimum point of discrepancy.

Summary

A new technique, the joint analysis of the VeRa temperature observation and the VIRTIS spectrum in the 4.3–5.0 μm range, is introduced to retrieve the upper cloud vertical structure. The merged routine of RTM (SHDOM) and the fast line-by-line method is used for the radiance calculation. The upper cloud layer is assumed as an exponential function with two free parameters: the cloud top altitude (Z) and the aerosol scale height (H). The methodology is the following: (1) VeRa temperature and two upper cloud structure parameters are used to generate synthetic spectrum, (2) the synthetic spectra are compared with the VIRTIS observations, and (3) the cloud top parameters are chosen by fitting the synthetic spectrum to the VIRTIS spectrum.

2.3   Result and discussion

We derived the parameters of the cloud top structure from the joint analysis of the selected VIRTIS spectra (see examples in Fig. 2.11) and corresponding VeRa temperature profiles for each latitude bin in the Southern hemisphere (Fig. 2.9). Figure 2.22 shows the latitude dependence of the cloud parameters. In the low and middle latitudes the cloud top altitude is 67.2±1.9 km. The aerosol scale height is 3.8±1.6 km which is close to that of the gas. Poleward of ~50°S the cloud structure changes significantly. The cloud top height decreases with latitude and reaches a minimum of ~63 km in the polar region. Aerosol scale height also decreases to 1–2 km. Table 2.2 summarizes the results of our analysis for three major latitudinal zones.

We note again that the cold collar region is characterized by temperature inversions (Fig. 2.9(f)–(h)), which in some cases make the retrieval of the cloud structure ambiguous. However, a typical cold collar spectrum, especially the spectral inversions in the wings of the 4.3 μm CO_2 band, can be only simulated with a small aerosol scale height and a low cloud top altitude (Fig. 2.16(e) and (f), and Fig. 2.19).

Figure 2.23 compares the latitude dependence of the cloud top altitude derived in this work with results of earlier observations. Our retrievals are consistent with the general trend for cloud top altitude to decrease with latitude, as obtained earlier from VIRTIS spectroscopy in the near-IR CO_2 bands (Ignatiev et al. 2009) and mid-IR spectroscopy by the Venera-15 Fourier spectrometer (Zasova et al. 2007). The cloud top altitude at 5 μm (diamonds) is around 3–6 km below that at 1.6 μm (crosses) for all latitudes. The tendency of the cloud top altitude to decrease with wavelength, shown in Fig. 2.23, is in quantitative agreement with that expected for a sulfuric acid composition of the upper

Table 2.2: Retrieved parameters of aerosol.

Latitude range	Mid–low lat. (0°–56°S)	Cold collar (56°–80°S)	Polar region (80°–90°S)
Scale height (km)	3.8 ± 1.6	2.1 ± 2.0	1.7 ± 2.4
Cloud top altitude (km)	67.2 ± 1.9	64.7 ± 3.2	62.8 ± 4.1
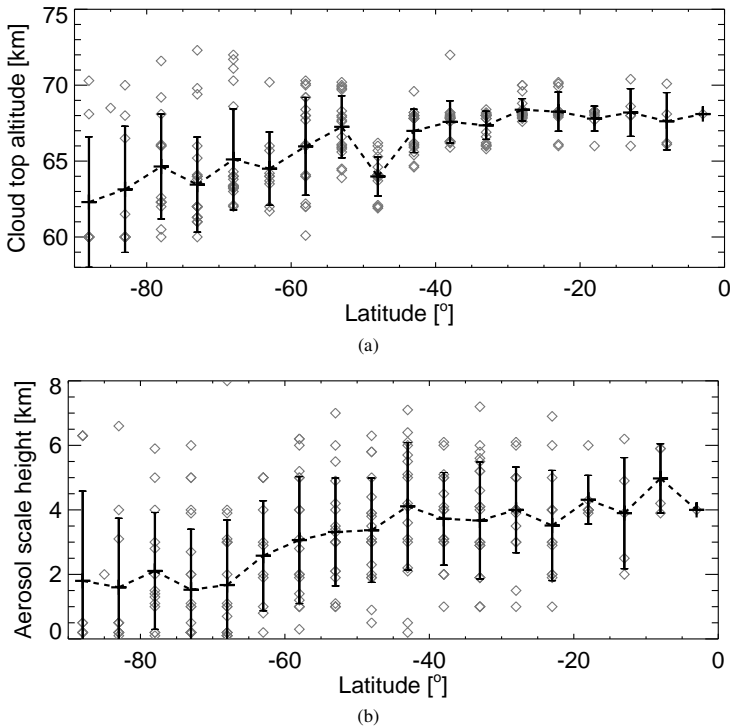
Figure 2.22: Latitudinal distributions of the cloud top altitude (a) and cloud scale height (b). Diamonds mark individual retrievals. Crosses and error bars are mean values and standard deviations within each latitude bin.

cloud at all latitudes (see, Fig. 2.25(a)). Also, day-night time deviations may be related since the result at 1.6 μm used day time data, and that at 5 μm used night time data. Our analysis also confirms the conclusions derived from the Venera-15 data that the aerosol scale height decreases towards the pole (Zasova et al. 1993, 2007), even though the 1.6 μm cloud top retrieval assumed the aerosol scale height of 4 km (Ignatiev et al. 2009).

Figure 2.23 also shows two peculiarities. Firstly, the cloud top altitude strongly descends from equator to pole in the 1–8 μm wavelength range, which sounds the upper cloud ($Z_{\tau=1} > 57$ km), whereas there is almost no decrease in cloud top altitude at a wavelength of 27.4 μm (open circles), which probes the middle cloud. This suggests that the upper cloud shrinks in vertical direction towards the pole, while the middle cloud does not change in altitude.

The second peculiarity seen in Fig. 2.23 is that poleward from the cold collar the 8 μm cloud top (filled circles) is located deeper than that at 5 μm, whereas the trend is opposite at low latitudes. This tentatively indicates differences in particle size at low and high
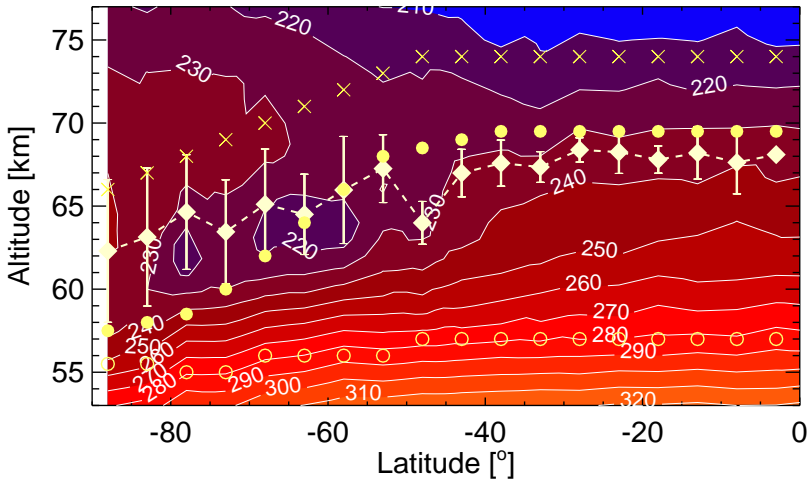
Figure 2.23: Latitude dependence of the cloud top altitude overplotted on the VeRa latitude-altitude temperature field: diamonds – this study (4.4–5.0 μm); crosses – VIRTIS spectroscopy in the 1.6 μm CO_2 band (Ignatiev et al. 2009); filled and open circles – approximate Venera-15 Fourier spectroscopy in the 8.2 and 27.4 μm, respectively (Zasova et al. 2007).

latitudes. The spectral behavior of the aerosol extinction efficiency depends on particle size. For a standard microphysical model of the Venus clouds the extinction efficiency for modes 2 and 2' (r_0 =1.0–1.4 μm) at 8.2 μm exceeds that at 5 μm (Fig. 2.24), meaning that in such a cloud the $\tau = 1$ level at 8.2 μm will be higher than that at 5 μm. This is what we see in Fig. 2.23 at latitudes below 50°–60°. For larger particles with $r_0 = 3.85$ μm (mode 3, curve 4 in Fig. 2.24), the ratio of extinction efficiencies is reversed, resulting in the cloud top at 8 μm being deeper than at 5 μm. This is exactly what Fig. 2.23 shows for the polar regions. Thus, this comparison suggests an increase of particle size in the upper cloud from equator to pole. This conclusion is consistent with the analysis of night side emissions observed by VIRTIS (Wilson et al. 2008), even though they are believed to sound deeper into the clouds (50–55 km). We note, however, that the conclusions drawn above from a comparison of observations by different missions are based on the assumption that the Venus cloud structure mainly depends on latitude.

The changes in the cloud top structure are correlated with the mesospheric temperature field (Fig. 2.23). The cloud top starts descending at the outer edge of the cold collar, around 50°S, and approximately follows the 230 K isoline. It is accompanied by a decrease of the aerosol scale height. Figure 2.25(a) shows a global view of the poleward decreasing cloud top with 4 km fixed aerosol scale height. There is negligible changes from noon to terminators. Drastic changes in the morphology of UV clouds are shown in Fig. 2.25(b). The transition from the patchy and mottled clouds at low latitudes to bright uniform polar hood also occurs in the cold collar region (Markiewicz et al. 2007a, Titov
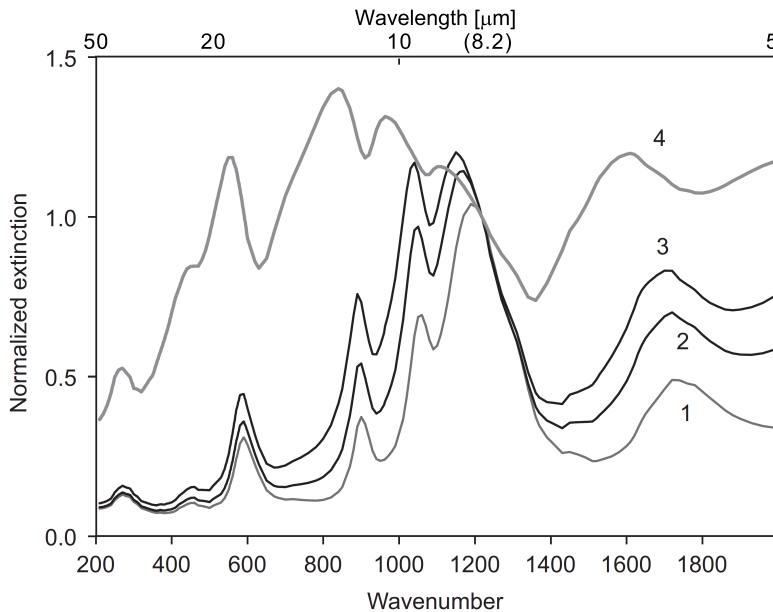
Figure 2.24: Normalized extinction efficiency, $Q_v/Q_{1218cm^{-1}}$, for 75% sulfuric acid particles. Curve 1 – mode 1, 2 – mode 2, 3 – mode 2', 4 – mode 3 (from Zasova et al. (2007)).

et al. 2008, 2012). This behavior of cloud top morphology is likely of dynamical origin and is related to the Hadley circulation, which has an upwelling branch at the equator and a downwelling motion at ~60°S (Svedhem et al. 2007). It needs more study to identify the exact mechanism for this moment.

The upper cloud has a very particular structure in the cold collar region. A very sharp cloud top with a small aerosol scale height (H≤1 km) coincides with a temperature minimum in the inversion layer (Fig. 2.26). This feature is likely of radiative origin. The sharp cloud top boundary provides effective cooling to space that maintains low temperatures. This mechanism is similar to that of formation of the temperature inversions at the Martian surface at night (Zurek et al. 1992). These inversions, in turn, create convectively stable conditions above the cloud top, which prevent vertical mixing of aerosols and maintain a sharp cloud boundary. This negative feedback between dynamical conditions and radiative effects makes the cold collar stable. The middle latitudes are also characterized by a vanishing vertical wind shear (Sánchez-Lavega et al. 2008), which suppresses wind shear instabilities. Titov et al. (2008) used the peculiarities of the stability distribution at the cloud top to qualitatively explain the global pattern of the UV markings.
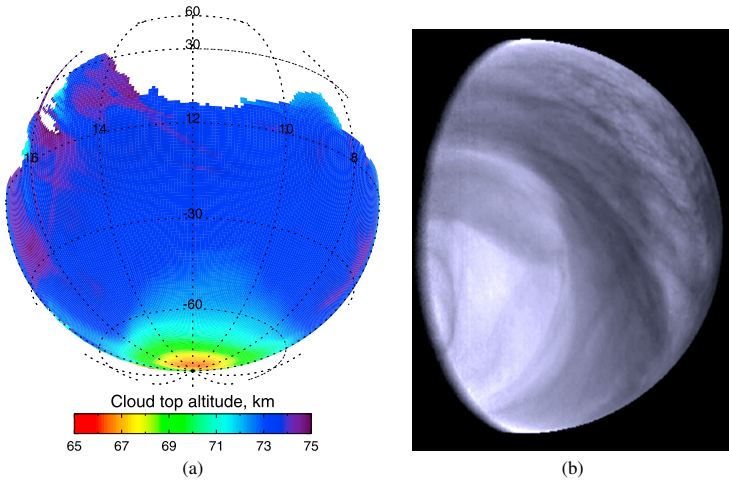
Figure 2.25: Global view of cloud morphology. (a) Cloud top altitude retrieved from VIRTIS-M-IR data (Ignatiev et al. 2009) and (b) the full view of the cloud tops of the southern hemisphere from equator (right) to the pole (lower left) observed by the VMC UV channel (Markiewicz et al. 2007a).
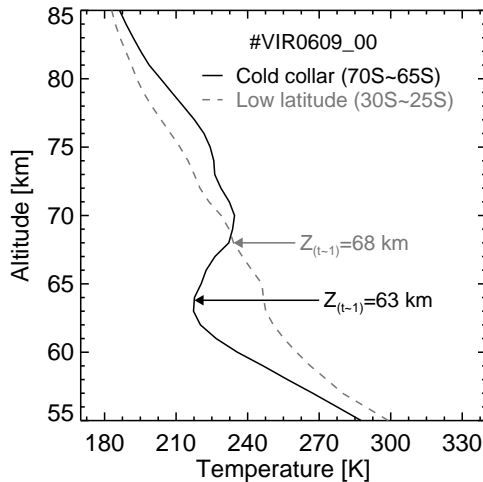
Figure 2.26: Comparison of different latitudinal zone cloud top altitudes related with temperature profiles. VIRTIS orbit, latitudinal bin, cloud top altitude information are shown in the figure. The cold collar case (black solid line) has the cloud top altitude below the temperature inversion layer at 63 km, and the low latitude case (grey dashed line) has a high cloud top altitude at 68 km.

3 Modeling of the thermal radiation in the Venus atmosphere

The strong latitude-dependence of the thermal structure of Venus mesosphere was reported by many observations (Seiff et al. 1985, Tellmann et al. 2009) including the decreasing trend of the cloud top altitude towards the poles as shown in Chapter 2. Clouds are the second most important thermal opacity source after carbon dioxide (Titov et al. 2007, Taylor and Grinspoon 2009) by reducing outgoing upward radiance and increasing atmospheric emission (Kondratev 1969). Compared to well-mixed carbon dioxide in the atmosphere, clouds have variable structure (Markiewicz et al. 2007b, Titov et al. 2008) that makes the clouds one of the most important element that defines the thermal IR fluxes. Therefore latitudinal trends of thermal structure and cloud vertical distributions are supposed to generate the variation of the thermal fluxes with latitude.

Vertical profiles of thermal IR fluxes profiles were reported by the four entry probes of the Pioneer Venus mission. The data showed variations of the thermal net flux from the cloud top altitude (~60 km) to the surface (Revercomb et al. 1985). The near IR observations showed that there is significant latitudinal variability in the cloud optical depth (Crisp et al. 1991, Titov et al. 2007). Also recent UV imaging by Venus Express showed strong variations of the cloud morphology (Markiewicz et al. 2007b, Moissl 2008, Titov et al. 2012). These observations provided strong impetus for numerical modeling of the thermal flux and their sensitivity to the cloud structure.

In this chapter we describe the model of thermal structure and the gaseous extinction in the lower atmosphere with a four mode aerosol size distribution. We apply the upper cloud structure derived in Chapter 2 to the cloud model combined with the middle and lower cloud layers.

3.1 Atmospheric structure and cloud model

Thermal and aerosol structure and composition of the atmosphere are the key inputs for a radiative transfer model. The atmospheric opacity is produced by absorption and scattering in gases and aerosols. The aerosol model is based on the observation data (Knollenberg and Hunten 1980, Pollack et al. 1980b, Zasova et al. 2007, Lee et al. 2012).

3.1.1 Temperature and pressure profile data

This study combines two sources to create combined temperature model of the Venus atmosphere: the Venus International Reference Atmosphere (VIRA) (Seiff et al. 1985)

below 50 km altitude and the results of atmospheric sounding by the radio-occultation experiment VeRa/Venus Express for mesosphere (50–95 km). The VIRA model of the troposphere (<60 km) is based on the direct measurement from descent probes. Although the measurements were limited in number, they showed that the low altitude thermal structure does not change much either with time or with latitude. Therefore, VIRA has been taken as a standard model of the troposphere. The inclusion of deep atmosphere data is key for an accurate thermal flux calculation.

3.1.1.1   VIRA (Venus International Reference Atmosphere)

Extensive investigations of the Venusian atmosphere by instruments onboard Venera and Pioneer Venus decent probes in 1970–90s establish the basic knowledge of physical properties of the atmosphere. The VIRA model represents a concise, descriptive document summarizing the physical properties of the atmosphere of Venus (Kliore et al. 1985). Seiff et al. (1985) derived the atmospheric model from the surface to 100 km in altitude. Since this model was published as a reference, many papers adopted the VIRA model or compared their results with VIRA (Haus and Goering 1990, Zasova et al. 1993, Roos-Serote et al. 1995, Drossart et al. 2007, Tellmann et al. 2009, Bézard et al. 2009, Bullock and Grinspoon 2001, Ignatiev et al. 2009).

The VIRA atmospheric model is based on the four Pioneer Venus probes, the Pioneer Venus Orbiter, and the Venera 10, 12, and 13 landers data. The atmospheric temperature from each measurement varied from a few K (below clouds) to 10–20 K (within clouds), or even larger due to the different locations (latitude and local time), the gravity wave amplitude and phase, and strong zonal wind around clouds level, as well as due to the systematic differences between measurements and techniques. Selected data were averaged to eliminate systematic offsets and variability within observations, and meantime the model has to preserve the static stability[1] for atmospheric dynamics (See, Seiff et al. (1985) for detailed descriptions). The atmospheric model has been constructed separately below 33 km altitude and above: one profile for all latitudes below 33 km and five latitude dependent profiles (0°–30°, 45°, 60°, 75°, and 85°) above 33 km. Both of northern and southern hemisphere data were merged under the assumption of hemispheric symmetry.

VIRA used hydrostatic equilibrium

$$dp = -\rho g dz,$$ (3.1)

and the equation of state,

$$P = \zeta \rho R T,$$ (3.2)

to obtain pressure and density profiles from temperature profile and the surface conditions. In Eqs. 3.1 and 3.2, P is pressure, ρ is density, g is gravity acceleration, z is altitude, T is temperature, R is the gas constant (191.4 j/kg·K, for the Venus atmosphere), and ζ is the compressibility. The equation of hydrostatic equilibrium (Eq. 3.1) is integrated for small interval Δz as like below

$$\frac{p_2}{p_1} = e^{-(\bar{g}\Delta z/R\bar{T})}$$ (3.3)

---

[1]The static stability is a difference between the atmospheric lapse rate, $\Gamma \equiv -\partial T/\partial z$, and the adiabatic lapse rate, $\Gamma_d \equiv -dT/dz = g/c_p$. It presents an atmospheric stability, whether it is a stably stratified, or not. The static stability criteria for dry air is the following: $\Gamma < \Gamma_d$ means that the atmosphere is statically stable, $\Gamma = \Gamma_d$ means statically neutral, and $\Gamma > \Gamma_d$ means statically unstable (Goody and Yung 1989).

where p_2 is obtained value, p_1 is given value, $\bar{g}$ is the mean gravity acceleration, and $\bar{T}$ is the mean temperature. The compressibility factor range is from 1.010 at the surface to 0.9928 at 26 km. The pressure model falls within the total range of the five probes measurements.

3.1.1.2   Atmospheric model (0–100 km): VeRa and VIRA

The VeRa observation provides temperature sounding with high vertical resolution in the 40–95 km altitude range and good spatial coverage for the whole southern hemisphere (Sect. 2.2.2.1). In this study, we keep the same latitudinal bin, around 5° latitude size, as used in Chapter 2. Our pressure and temperature model combines VeRa measurements in the 50–95 km altitude range, and VIRA profiles for 0–50 km and above 95 km with 1 km vertical resolution. While VeRa data are averaged within each latitudinal bin, the five VIRA profiles are taken along the latitude ranges (0°–30°, 30°–52.5°, 52.5°–67.5°, 67.5°–80°, and 80°–90° latitude). To remove discontinuity points between two data sources, a running averaged value (Chapman 2007) was used in the 48–52 km range. Horizontal translations of VIRA profile has been taken for above 95 km of VeRa data to assure continuity of profile instead of the extrapolation from the VeRa profile because of the large deviation of temperature lapse rate above 90 km in the VeRa profiles. A total of 133 VeRa subsets are used for the latitudinal average, from orbit number 84 (2006-07-14) to orbit 1141 (2009-09-3), including newly updated data in 2010.

Figure 3.1 shows examples of temperature and pressure profiles for three latitudinal

(a)
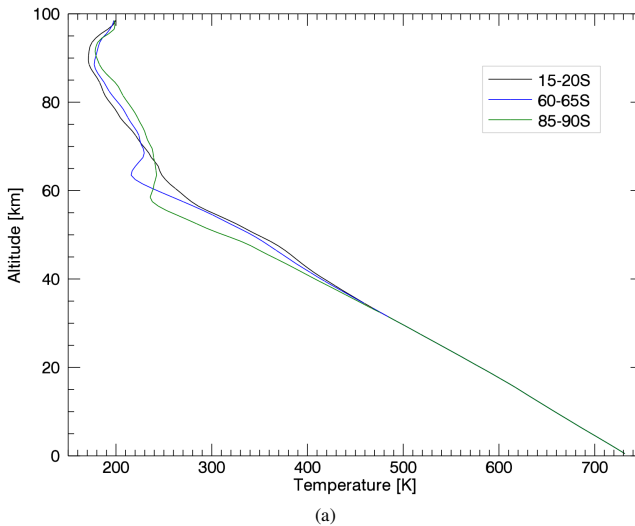
Figure 3.1: (a) Input temperature profiles, merged VeRa measurements and VIRA models. Three colors represent different latitudinal regions: low latitude (15–20°S), the cold collar (60S–65°S), and the pole (85–90°S). Gray boxes represent approximate cloud layers.

(b)
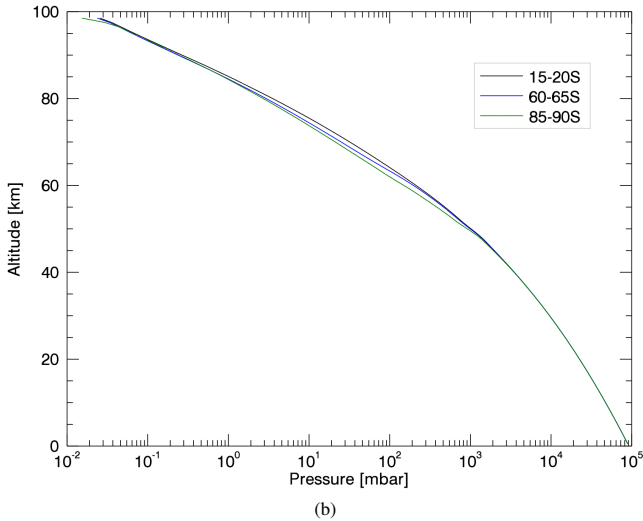
Figure 3.1: *(continued)* (b) Input pressure profiles. Descriptions of the latitudinal regions are same as in Fig. 3.1(a).

zones; low latitude, the cold collar, and pole. The surface temperature is fixed as 735 K for all latitudes according to VIRA. VIRA provides latitude dependent model from the 33 km level, but, the latitudinal temperature changes are not significant below cloud layers, compared to large variation above 40 km altitudes. Pressure profiles show little latitudinal deviations near to the cloud top region. Appendix A provides a table of temperature and pressure profiles for these three latitudinal bins in Fig. 3.1.

3.1.2   Cloud structure

The main cloud deck is located between 50 km and ~70 km altitudes. The clouds consist of three layers: upper (>58–60 km), middle (50–60 km), and lower (48–50 km) layers. The long-term variation of the upper cloud layer and overlying haze were detected by the ground-based polarimetric observations. In the late 1960s and early 1970s, the overlying haze was absent, then in the late 1970's, a submicron haze covered the whole disk (Ragent et al. 1985, Zasova et al. 2007). The altitude of the upper cloud boundary was tentatively found to be by 3–4 km lower in the polar regions. The middle cloud layer was found to be the most constant region, while variations of the upper and lower cloud layers are significant (Ragent et al. 1985).

Observations from entry probes, orbiting satellites, flyby spacecrafts, and ground-based provide the present information on cloud particles. In particular, descent probes provided the reliable data sets that are used to derive the microphysical properties of aerosol particles. Nephelometer and particle size spectrometer experiments from the Venera and Pioneer Venus probes suggested three distinct-size modes; "mode 1" (the small-
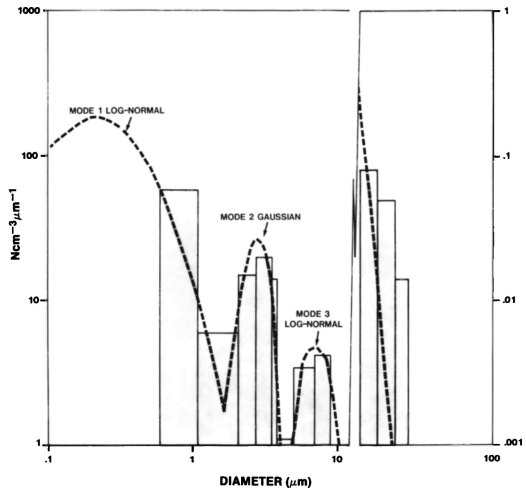
Figure 3.2: The size distributions for mode 1, 2, and 3 at 54.2 km altitude (from Knollenberg and Hunten (1980)).

size, mean radius less than 0.2 μm) , "mode 2" (the middle-size, mean radius of around 1.0 μm), and "mode 3" (the large-size, mean radius of around 3.8 μm) particles as shown in Fig. 3.2. Mode 1 particles pervade the entire cloud layers, with number density progressively increasing with depth. Mode 2 particles are believed to have grown from mode 1 particles as a result of photochemical reactions. The number density of mode 2 is dominant in the upper cloud layer. Mode 3 particles appear in the middle and lower cloud layer with a large peak in the lower layer (Pollack et al. 1980b, Ragent et al. 1985). In addition to the three modes, Pollack et al. (1980b) used four modes of particles size distributions. Since Knollenberg and Hunten (1980) identified the larger mode 2 particles in the middle cloud layer, "mode 2'" (mean radius is 1.4 μm) particles were introduced to fit Pioneer Venus measurements (Zasova et al. 2007).

Table 3.1 shows the parameters of four mode particles, which are adopted in this study. Upper cloud layer is assumed a single particle size distribution of mode 2, following the assumption of Chapter 2. On the other hand, submicron upper haze is almost transparent in infrared wavelength (Ignatiev et al. 2009). The cloud model of Zasova et al. (2007) showed that the extinction coefficient of mode 1 is around one-tenth of that of mode

Table 3.1: Four mode cloud particle properties (Zasova et al. 2007).

Mode	Mean radius (μm)	σ (log-normal particle size distribution)
Mode 1	0.15	1.91
Mode 2	1.05	1.21
Mode 2'	1.4	1.23
Mode 3	3.85	1.3
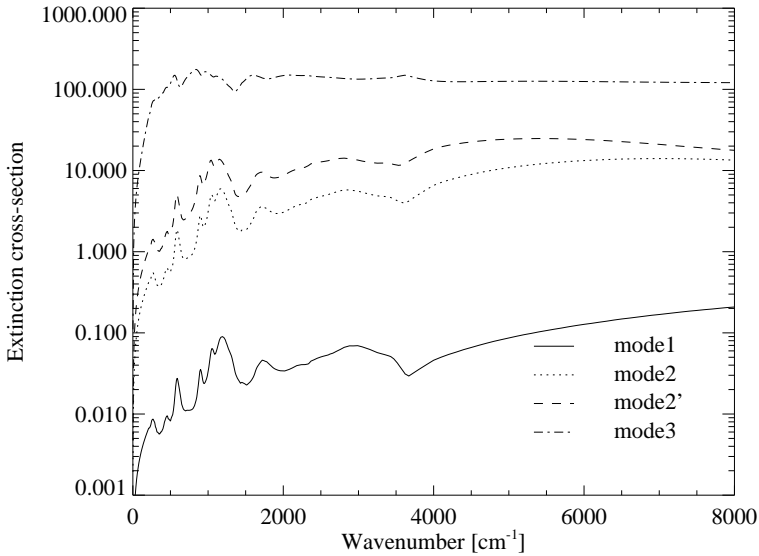
Figure 3.3: Extinction cross-section spectra of four mode particles. Parameters of each mode are shown in Table 3.1.

2 in 1218 cm^{-1}, then becomes negligible in shorter wavenumber regions above 60 km. Therefore we neglected the effects of mode 1 in the upper cloud layer, and followed our work as in Chapter 2 about the upper cloud vertical structure. The middle and lower cloud layers are combinations of mode 1, mode 2' and mode 3 particles. We took the vertical structure of the middle and lower cloud layers from Zasova et al. (2007). The free variable of this study is the parameters of the upper cloud vertical structure, while the middle-lower cloud layer structures are fixed on latitudinal changes.

Extinction cross-section of aerosol particles strongly depend on the wavenumber. Figure 3.3 presents the spectra of extinction cross-section [μm^2/particle] of each mode (calculated by Ignatiev, Personal communication). These spectral extinction cross-sections are calculated with Mie code, based on the cloud particles assumed to be 75% H_2SO_4. The figure shows principle absorption bands of H_2SO_4 at 450, 580, 900, 1150 cm^{-1} (Zasova et al. 2004). The large variations of each extinction spectrum imply that spectral dependency of cloud top altitude.

Figure 3.4 shows the change of cloud extinction profiles at three wavenumbers. Extinction coefficient of clouds is increasing with wavenumber. The upper cloud structure (red solid line) in the figure is taken from Table 2.2) in the mid-low latitude region (the cloud top altitude is 67.2 km and the aerosol scale height 3.8 km). It has very weak cloud extinctions at 365 cm^{-1} in (a), as shown in Fig. 3.3 which presents quick decrease of extinction cross-sections for all modes in smaller wavenumber from ∼500 cm^{-1}. (b) is at 2000 cm^{-1}, within the infrared range. The large cloud extinction appears around
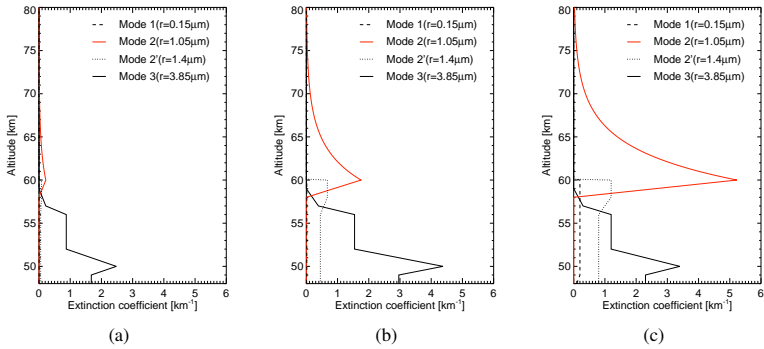
Figure 3.4: Vertical cloud extinction coefficients profiles with four mode model at (a) 365 cm^{-1}, (b) 2000 cm^{-1}, and (c) 18000 cm^{-1}. Mode 1, 2', and 3 are taken from Zasova et al. (2007) below 60 km altitude. The upper cloud layer, above 60 km, takes account mode 2 (red solid line) from Chapter 2 (Lee et al. 2012).
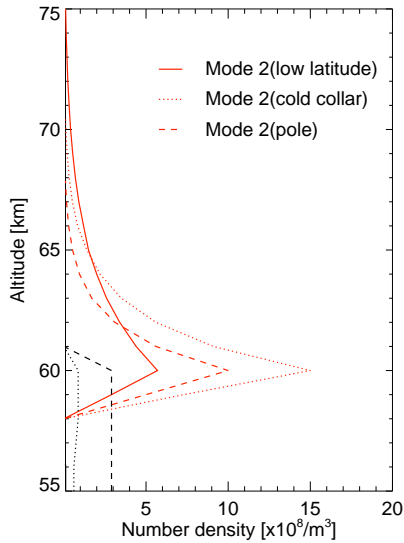
Figure 3.5: Vertical distribution of particle number density [m^{-3}]. The upper cloud layers used Table 2.2 values for three regions: low latitude, the cold collar, and the pole.

18000 cm^{-1}, in the visible range (c), with apparent extinction coefficients for four modes.
    The equation below defines the number density

$$N_i(z) = \frac{E_i(z, \nu)}{Q_i(z, \nu)}$$

(3.4)

where z is altitude (km), ν is wavenumber (cm^{-1}), i indicates each modes (mode 1, 2, 2', and 3), E_i is extinction coefficient as shown in Fig. 3.4, Q_i is extinction cross-section as shown in Fig. 3.3, and N_i is the particle number density. The process of considering aerosol extinction is the following: first, the upper cloud structure is decided as a free variable with fixed the middle and lower cloud extinction profiles (Fig. 3.4 shows the red solid line which indicates the upper cloud layer). The upper cloud structure is based on the aerosol extinction profiles at 2000 cm^{-1} following Chapter 2. Second, the number densities of four modes are derived from Eq. 3.4. Three, the cloud extinction coefficient profiles are calculated by multiplying the number density and extinction cross-sections (Fig. 3.3) with wavenumber and altitude.

    The number density profiles are shown in Fig. 3.5 based on the averaged values as in Table 2.2 (Chapter 2). The case of low–middle latitude, 67.2 km cloud top altitude and 3.8 km aerosol scale height, is the same as the extinction profiles in Fig. 3.4. The largest number density is shown in the curve for the cold collar and the smallest is the curve for the low latitude condition.
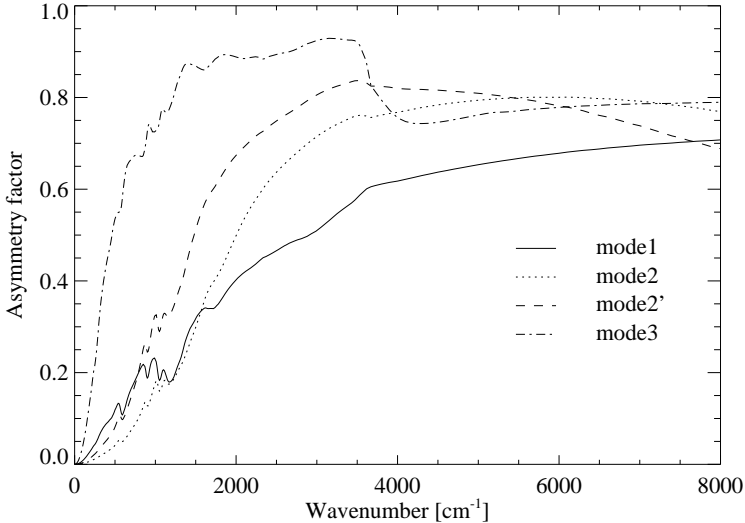
Figure 3.6: Asymmetry factor spectra along the wavenumber from 1 to 8000 cm^{-1} range. Mode 1 (solid), mode 2 (dotted), mode 2'(dashed), and mode 3 (dot-dashed) are shown together.
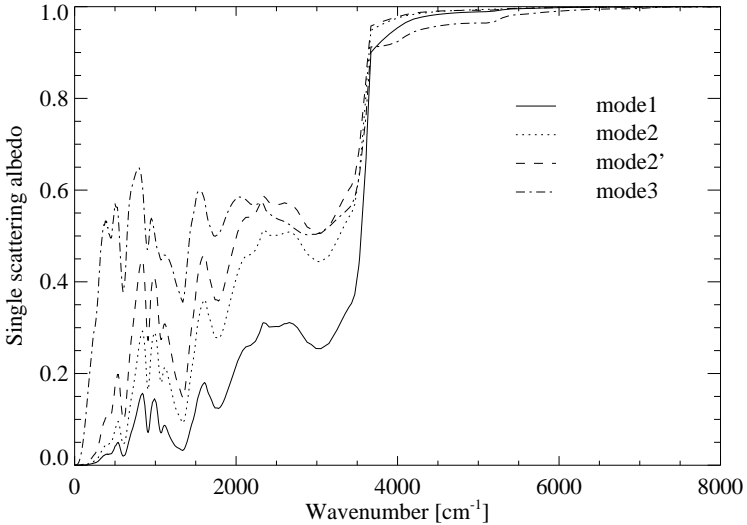
Figure 3.7: Single scattering albedo of each mode. Notations are the same as in Fig. 3.6

The other optical parameters of each mode, asymmetry factor for the Henyey-Greenstein phase function, and single scattering albedo, are also wavenumber dependent. It is shown in Fig. 3.6 and Fig. 3.7 for each mode, which are calculated by Ignatiev (personal communication). Asymmetry factor is an index of the scattering direction: $g = 0$ means isotropic scattering, $g > 0$ is forward scattering, and $g < 0$ is backward scattering (Sect. 2.2.3.2). Light scattering of large particles (aerosol size > wavelength) tends to have forward scattering as shown in Fig. 3.6 at large wavenumbers. At small wavenumbers (size≪wavelength), the scattering becomes isotropic (Rayleigh scattering). Single scattering albedo is the fraction scattering of the total extinction (k_{sca}/k_{ext}). In wavenumber < ~4000 cm^{-1}, single scattering albedo decreases quickly and absorption of aerosol becomes strong. The decreasing single scattering albedo is related with the absorption of H$_2$SO$_4$ and results in the strong thermal absorption of clouds in IR range.

Summary

Sect. 3.1 describes temperature and cloud structure as a function of latitude. The temperature structure developed in this study is combined the Venus international reference atmosphere (VIRA) below 50 km and observed temperature profiles from radio occultation sounding by VeRa/Venus Express. The temperature model covers from the surface to the mesosphere (0–100 km) to obtain accurate flux profile calculation that will be discussed in the next chapter. The aerosol structure assumes three-layered clouds with four modes particle size distribution. The upper cloud structure is based on the result of Chapter 2, which is latitude dependent, and the middle and lower cloud layers are assumed as

latitude independent.

3.2 Thermal emission calculation

This chapter will focus on the radiative transfer model developed for the thermal IR range. The basic radiative transfer equations for upward and downward fluxes will be discussed first, followed by the description of the monochromatic extinction properties. Line-by-line gaseous and aerosol extinction calculation routine are improved to take into account inhomogeneous atmosphere. This line-by-line routine is applied in a broad spectral range and it is merged with a radiative transfer model (SHDOM) (Evans 1998) to obtain monochromatic fluxes (Chapter 2). We introduce a division of the broad spectral range in sub-intervals to optimize the calculations. Rayleigh scattering and consideration of the heterogeneous optical properties are explained.

3.2.1 Flux calculation

Section 2.2.3 explained the monochromatic radiance calculation. The optical properties of medium are needed to solve radiative transfer Eq. 2.12. Radiance is integrated from the source function along the path and then integrated over solid angle to obtain fluxes. The monochromatic flux at P point in $\mathbf{d}$ direction is expressed as the below equation

$$F_{\nu,\mathbf{d}}(P) = \int I_\nu(P, s) \cos(\mathbf{d}, s) d\omega_s, \tag{3.5}$$

where $I_\nu(P, s)$ is monochromatic radiance at P in s direction and ω_s is the solid angle (Goody and Yung 1989). In a stratified atmosphere, the vertical flux can be defined with two parts division

$$F_\nu(\tau) = 2\pi \int_0^1 I_\nu(\tau, \xi)\xi d\xi + 2\pi \int_{-1}^0 I_\nu(\tau, \xi)\xi d\xi \tag{3.6}$$

where ξ is the cosine of the zenith angle and used the definition of the solid angle, $d\omega = -2\pi d\xi$. First and second terms on the right hand side represent the integration over positive hemisphere, upward flux, and negative hemisphere, downward flux, respectively.

In SHDOM, hemispheric fluxes are calculated at every grid point ($\mathbf{x}_i$), as a summation,

$$F^\pm(\mathbf{x}_i) = \sum_{j=1}^{N_\mu/2} w_j \sum_{k=1}^{N_{\phi j}} \hat{w}_{jk} |\xi_j| I_{ijk} \tag{3.7}$$

where the zenith angle sum (j) is over either the upward ($+$) or downward ($-$) hemisphere ordinates. w_j are the Gauss-Legendre quadrature weights and $\hat{w}_{jk}$ are the azimuthal integration weights normalized appropriately. N_μ indicate Gaussian quadrature cosine zenith angles, and N_ϕ are evenly spaced azimuth angles (Evans (1998))

Upward and downward fluxes show energy flow at each level. The altitude gradient of the net flux profile, which is a difference between downwelling and upwelling fluxes, defines energy deposition within a stratified atmosphere. For the thermal emission and

cooling rate calculation, it is necessary to integrate monochromatic fluxes over a broad wavenumber, which can be called flux density [W/m^2]

$$F(\tau) = \int F_\nu(\tau) d\nu. \tag{3.8}$$

In this study, the surface emissivity is assumed to be 0.8, for the basalt, at all wavenumbers (Haus and Arnold 2010). The downward flux at the upper boundary was set to zero under the assumption of no source above.

3.2.1.1   Gaseous absorption

In order to model thermal fluxes, we need to calculate gaseous absorption coefficients which vary strongly with wavenumber. We use the method of the fast line-by-line calculations same as Chapter 2 (Titov and Haus 1997). We improve the method by expanding the matrix of absorption coefficients to three dimensions (wavenumber, temperature, and pressure) from a two dimensional matrix (wavenumber and temperature) which had been used in Chapter 2 (see, Sect. 2.2.3.1 for the details). This modification allows us to get more accurate calculation of the gaseous extinction for temperature inversion region (See, Fig. 3.1(a)). The pressure and temperature range of the matrix covers the entire atmosphere of Venus from the surface to the 100 km altitude. Wavenumber range starts from 50 cm^{-1} with 0.1 cm^{-1} grid size up to 8300 cm^{-1}. Temperature range is from 150 K to 750 K with a grid size of 20 K (31 grids). Pressure grid is one order of magnitude in a logarithmic scale of [mbar] from 5 (10^5 mbar) to -3 (10^{-3} mbar) (9 grids).
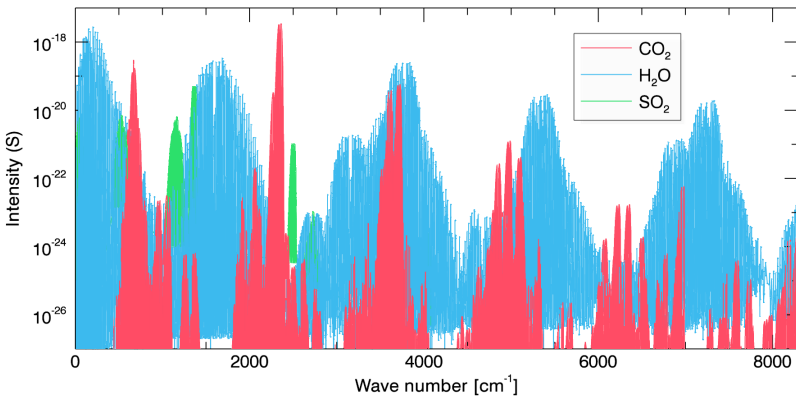
Figure 3.8: Distribution of line intensities of CO_2 (red), H_2O (blue), and SO_2 (green) along the wavenumber. The ratio of atmospheric composition is not considered for this figure.

To accomplish gaseous absorption calculations, it is necessary to manage a very large number of data set of line parameters and make a trade-off between accuracy and computation time. We select three major thermal opacity gases for this calculation: CO_2,

Table 3.2: Summary of HITRAN2008 lines used in the gaseous absorptions of H_2O, CO_2, and SO_2

Molecule	Isotopologue	Abundance	Number of lines
H_2O	161	0.997317	69,201
	181	1.99983×10^{-3}	
	171	3.71884×10^{-4}	
	162	3.10693×10^{-4}	
	182	6.23003×10^{-7}	
	172	1.15853×10^{-7}	
CO_2	626	0.984204	314,919
	636	1.10574×10^{-2}	
	628	3.94707×10^{-3}	
	627	7.33989×10^{-4}	
	638	4.43446×10^{-5}	
	637	8.24623×10^{-6}	
	828	3.95734×10^{-6}	
	827	1.47180×10^{-6}	
	838	4.44600×10^{-8}	
	837	1.65354×10^{-8}	
SO_2	626	0.945678	58,250
	646	4.19503×10^{-2}	

H_2O, and SO_2. CO_2 is the strongest greenhouse agent in the Venusian atmosphere, followed by clouds, H_2O, and SO_2 (Tomasko et al. 1980, Pollack et al. 1980a, Schofield and Taylor 1982, Revercomb et al. 1985, Titov et al. 2007). Line parameters are taken from HITRAN2008 (Rothman et al. 2009). Table 3.2 shows the line parameters for selected gases. These absorption lines are spread over the entire infrared range. Figure 3.8 presents the locations and strengths of the lines. Pronounced CO_2 bands are at 667 cm^{-1}(=15 μm) and 2349 cm^{-1} (=4.3 μm), and other bands are near to 961, 1064, 1259, 1366, 1932, 2083, 3613, 3715, 497,8 and 5099 cm^{-1}. Absorption lines of H_2O and SO_2 are shown together in Fig. 3.8. Absorption lines of SO_2 are located in the shorter wavenumber, but H_2O spreads into the whole wavenumber range. All isotopes are included under the assumption that the ratio of isotopes on Venus atmosphere is equal to the telluric values (Owen 1978, de Bergh et al. 2006). We use the vertical profile of minor gases as shown in Fig. 3.9.

A problem in the gaseous absorption calculation is in the uncertainties of our knowledge of line parameters in the deep atmosphere of Venus. High pressure and hot temperatures provide extreme conditions for the absorption line shape which has not been measured for the entire wavenumbers. Broadenings of lines of trace gases by CO_2 is also poorly known. In spite of the limitations on line parameters, we collected data from previous studies, which had succeeded to produce comparable radiance spectra to the observations. The detailed information of line parameters are the following.

Carbon dioxide absorption calculation

CO_2 is the major constituent of the Venus atmosphere. The strong pressure broadening of CO_2 induces that the absorption of the far wings of CO_2 bands are comparable
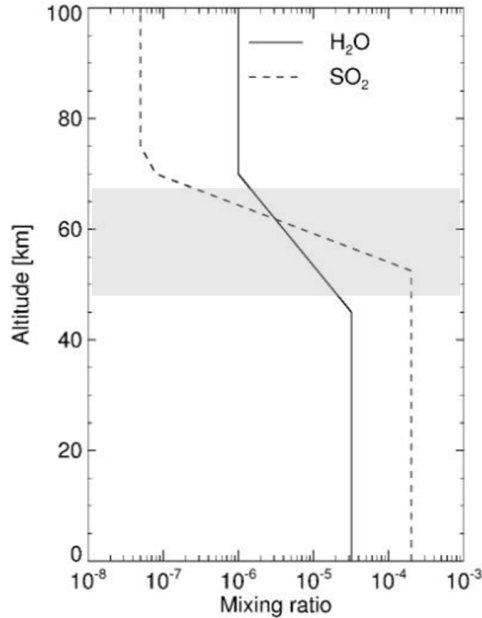
Figure 3.9: The profiles of mixing ratio of H_2O (solid line) and SO_2 (dashed line). The values are taken from (Titov et al. 2007). Grey transparent box indicate approximate cloud layers.

to that of the bands of other trace gases. Therefore the correct information of the line shape of CO_2 becomes crucial to estimate accurate gaseous absorptions. Many studies found that the Lorentz shape for the line wing produced an excess of absorption compared to observations. Empirical corrections of Lorentz line shape are used generally in aid of precise and easy implementation. A large set of line shape factor are proposed and applied to analyze observations (Winters et al. 1964, Burch et al. 1969, Moskalenko and Parzhin 1981, Tanaka and Yamanouchi 1977, Pollack et al. 1993, Meadows and Crisp 1996, Tonkov et al. 1996, Ignatiev et al. 1999). Each line shape factor was developed and used for particular gaseous band, and hence this study uses five line shape factors for five separate wavenumber ranges based on the data sources. Line shape factors are described in the following paragraphs, in the order of increasing wavenumber.

Below 2000 cm^{-1}, the line shape factor is taken from Ignatiev et al. (1999), which had been used for 250–1650 cm^{-1} range. It is based on the study by Moskalenko and Parzhin (1981).

$$\chi(\nu - \nu_0) = \begin{cases} 1 & \text{, for } |\nu - \nu_0| \leq d \\ \exp\{-a(|\nu - \nu_0| - d)^c\} & \text{, for } |\nu - \nu_0| > d \end{cases} \quad (3.9)$$

with $d = 4$. The parameters a and c depend on temperature linearly; for $T = 300$ K,

$a = 0.3$ and $c = 0.5$, and for $T = 220$ K, $a = 0.08$ and $c = 0.7$. This linear proportion to the temperature property is valid in 220 K–420 K range, and a and c are fixed with the boundary values for beyond this range.

Between 2000 cm^{-1} and 2600 cm^{-1}, we used the line shape factor of Winters et al. (1964) (See, Sect. 2.2.3.1 for detailed explanation).

In the range from 2600 cm^{-1} to 3800 cm^{-1}, the line shape factor uses the following formulae (Pollack et al. 1993)

$$\chi(v - v_0) = \begin{cases} 1 & \text{, for } |v - v_0| < 3 \text{ cm}^{-1} \\ 1.35 \exp(-|v - v_0|/10) & \text{, for } 3 \text{ cm}^{-1} \leq |v - v_0| < 10 \text{ cm}^{-1} \\ 0.614 \exp(-|v - v_0|/47) & \text{, for } 10 \text{ cm}^{-1} \leq |v - v_0| < 120 \text{ cm}^{-1} \\ 0 & \text{, for } 120 \text{ cm}^{-1} \leq |v - v_0| \end{cases} \quad (3.10)$$

which are based on the study of the collision-broadened carbon dioxide shapes by Burch et al. (1969).

In the range of 3800–4700 cm^{-1}, the formulae below is used for the line shape factor (Tonkov et al. 1996)

$$\chi(v - v_0) = \begin{cases} 1 & \text{, for } |v - v_0| < 3 \text{ cm}^{-1} \\ 1.084 \exp(-0.027|v - v_0|) & \text{, for } 3 \text{ cm}^{-1} \leq |v - v_0| < 150 \text{ cm}^{-1} \\ 0.208 \exp(-0.016|v - v_0|) & \text{, for } 150 \text{ cm}^{-1} \leq |v - v_0| < 300 \text{ cm}^{-1} \\ 0.025 \exp(-0.009|v - v_0|) & \text{, for } 300 \text{ cm}^{-1} \leq |v - v_0| \end{cases} \quad (3.11)$$

where is derived for the 2.3 μm spectral region at 296 K.

At the wavenumber larger than 4700 cm^{-1}, we adopted the formulae from Meadows and Crisp (1996) which fit the 2.3 and 1.74 μm spectral regions. The function is

$$\chi(v - v_0) = \begin{cases} 1, & \text{for } |v - v_0| < \sigma_1 = 3 \text{ cm}^{-1} \\ \exp(-B_1(|v - v_0| - \sigma_1)), & \\ & \text{for } \sigma_1 \leq |v - v_0| < \sigma_2 = 10 \text{ cm}^{-1} \\ \exp(-B_1(\sigma_2 - \sigma_1) - B_2(|v - v_0| - \sigma_2)), & \\ & \text{for } \sigma_2 \leq |v - v_0| < \sigma_3 = 90 \text{ cm}^{-1} \\ \exp(-B_1(\sigma_2 - \sigma_1) - B_2(\sigma_3 - \sigma_2) - B_3(|v - v_0| - \sigma_3)), & \\ & \text{for } \sigma_3 \leq |v - v_0| < v' = 150 \text{ cm}^{-1} \\ \exp(-B_1(\sigma_2 - \sigma_1) - B_2(\sigma_3 - \sigma_2) - B_3(v' - \sigma_3)), & \\ & \text{for } v' < |v - v_0| \end{cases} \quad (3.12)$$

where B_i depends on temperature and follows the below equation

$$B_i(T) = \alpha_i + \beta_i \exp[-\epsilon_i T], \quad (3.13)$$

and Table 3.3 values.

Figure 3.10 shows these five line shaper factors along the wavenumber difference from the line center (dv, from -200 to $+200$ cm^{-1}) in the x-axis. The line shape factor has a range from 0.0 to 1.0 and it is multiplied to Voigt line contour. All of them decrease quickly as it goes further from the line center with diverse shapes.

The CO_2 absorption is calculated using the three dimensional matrix as explained at the beginning of this session. The database matrix for the calculation of CO_2 absorption
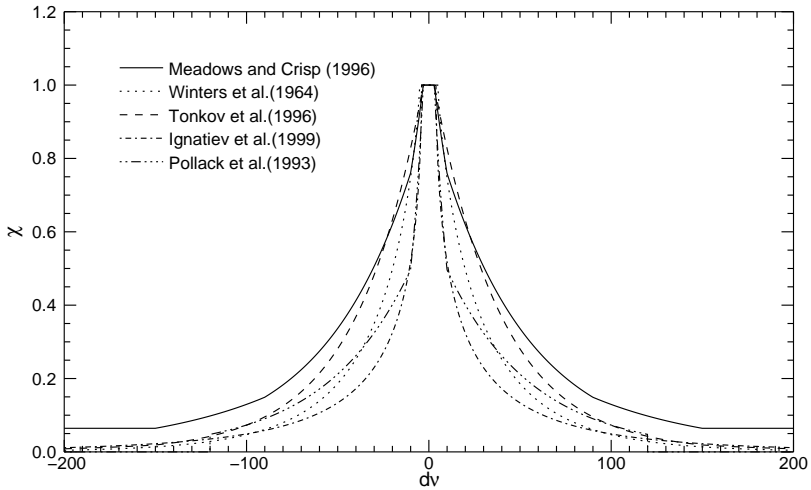
Figure 3.10: Comparison of five line shape factors from the line center ($dv = 0$) to the far wing ($dv = 200$ cm^{-1}). Atmospheric conditions are fixed as 1 bar and 280 K. Solid line – Meadows and Crisp (1996), dotted line – Winters et al. (1964), dashed line – Tonkov et al. (1996), dash-dotted line – Ignatiev et al. (1999), and dash-dot-dot-dotted line – Pollack et al. (1993).

is based on a self-broadening coefficient, Voigt contour with five line shape factors, and the cutoff value of 200 cm^{-1}. CO_2 absorption coefficient of every 1 km altitude grid is derived from the database matrix. Our calculations were validated by comparison with the database developed for radiance spectrum calculation by Ignatiev (personal communication). This database was applied for the analysis of Venera and Venus Express infrared spectrum (Ignatiev et al. 1999, 2009). Figure 3.11 shows the comparison of CO_2 absorption coefficient in spectral range from 50 to 8000 cm^{-1} under the assumption of 100% CO_2 atmosphere. The spectra for three altitudes are shown: below cloud layer (20 km), near to the cloud base (50 km), and near to the cloud top (68 km). These absorption coefficient spectra show strong similarities. Some differences in the band wings are caused by different line parameter sources and cutoff values. These figures represent a promising result for the use of this database for deep atmospheric gaseous absorptions with 1 km vertical resolution and broader wavenumber ranges.

Table 3.3: Coefficients for the shape of lines (Meadows and Crisp 1996)

I	α_i	β_i	ϵ_i
1	0.090	−0.16	0.0041
2	−0.014	0.0526	0.00152
3	0.014	0.0	0.0

(a)

(b)

(c)
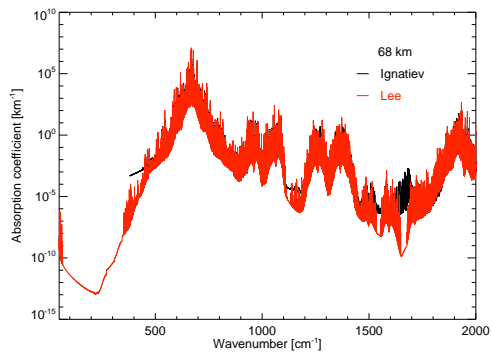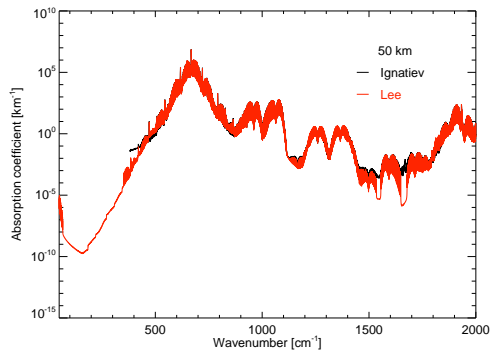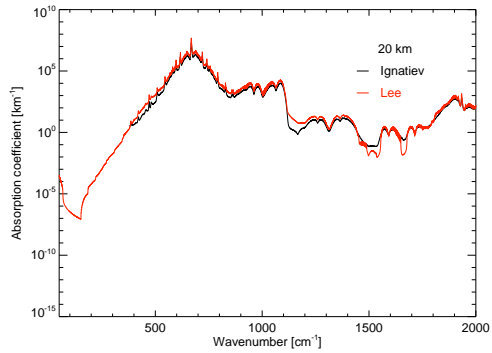
Figure 3.11: Comparison of the absorption coefficient spectra of CO_2 of this study (red line) with the database of Ignatiev (black line, private communication). (a)–(c) are in the range of 50–2000 cm^{-1}, and (a) is the values of 20 km, (b) is 50 km, and (c) is 68 km altitude layers.
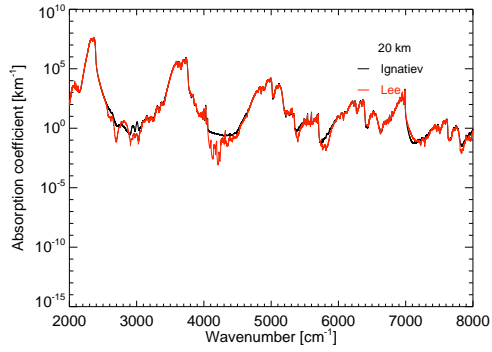
(d)
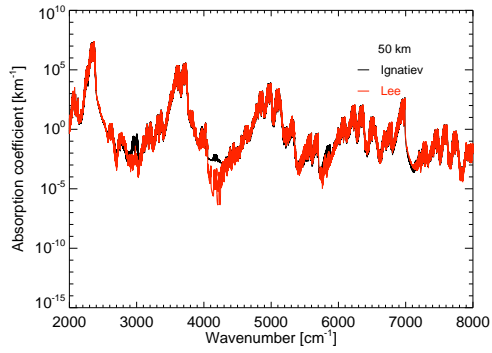
(e)
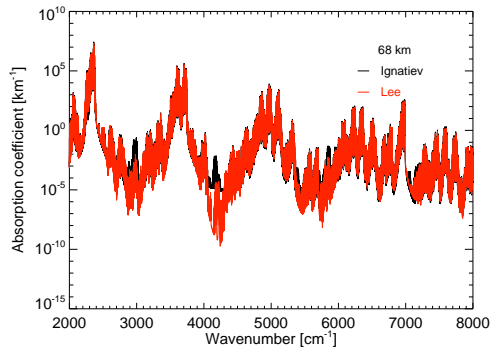
(f)

Figure 3.11: *(continued)*, (d)–(f) are in the range of 2000–8000 cm^{-1}. (d) is the values of 20 km, (e) is 50 km, and (f) is 68 km altitude layers.

Water vapor and sulfur dioxide absorption calculation

The HITRAN2008 spectroscopic database provides air-broadened and self-broadened half-widths (Rothman et al. 2009). Air-broadening is based on the Earth atmospheric composition (N_2 78%, O_2 21%, and CO_2 0.04%), that cannot be directly applied for Venus' (CO_2 96.5% and N_2 3.5%). The CO_2-broadened half-widths for the trace gases are not well constrained. The measurement results in the CO_2-broadened half-widths for H_2O lines suggested using the scaling factor to the air-broadened half-width, but it varied from 1.3 to 2.0 (Gamache 1995), or from 0.95 to 3.07 with an average of 1.67 (Brown et al. 2007). Fedorova et al. (2008) used the scaling factor of 1.7 to multiply the air-broadened half-width from the HITRAN2004 database to account for the H_2O broadening lines in the Venus atmosphere. We adopt this scaling factor of 1.7 for the H_2O lines. SO_2 is assumed as air-broadened half-width due to lack of data. Both H_2O and SO_2 used Voigt line shape, and cutoff value is set as 100 cm^{-1}.

3.2.1.2   Spectral sub-intervals for thermal emission calculation

For convenience, we divided a broad wavenumber range into several sub-intervals. This is necessary to strike a balance between the needs of high spectral resolution and efficient computing. First, it is necessary to keep sufficient spectral resolution, at least around 0.1 cm^{-1}, to take into account the clear signal of gaseous absorption lines. Second, the process requires reasonable computing time to undergo several tests for the input data and parameters checking for routines. Since SHDOM requires adjusted accuracy parameters, which can result in unstable results due to tremendous extinction, depending on the wavenumbers, sub-intervals are suitable for using SHDOM in a line-by-line method. To accomplish this, sub-intervals are divided according to the CO_2 absorption band.

The strong absorption band of CO_2 overwhelms those of other gases. Nevertheless, minor gases can be important in the range of weak CO_2 absorption. Figure 3.12 presents the CO_2 absorption cross section in the 50–10,000 cm^{-1} range. We set a standard value with the median, 10^{-25} [cm^2/molecule], to distinguish the strong and weak absorptions of CO_2. Division in sub-interval (Table 3.4) is based on this spectrum. The table marks strong CO_2 bands and minor gas bands together. L2–3 and L4–6 contain strong CO_2 bands at 15 μm and 4.3 μm, respectively. L1–2 and L3–4 have comparably weak CO_2 absorptions and minor gases become important sources. L5 is 2000 cm^{-1} (5 μm) within L4–6, and it represents a boundary between thermal flux dominant area and the solar flux dominant area. The 50–2590 cm^{-1} (3.86–200 μm) range, L1–6, is used for the calculation of thermal emission calculation, L5–16 range will be employed in the solar heating calculation.

3.2.1.3   Rayleigh scattering

Rayleigh scattering considers a limited case of very small particles, which are much smaller than the wavelength of the incident radiation (Hansen and Travis 1974, Goody and Yung 1989). This scattering is caused by the polarizability of small particles. For this reason, Rayleigh scattering is applied to the gaseous molecular scattering in planetary atmosphere (Hansen and Travis 1974). Under the assumption that the scattered radiation corresponds to that emitted by the dipole and a scalar polarizability (α) for a sphere, the

scattering coefficient per particle (s_n) can be expressed as

$$s_n = \frac{1}{2}\left(\frac{2\pi}{\lambda_0}\right)^4 |\alpha|^2 \int \frac{1}{2}(1 + \cos^2\theta)d\omega$$
$$= \frac{8\pi}{3}\left(\frac{2\pi}{\lambda_0}\right)^4 |\alpha|^2 \tag{3.14}$$

where θ is the scattering angle (Goody and Yung 1989). The polarizability tensor is $\alpha = (m-1)/(2\pi N)$, where m is a complex refractive index and N is the number density of molecule. This equation shows that Rayleigh scattering coefficient is inversely proportional to the fourth-power of the wavelength. Rayleigh scattering increases quickly going toward shorter wavelengths.

The Rayleigh scattering optical thickness of the atmosphere can be expressed as pressure in a simplified form. From h to the top of atmosphere, the optical thickness of Rayleigh scattering (τ_R) caused by atmospheric gases is

$$\tau_{R,\lambda}(h) = \int_h^\infty \rho \frac{s_{n,\lambda}}{\bar{\mu}}dh' \tag{3.15}$$

where $\frac{s_{n,\lambda}}{\bar{\mu}}$ is the scattering coefficient per unit mass, $\bar{\mu}$ is the mean molecular mass, and ρ is the density of gases. Equation 3.15 can be combined with the assumption of hydrostatic equilibrium ($P(h) = \int_h^\infty g\rho dh'$) (Hansen and Travis 1974)

$$\tau_{R,\lambda}(h) = \frac{P(h)s_{n,\lambda}}{g\bar{\mu}}$$
$$= \tau_{R0,\lambda}\frac{P(h)}{P_0} \tag{3.16}$$
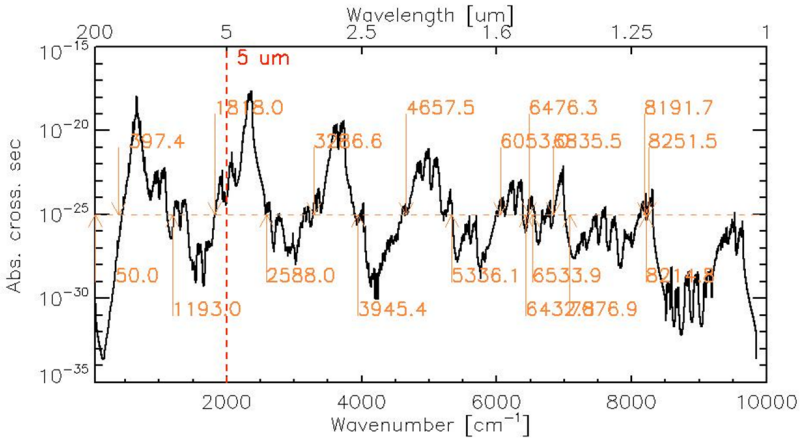
Figure 3.12: CO_2 absorption cross section [cm^2/molecule] along the wavenumber at 350 K and 10 bar condition. The locations of sub-interval ranges are marked along the wavenumber.

Table 3.4: Sub-intervals in the 50–50000 cm^{-1} (0.2–200 μm) range. CO_2 bands are marked with yellow arrows. The locations of H_2O and SO_2 bands are marked with red arrow, which does not overlap with CO_2 bands, and blue arrow, which overlaps with CO_2 bands. UV unknown absorber is shown in L15–L16 range. L5, 2000 cm^{-1} (5 μm), is the boundary of thermal and solar radiation. L1–L6 range is considered for the thermal emission calculation.

Wavenumber [cm-1]	marks	CO_2	H_2O	SO_2	UV unknown absorber
50 (= 200 μm)	L1				
390	L2		↕	↕	
1190	L3	↕			
1810	L4		↕	↕	
2000 (= 5 μm)	L5	↕			
2590	L6			↕	
3000	L7	↕	↕		
3950	L8	↕	↕	↕	
4650	L9	↕		↕	
5340	L10	↕	↕		
6050	L11	↕	↕		CO$_2$ bands ↕
7080	L12	↕		↕	overlapped by CO$_2$ ↕
8190	L13	↕	↕		non-overlapped CO$_2$ ↕
8300	L14				comparably weak ↕↕
26000 (=0.385 μm)	L15		↕	↕	
50000 (= 0.2 μm)	L16		↕	↕	

where $\tau_{R0,\lambda}$ is the Rayleigh optical thickness for whole atmosphere, P_0 is the pressure at the surface and the formulae above neglects the altitude dependencies of $s_{n,\lambda}$, $\bar{\mu}$, and g. The Rayleigh optical thickness above h altitude becomes a simple function of pressure (Pollack 1967).

The parameters can be adjusted for Venus atmosphere [followed Hansen and Travis (1974)'s parameters]: the depolarization factor for nonspherical molecules (Goody and Yung 1989) is ~0.09 under the assumption of pure CO_2 atmosphere, the mean molecular mass is ~ $44 \times 1.66 \times 10^{-24}$ g, the surface pressure is ~93 atm, the gravity is ~8.7 m/s^2, and other parameters from Allen (1964), then τ_{R0} is simplified as a function of wavelength

$$\tau_{R0}(\lambda) = 1.527\lambda^{-4}(1 + 0.013\lambda^{-2}), \qquad (3.17)$$

where λ is in the unit of μm (Hansen and Travis 1974).

Table 3.5 compares the Rayleigh scattering from Eq. 3.16 (Hansen and Travis 1974), τ_{HT}, and another theoretical values (Moroz 2002), τ_M, which had been used to analyze Venera observation. These two Rayleigh optical thicknesses are compared in Table 3.5, of VIRA model in the three wavelength channels. Equation 3.16 and Moroz (2002)'s data produce comparable values. Since Eq. 3.16 is easy to apply at different altitudes and at

other wavelengths, this study use this equation to get the values of molecular scattering amounts in the deep atmosphere.

Table 3.5: Comparison of Rayleigh optical thickness along the altitude for selected wavelengths between derived values from Eq. 3.16 (τ_{HT}) and values from Moroz (2002) (τ_M)

h (km)	P (bar)	Rayleigh optical thickness from the surface to h km ($=\tau_{R0} - \tau_R(h)$)					
		$\lambda = 0.65\ (\mu m)$		$\lambda = 0.85\ (\mu m)$		$\lambda = 1.02\ (\mu m)$	
		τ_M	τ_{HT}	τ_M	τ_{HT}	τ_M	τ_{HT}
0	92.1	0.0	0.0	0.0	0.0	0.0	0.0
2	81.1	0.97	1.054	0.33	0.356	0.16	0.171
4	71.2	1.84	2.001	0.62	0.676	0.3	0.324
8	54.4	3.32	3.606	1.12	1.218	0.54	0.584
16	70.7	5.42	5.882	1.83	1.987	0.88	0.953
30	9.6	7.28	7.9	2.46	2.668	1.18	1.28
45	2.0	7.95	8.628	2.48	2.914	1.29	1.398

3.2.1.4 Extinction of heterogeneous atmosphere

The atmospheric parameters, e.g. temperature, extinction, phase function, and single scattering albedo, need to be specified for the radiative transfer calculations. The optical properties of each atmospheric agent are prepared through Sect. 3.1.2 and Sect. 3.2.1.1–3: four-mode particle size distributions, and absorption cross sections of gases and molecular scattering. Since atmosphere contains many opacity sources, we re-define optical properties in every grid points as a mixture of opacity sources. Under the assumption of the external mixture of aerosols (Levoni et al. 1997), the mean aerosol extinction coefficient, and asymmetric factor are described as follows:

$$E(z) = \frac{\sum_j N_j(z)E_j(z)}{\sum_j N_j(z)},$$

$$g(z) = \frac{\sum_j N_j(z)S_j(z)g_j(z)}{\sum_j N_j(z)S_j(z)},$$

(3.18)

where E is extinction coefficient, g is asymmetry factor, N is the number density, S is the scattering coefficient, and j is index for each mode of aerosol.

While we take into account contributions from both gases and aerosols for calculating

the single scattering albedo:

$$\omega(z) = \frac{\text{rayleigh scattering} + \sum_j E_j(z)\omega_j(z)}{\text{gaseous extinction} + \sum_j E_j(z)}. \tag{3.19}$$

Summary

Atmospheric thermal structure and optical properties of agents in the broad spectral range have been discussed in this chapter. The temperature profile and pressure profile are combined the Venus International Reference Atmosphere (VIRA) and the observation data from the radio occultation experiment VeRa/Venus Express into the ~5° latitude bin from equator to the pole. Cloud structure uses four mode size distributions (Chapter 3.1). CO_2, H_2O, and SO_2 have been taken account for the atmospheric gases. We improve gaseous absorption coefficient database for the model calculation which had been used in Chapter 2. Line parameters are selected to adjust to the Venus atmosphere and the spectral range. The sub-interval division of a broad spectral range and simplified Rayleigh scattering are introduced for the calculation convenience. The weighting average is considered for the radiative transfer calculation in the heterogeneous atmosphere.

These data will be used in the thermal flux calculation in Chapter 4. While the atmospheric gases, and the middle and lower cloud layers are latitude independent, the upper cloud layer will be considered as a free variable to calculate the sensitivity of thermal emission in the mesosphere. For the meridional trend of the thermal fluxes and cooling rates, the averaged latitudinal upper cloud structure will be taken from Chapter 2.

4 Thermal emission and cooling rate in the Venus atmosphere

The thermal radiation field depends on the atmospheric temperature structure and the distribution of opacity sources. Since many atmospheric parameters affect the thermal radiation, one needs to perform comprehensive radiative transfer modeling in order to determine the relative contribution of the different parameters. In this chapter we analyze the effects of each atmospheric parameter on the thermal flux, using the atmospheric temperature and cloud models specified in Chapter 3. First, we compare the brightness spectra calculated from models with different atmospheric conditions. Then we present the thermal flux integrated over the entire thermal-IR range. The sensitivity of the thermal flux to the cloud top structure is evaluated for different temperature conditions, in order to identify the radiative effects of cloud top structure. The vertical profile of the thermal flux cannot be obtained from remote sensing, and there have been only a few in-situ measurements by descent probes in limited wavelength ranges. Therefore, modeling is necessary to understand the radiative field structure. We end this chapter with a cooling rate calculation based on the averaged cloud top parameters derived from observation (Chapter 2).

4.1 Thermal flux

Thermal emission cools the atmosphere, and determines the outgoing energy flux from a planetary atmosphere to space. It is effective in the IR range ($\sim$4–200 μm), corresponding to the 120 K–735 K temperature range of the Venus atmosphere. We use this broad band in our simulations. Solar radiation is not included in this calculation.

4.1.1 Thermal emission spectra and profiles

Monochromatic flux profiles and radiance spectra are calculated for the atmospheric models described in Chapter 3. First, we use the low latitude temperature structure to confirm the radiative response of atmospheric extinction agents in the brightness temperature spectrum and wavenumber-integrated flux profile. The temperature at low latitude decreases monotonically with altitude. The model spectrum for this temperature profile can be easily interpreted, unlike spectra for peculiar temperature structures like the temperature inversion at the cold collar and the isothermal layer at the pole. The sensitivity of thermal emission to different atmospheric agents is studied through these controlled cases: gases free, cloud free, H_2O and SO_2 free, CO_2 free, H_2O free, and SO_2 free conditions. Second,

Table 4.1: Description of atmospheric model conditions with abbreviations. Three thermal structures are used: low latitude, the cold collar, and polar region. The atmospheric gaseous composition and the cloud top structure parameters are controlled.

Model Abbreviation	Thermal structure	The atmospheric gaseous composition and the cloud top structure
L *(L-CHScld)*	Low latitude (27.5°S)	CO_2, H_2O, and SO_2 Averaged cloud top structure in low-middle latitude region ($Z = 67.1$ km, $H = 3.8$ km)
L-CHS		CO_2, H_2O, and SO_2 Cloud free
L-cld		Gases free Averaged cloud top structure in low-middle latitude region
L-Ccld		CO_2 Averaged cloud top structure in low-middle latitude region
L-HScld		H_2O and SO_2 Averaged cloud top structure in low-middle latitude region
L-CScld		CO_2 and SO_2 Averaged cloud top structure in low-middle latitude region
L-CHcld		CO_2 and H_2O Averaged cloud top structure in low-middle latitude region
*L-Z**H##*		CO_2, H_2O, and SO_2 Cloud top structure: $Z =$** km and $H =$ #.# km
C	Cold collar (62.5°S)	CO_2, H_2O, and SO_2 Averaged cloud top structure in the cold collar region ($Z = 64.7$ km, $H = 2.1$ km)
*C-Z**H##*		CO_2, H_2O, and SO_2 Cloud top structure: $Z =$** km and $H =$ #.# km
P	Pole (87.5°S)	CO_2, H_2O, and SO_2 Averaged cloud top structure in polar region ($Z = 62.8$ km, $H = 1.7$ km)
*P-Z**H##*		CO_2, H_2O, and SO_2 Cloud top structure: $Z =$** km and $H =$ #.# km

we proceed with calculations on the radiative effects of the upper cloud structure. The sensitivity of the thermal flux to the cloud top parameters is determined for three typical atmospheric thermal structures: low latitude, the cold collar, and polar regions (Fig. 3.1).

Table 4.1 gives the details of the atmospheric models, e.g. temperature structure, gaseous composition, and the upper cloud structure parameters. In this study we include three gases (CO_2, H_2O, and SO_2), which are the strongest greenhouse gases in the Venus

atmosphere (Pollack et al. 1980a). Note that there are two free parameters for the upper cloud structure, altitude of the cloud top Z and aerosol scale height H, which will be used repeatedly in this chapter. The averaged parameters of the upper cloud structure are given in Table 2.2 (Chapter 2).

4.1.1.1 Thermal emission spectrum at the top of atmosphere

The synthetic radiance spectrum at the top of the atmosphere was calculated for low latitude conditions. Figure 4.1 compares the outgoing spectra calculated from model *L-CHS*, *L-cld*, *L-Ccld*, and *L-HScld*, which are presented in the brightness temperature spectrum (Appendix C). Model *L-CHS* shows cloud-free condition, and the brightness temperature reaches values as high as 430 K, corresponding to thermal radiance originating in the deep atmosphere (below 40 km altitude). Although this spectrum has the highest brightness temperature among the four models, emission from the hot surface (735 K) is still blocked by atmospheric gases. Model *L-cld*, which takes only aerosol opacity into account, shows a relatively flat spectrum that is following the cloud top temperature
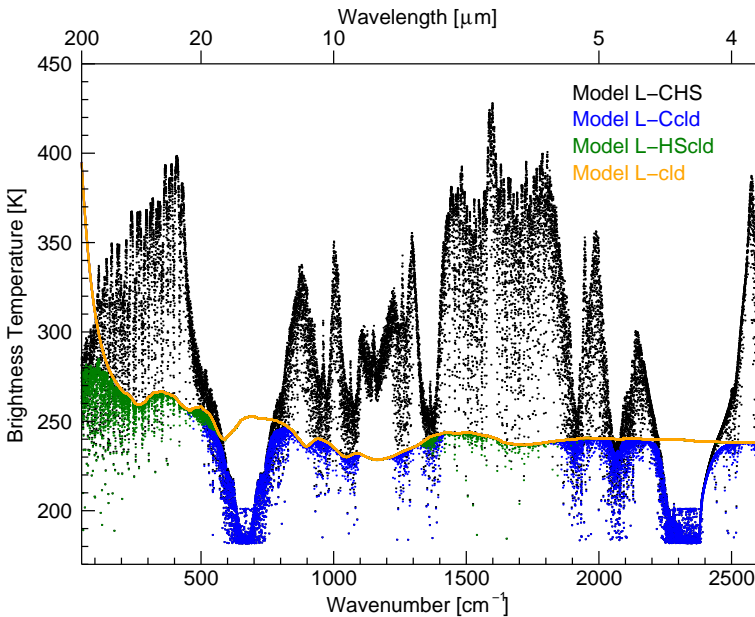

Figure 4.1: Synthetic brightness temperature in the 50–2590 cm^{-1} wavenumber range. Low latitude thermal condition have been adopted (model *L*). Four model spectra are compared: *L-CHS* (black), *L-Ccld* (blue), *L-HScld* (green), and *L-cld* (yellow). The models are described in Table 4.1.

($\sim$240 K) in the wavenumber>500 cm^{-1} range. The brightness temperature increases toward small wavenumbers (<200 cm^{-1}), which is caused by reduced H_2SO_4 opacity (see, Fig. 3.3 in Sect. 3.1.2). The other two spectra are results for model *L-Ccld* and *L-HScld*. Model *L-Ccld* includes cloud aerosol and CO_2, but lacks H_2O and SO_2[1]. Pronounced CO_2 absorption bands are seen at 2349 cm^{-1} (4.3 μm) and 667 cm^{-1} (15 μm), as well as at 961, 1064, 1259, 1366, 1932, and 2083 cm^{-1}. Model *L-HScld* shows the bands of H_2O at 1590 cm^{-1} (6.3 μm) and in the 50-475 cm^{-1} range, and that of SO_2 at 50, 519, and 1360 cm^{-1}, but the bands are weaker than those of CO_2 due to the very low abundance above the cloud tops[2]. In the wavenumber range<200 cm^{-1}, there is significant absorptions by H_2O and SO_2. However, the effects of H_2O and SO_2 on the radiative energy balance are small compared to that of CO_2 because the thermal emission is low in this wavenumber range (see Appendix C for the ra diative flux spectrum).

Figure 4.1 illustrates two important facts. Firstly, clouds block the thermal emission from the deep atmosphere, creating a strong greenhouse effect (compare to the cloud-free model *L-CHS*). Strong absorption by gases reduces the brightness temperature to less than 430 K, from the high surface temperature (735 K). The cloud deck reduces the brightness temperature further, from $\sim$430 K to $\sim$240 K. The presence of clouds decreases the brightness temperature by up to 190 K, which produces thermal heating at cloud levels. Without clouds, a great amount of thermal energy can escape to space. Secondly, gases affect the thermal emission even above the cloud level. Gases generate absorption bands (compare models *L-Ccld* and *L-HScld* to *L-cld*). The results indicate that gaseous absorptions are important not only in the deep atmosphere, but also in the mesosphere. Especially the strong CO_2 absorptions at 667 cm^{-1} and 2349 cm^{-1} are effective up to 120 km altitude. This strong absorption results in a flat feature in synthetic spectrum at the center of these CO_2 bands instead of scattered feature. It is caused by the altitude range of this model which is limited to 100 km altitude. The real temperature structure can be variable between 120 K and 220 K in the 100–120 km altitude range, as shown in Fig. 1.1.

4.1.1.2 Flux profile in a narrow wavenumber range

We compare the upward and downward flux altitude profiles in selected wavenumber ranges between the cloud condition and the cloud-free condition (models *L* and *L-CHS*) for low latitude temperatures. The monochromatic flux profile is very sensitive to the absorption properties at a particular wavelength, and therefore can be very different at the center of an absorption line compared to the continuum. Therefore, for the comparison we integrate the flux over a 10 cm^{-1} wavenumber range instead of using a monochromatic flux profile. We select five spectral ranges: three of them are centered at absorption bands of H_2O, SO_2, and CO_2 (strong absorption), one range is in the wing of a strong CO_2 band (intermediate absorption), and the last spectral range is chosen to be free from strong gaseous absorption bands. They are 250–260 cm^{-1} for the H_2O band, 515–525 cm^{-1} for the SO_2 band (at 519 cm^{-1}), 660–670 cm^{-1} for the center of CO_2 band (at 667 cm^{-1}), 600–610 cm^{-1} for the wing of the strong CO_2 band (at 667 cm^{-1}), and 1600–1610 cm^{-1} for the region which is free from strong gaseous absorption.

Figure 4.2 shows five pairs of upward and downward flux profiles as a function of

---

[1]This neglects a chemical reaction for the cloud formation, so cloud exists without H_2O and SO_2.
[2]The 1150 cm^{-1} SO_2 band overlaps with the liquid sulfuric acid band
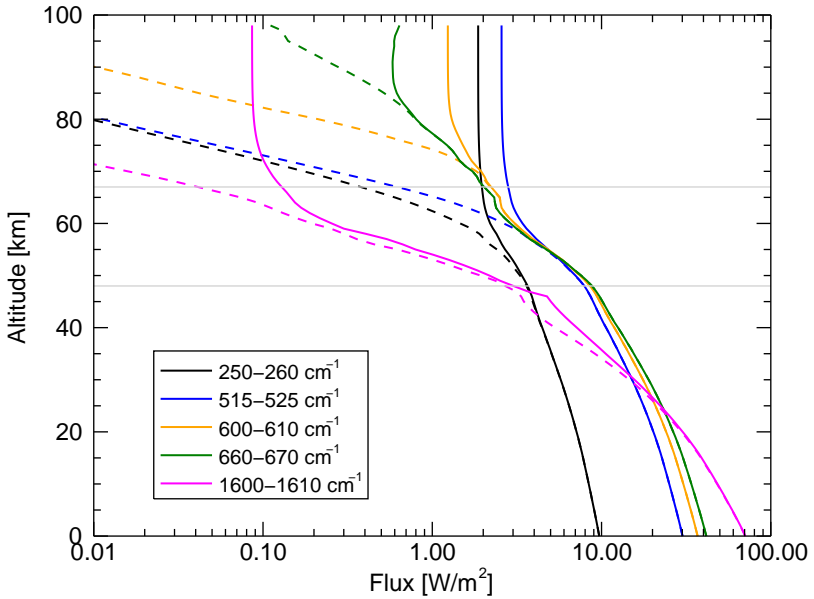
Figure 4.2: Five pairs of wavenumber-integrated upward (solid) and downward (dashed) flux profiles. The five selected narrow wavenumber ranges are 250–260 cm^{-1} (black), 515–525 cm^{-1} (blue), 600–610 cm^{-1} (yellow), 660–670 cm^{-1} (green), and 1600-1610 cm^{-1} (magenta). The cloud top altitude is 67 km and the base altitude is 48 km (gray solid lines).

altitude. The cloud deck occupies the 48–67 km altitude range. The slopes of the flux profiles are different due to the wavenumber dependency of the thermal emission (see Appendix C for more detail). The difference between the up- and downward fluxes is the net flux, and it is close to zero in the deep atmosphere due to extremely high gaseous opacity. The net flux in the 1600–1610 cm^{-1} wavenumber range ('gaseous absorption free') becomes non-zero above 20 km altitude. Although this narrow wavenumber range does not have gaseous absorption lines, it is affected by nearby gaseous absorptions due to their strong pressure broadening in the deep atmosphere. Compared to other ranges, the net flux in this range is sensitive to cloud opacity, so that the vertical gradient of the net flux decreases at the base of cloud, and increases near the cloud top. In the 660–670 cm^{-1} wavenumber range (CO_2 band center) the net flux becomes non-zero above 80 km altitude, which is far above the cloud top. The net flux in the 600–610 cm^{-1} wavenumber range (CO_2 band wing) is also non-zero above the cloud tops and increases upward. These imply that clouds do not affect the thermal flux in these ranges, as CO2 absorption dominates, and they induce radiative cooling in the mesosphere. There is an increasing tendency of the upward flux above 90 km altitude following the temperature
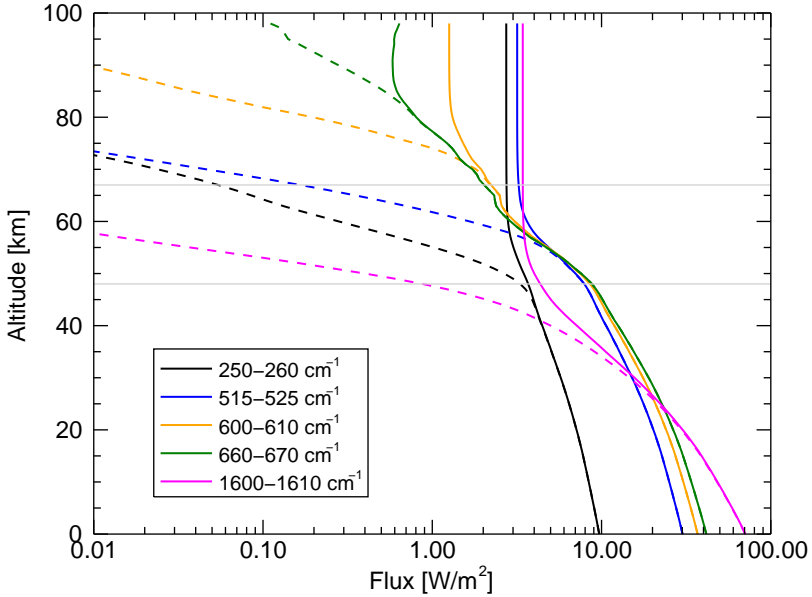
Figure 4.3: Same as in Fig. 4.2, but calculated for cloud-free conditions (model *L-CHS*).

profile, and it is caused by CO_2 thermal emission[3].

Aerosol extinction decreases for wavenumbers below 1000 cm^{-1} (Fig. 3.3 in Chapter 3) sufficiently for the opacity of the SO_2 and H_2O gases to become noticeable. The downward flux in the SO_2 band (515–525 cm^{-1}) decreases quickly above 55 km altitude, following the decrease in the SO_2 mixing ratio (Fig. 3.9 in Sect. 3.2.1.1). Likewise, the downward flux in the H_2O band (250–260 cm^{-1}) decreases above 45 km, following the decrease in the H_2O mixing ratio (Fig. 3.9). However, the outgoing flux is also reduced by the presence of clouds, almost by a factor of two when compared to cloud-free conditions.

A comparison between Fig. 4.2 and Fig. 4.3 illustrates the influence of clouds on the net thermal flux. The most significant change is for the outgoing flux in the 1600–1610 cm^{-1} wavenumber range, which increases from 0.09 W/m^2 with clouds to 3.42 W/m^2 without clouds. The upward flux in minor gas bands (250–260 cm^{-1} and 515–525 cm^{-1}) also increases in cloud-free conditions. There are negligible changes in the 600–610 cm^{-1} and 660–670 cm^{-1} wavenumber ranges, showing that the flux here is almost independent of clouds.

4.1.1.3 Radiative effects of opacity agents in the sub-intervals

We integrate monochromatic fluxes within the sub-intervals, which divide a broad spectral range according to a presence of CO_2 bands (Sect. 3.2.1.2). Based on low latitude thermal

---

[3]Fig. D.2 shows the effective altitude of CO_2 absorption reaches above 90 km altitudes.

conditions, several atmospheric compositions are tested within sub-intervals. Table 4.2 shows the contribution of different opacity sources to the outgoing thermal flux integrated over the sub-intervals. Model L gives the outgoing net flux for the low latitude model (the second column of the table). The response to cloud-free conditions is retrieved from model L-CHS in the third column of the table, and demonstrates strong radiative effect of clouds in the L2–4 sub-interval. Clouds affect the outgoing thermal emission mostly in this sub-interval. The radiative effects of all gases combined are found by subtracting the results of the gases-free model L-cld from those of model L. The same was done for each gas individually (the three right-most columns of the table). Note that gaseous radiative effects in the table correspond to the layer above the cloud tops, because clouds block the thermal emissions from the deep atmosphere effectively. This is the reason for the relatively small values for gaseous contributions compared to that of the clouds. CO_2 absorption is negligible in the L1–2 sub-intervals, but becomes dominant among gases in L2–3 and L4–6. H_2O and SO_2 are the dominant opacity sources in the L1–2 sub-interval. Results for the L3–4 sub-interval show the importance of minor gases as well as a high CO_2 contribution, but the effect of CO_2 is weaker than that in L2–3 or L4–6. The summation of the contribution of each of the gases is not equal to the result of the 'all gases' case because absorption lines of different gases overlap.

Table 4.2 only lists the flux as observed at the top of the atmosphere. We will now compare the flux profiles as a function of altitude for our controlled cases. The L2–3 and L3–4 sub-intervals are selected for the comparison because both show strong radiative cloud effects, while the L2–3 sub-interval contains strong CO_2 absorption and the L3–4 sub-interval contains relatively strong H_2O and SO_2 absorptions.

Figure 4.4 shows the wavenumber-integrated flux profiles in the L2–3 sub-interval. This sub-interval contains the largest part of the outgoing thermal flux within the entire

Table 4.2: The changes of net flux (W/m^2) at the top of the atmosphere in each sub-interval. The net flux F_{net} of model L is given in the second column. The contributions of agents are derived by subtracting $F_{net,agentfree}$ from F_{net}. Negative means the net flux is reduced due to an agent.

Sub-interval	F_{net} of model L	Contribution of each agent to the outgoing flux [W/m^2] ($=F_{net} - F_{net,agentfree}$)				
		Clouds	Gases			
			All gases	CO_2	H_2O	SO_2
L1–2	52.379	−29.600	−1.322	0.000	−1.015	−0.056
				0.0%*	76.7%*	4.2%*
L2–3	101.149	−82.656	−26.102	25.492	−0.060	−0.300
				97.7%*	0.2%*	1.1%*
L3–4	9.027	−98.658	−0.270	−0.181	−0.037	−0.035
				67.0%*	13.9%*	13.1%*
L4–5	0.395	−6.654	−0.036	−0.035	−0.001	0.000
				97.0%*	1.5%*	0.0%*
L5–6	0.178	−1.168	−0.111	−0.110	0.000	0.000
				99.8%*	0.0%*	0.0%*

* Percentage of the 'All gases' contribution.
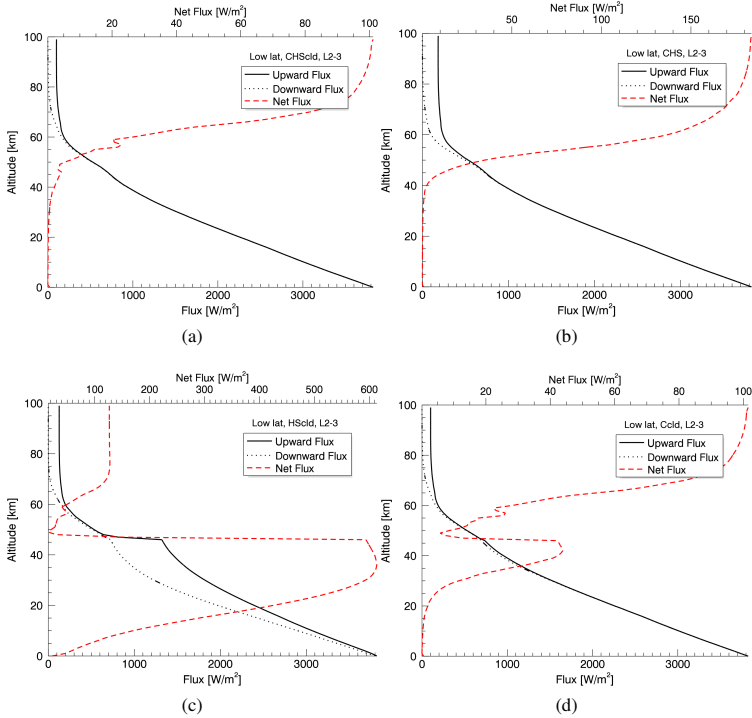
Figure 4.4: Wavenumber-integrated vertical flux profiles in the L2–3 sub-interval. The low latitude thermal structure has been adopted. Upward (black solid line) and downward (black dotted line) fluxes are shown. The net flux (red dashed line) is obtained by subtracting the downward flux from the upward flux. Note that the upper x-axis is for the net flux and the lower x-axis is for the up- and downward fluxes. Shown are the results for (a) the low latitude model with all agents (*L-CHScld* or *L*), (b) cloud-free conditions (*L-CHS*), (c) CO_2-free conditions (*L-HScld*), and (d) H_2O and SO_2-free conditions (*L-Ccld*). In the legend, 'Low lat' refers to the low latitude temperature condition.

range (according to the 'model *L*' value in Table 4.2), and has a strong CO_2 absorption band (15 μm). Figure 4.4 compares the result of model *L* in the (a) sub-panel with three controlled cases (b–d). The strong CO_2 thermal emissions are shown in Fig. 4.4(a), (b), and (d), through the increasing net flux above the cloud top altitude (67 km). Figure 4.4(c) shows a large net flux of ~600 W/m² below the clouds due of the absence of CO_2. The net flux quickly decreases at the cloud base, which implies a sudden thermal heating by the clouds. The absence of minor gases also can induce thermal heating at the cloud base. Figure 4.4(d) shows a net flux of ~45 W/m² below the clouds, which decreases to ~5 W/m² at the cloud base. This suggests that the radiative effects of minor gases are
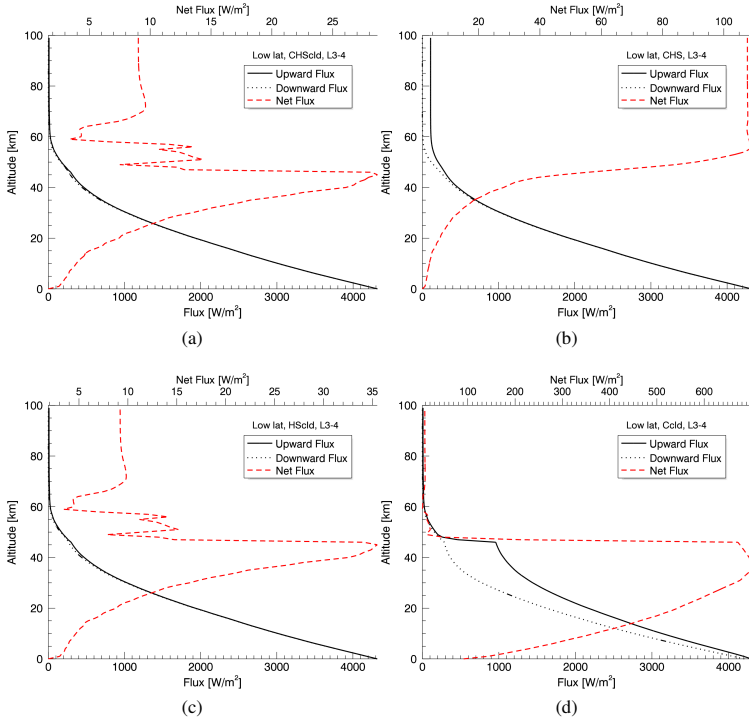
Figure 4.5: Wavenumber-integrated flux profiles in L3–4 sub-interval. Notations are the same as for Fig. 4.4.

not negligible in the deep atmosphere, even though CO_2 is a major opacity source in this sub-interval.

Figure 4.5 compares the same conditions as shown in Fig. 4.4, but for the L3–4 sub-interval. The thermal emission in this sub-interval is huge, more than 4000 W/m^2 at the surface, and decreases with altitude to ∼200 W/m^2 at the cloud top and ∼10 W/m^2 at 99 km altitude. The net flux structure exhibits a fluctuation due to the cloud vertical structure. The cloud-free model *L-CHS* in Fig. 4.5(b) shows that the upward flux at 99 km increases by an order of magnitude compared to the model with all agents in (a). This implies that in the L3–4 sub-interval, clouds have a stronger radiative effect on thermal emission than in L2–3. The net flux of model *L-CHS* is almost constant at ∼110 W/m^2 above 50 km while it slopes steeply downward towards ∼40 km altitude, which suggests that gaseous thermal cooling can be strong in the 40–50 km altitude range. Model *L-HScld* in Fig. 4.5(c) shows a small (∼7 W/m^2) net flux increase below the clouds compared to (a). This implies that the radiative effect of CO_2 is weaker in the L3–4 sub-interval than in L2–3. A significant change is shown for model *L-Ccld* in Fig. 4.5(d), which shows

that the net flux increases to ~700 W/m^2 below the clouds when H_2O and SO_2 are absent (although the overall thermal radiative effect of H_2O is much stronger than that of SO_2, the L3–4 sub-interval has comparable radiative effects of both H_2O and SO_2, as shown in Table 4.2). The thick clouds can reduce this increased net flux and result in strong thermal warming at the cloud base.

4.1.2 Sensitivity of the thermal flux to the cloud top structure

This chapter describes the result of calculations of the thermal flux integrated over the full wavenumber range. The controlled cases focus on the radiative effects of the cloud top structures: the cloud top altitude (Z) and the aerosol scale height (H). The averaged parameters of cloud top structure are considered as a standard model (Model L, C, and P in Table 4.1). We compare higher/lower Z and H from the standard model to evaluate the sensitivity of thermal flux to the cloud top structure. The temperature structure is another important factor which affects directly thermal emission and gaseous absorption. Therefore, the calculation of thermal emission with various cloud top parameters has been repeated for the three typical temperature profiles (low latitude, the cold collar, and pole as shown in Fig. 3.1).

While the integrated flux can give the energy amounts at every level, the spectrum of brightness temperature can provide an atmospheric condition instantaneously. Therefore, the sensitivity of thermal emissions to the cloud top parameters is shown as the following: First, the brightness temperature spectra are presented depending on the cloud top parameters. Second, the integrated thermal flux profiles are compared to analyze the vertical response of thermal emission to the change of the cloud top structures.

4.1.2.1 Low latitude

At low latitude, temperature monotonically decreases with altitude, and therefore, the temperature of the cloud top can be expressed as the function of altitude. Figure 4.6(a) shows brightness temperature spectra and demonstrate this relation between the brightness temperature and the altitude of the cloud top, by increasing cloud top altitude from 62 km to 70 km that corresponded to the decreasing of the cloud top temperature from 250 K to 230 K. The depths of absorption bands are deeper and clearer as the cloud top altitude goes down, due to increasing brightness temperature of cloud tops and longer optical depth of gases. Figure 4.6(b) compares the spectra of the outgoing radiation calculated for different values of the aerosol scale height. 1 km aerosol scale height is selected as the smallest aerosol scale height since it is the size of vertical grid, and 6 km aerosol scale height is chosen as the largest aerosol scale height because $H > 6$ km was rarely shown in the observation (Chapter 2). In this figure, especially we note the trend in the continuum spectrum between strong absorption bands. For a small aerosol scale height ($H = 1.0$ km), the brightness temperature spectrum shows the least deviations from the cloud top temperature (240 K). Since aerosol scale height corresponds to an e-folding value of cloud opacity along the altitude (Sect. 2.2.4.1) explains the opacity model for the upper cloud vertical structure), the small scale height means a clear boundary between clouds and cloud free atmosphere above. As the aerosol scale height increases (Fig. 4.6(b)) the brightness temperature spectrum deviates more and more from the cloud
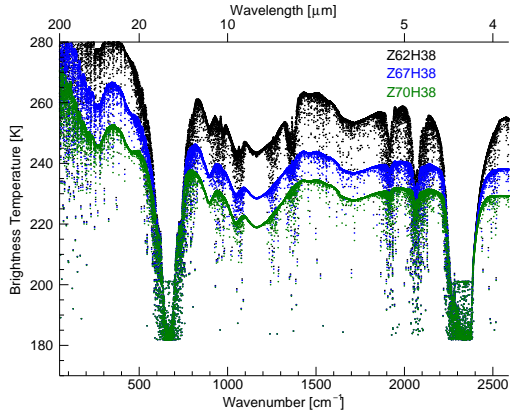
(a)
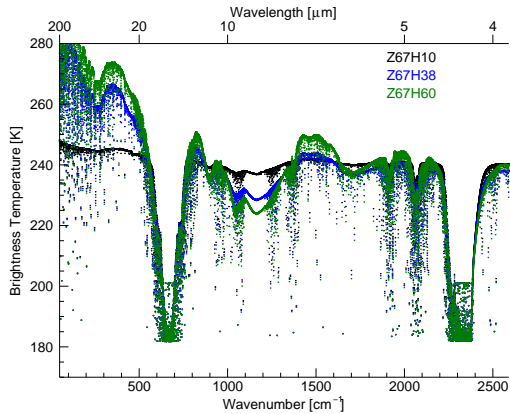
(b)

Figure 4.6: Brightness temperature spectra are calculated in the low latitude thermal struc-
ture with various cloud top parameters. The cloud top altitude is marked with 'Z' (1 km
unit) and the aerosol scale height is marked with 'H' (0.1 km unit) in the legend. (a) Three
cloud top altitudes are compared for 62 km (black), 67 km (blue), and 70 km (green) while
the aerosol scale height is fixed at 3.8 km. (b) Three aerosol scale heights are compared
for 1.0 km (black), 3.8 km (blue), and 6.0 km while the cloud top altitude is fixed at
67 km. 67 km cloud top altitude and 3.8 km aerosol scale height are the averaged cloud
top parameters at low latitudes (Table 2.2).

(a)

(b)

(c)

(d)

(e)
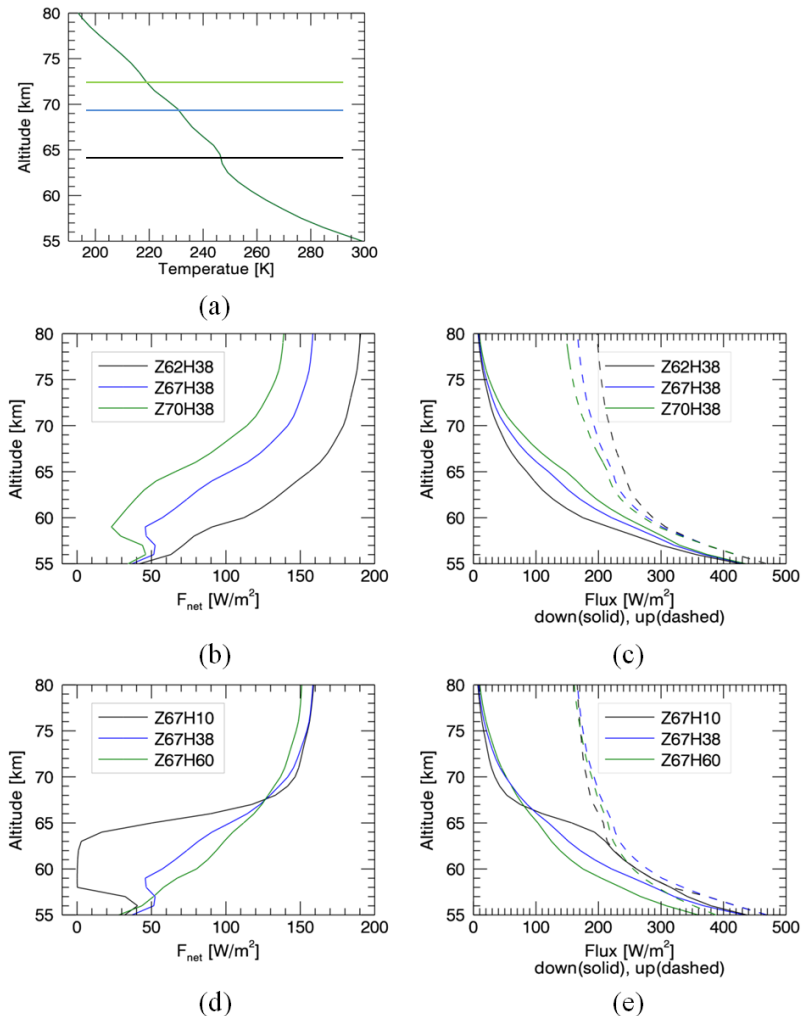
Figure 4.7: Integrated flux profiles in the low latitude. (a) Temperature profile and three cloud top altitudes are marked. (b) Net flux profiles, and (c) upward and downward flux profiles are calculated for three cloud top altitudes: 62 km (black), 67 km (blue), and 70 km (green), with a fixed 3.8 km aerosol scale height. (d) and (e) are net flux profiles, and upward and downward flux profiles, respectively, calculated for three aerosol scale height: 1.0 km (black), 3.8 km (blue), and 6.0 km (green), with a fixed cloud top altitude as 67 km.

top temperature. The large aerosol scale height corresponds to a blurred cloud top boundary and the differences in spectral properties of sulfuric acid clouds have more pronounced effect on the outgoing radiation. For instance, at wavenumber < 200 cm^{-1} the brightness temperature increases since radiation originates in the deeper and hotter atmosphere. Figure 4.6(b) illustrates the general rule that the radiation escapes to space from a level with $\tau \sim 1$ which altitude depends on wavenumber.

Figure 4.7 shows the result of full wavenumber-integrated flux profiles. Figure 4.7(a) is the temperature profile which used for the calculation. This calculation used the same set of cloud parameters as in Fig. 4.6. Figure 4.7(b) shows increasing net flux at 80 km altitude from ~140 W/m^2 to ~190 W/m^2 during the cloud top altitude changes from 70 km to 62 km. It is related with the increased upward fluxes at 80 km (Fig. 4.7(c)) due to the warmer cloud top temperature, while the downward fluxes are similar at the same level. The decreasing downward fluxes with altitude in Fig. 4.7(c) correspond to the exponential shape of upper cloud layer (Sect. 2.2.4.1).

Figure 4.7(d) and (e) present the result of three aerosol scale heights. As aerosol scale height gets smaller, the boundary of cloud top becomes sharper. The net flux profile of 6 km aerosol scale height increases smoothly with altitude, but that of 1 km aerosol scale height shows noticeable slope changes in the downward flux near to the cloud top altitude. This result implies that the aerosol scale height plays an important role for controlling downward flux and affects net flux profile within the upper cloud layer, even though there are no significant differences in the outgoing net fluxes at 80 km altitude.

4.1.2.2   Cold collar

The thermal structure of the cold collar is one of peculiar features in the Venus lower atmosphere. It has around 10 km thickness temperature inversion layer in the 60–70 km altitude range (Fig 3.1). The temperature inversion layer produces a spectral inversion in the "shoulders" of strong CO_2 absorption bands, as shown in the spectrometer observation data (Fig. 2.11). Figure 4.8 presents synthetic brightness temperature spectra, which are calculated for the four cloud top altitudes with a fixed aerosol scale height of 2.1 km. Four cloud top altitudes are selected: 65 km altitude is the averaged parameter at the cold collar region, 63 km is the temperature minimum level in the inversion layer, 61 km is possible lowest altitude for the cloud top in this study, and 70 km is the level of temperature maximum within the temperature inversions layer. The spectra corresponding to 61 km, 63 km, and 65 km cloud top altitudes show the spectral inversion obviously at the shoulders of 2349 cm^{-1} (4.3 μm) CO_2 band. The spectrum calculated for 70 km cloud top altitude does not show a spectral inversion near the 2349 cm^{-1} band, because in this case the temperature inversion is hidden within the cloud. However, the spectral inversions at the shoulder of the 667 cm^{-1} (15 μm) CO_2 band can be found clearly for all of spectra. Lower cloud opacity in this wavenumber range is not enough to block the thermal emission from the temperature inversion region, even for the 70 km cloud top altitude case. The brightness temperature of 61 km and 63 km cloud top altitudes show more than 240 K in less than 500 cm^{-1} and around 1500 cm^{-1} wavenumber. 240 K is corresponding to 60 km altitude, and higher than 240 K brightness temperature implies that these thermal emissions are originated from the middle cloud layer.

Figure 4.8(b) shows the spectra calculated for three aerosol scale heights. The spec-
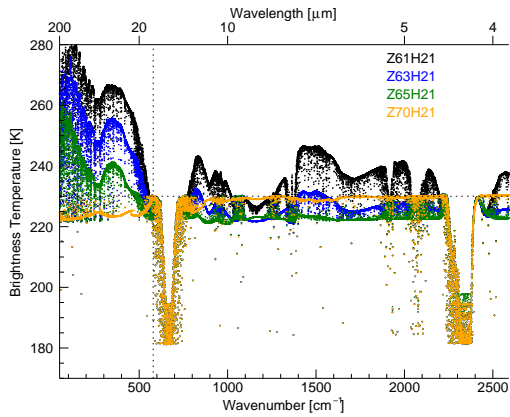
(a)
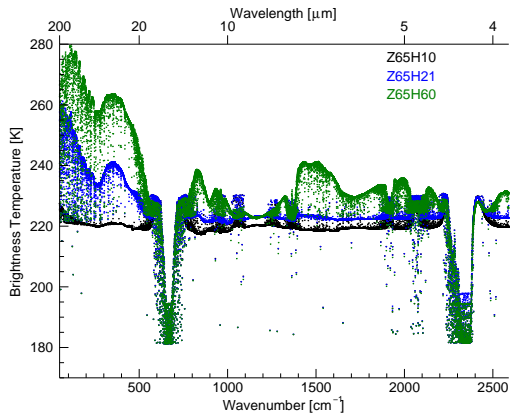
(b)

Figure 4.8: Brightness temperature spectra are calculated for the cold collar thermal structure with various cloud top parameters. Descriptions are the same as Fig. 4.6. (a) Four cloud top altitudes are compared: 61 km (black), 63 km (blue), 65 km (green), and 70 km (orange) with the fixed aerosol scale height as 2.1 km. (b) Three aerosol scale heights are compared: 1.0 km (black), 2.1 km (blue), and 6.0 km (green) with the fixed cloud top altitude as 65 km. 65 km cloud top altitude and 2.1 km aerosol scale height are the averaged cloud top parameters at the cold collar regions (Table 2.2).

(a)

(b)

(c)

(d)

(e)
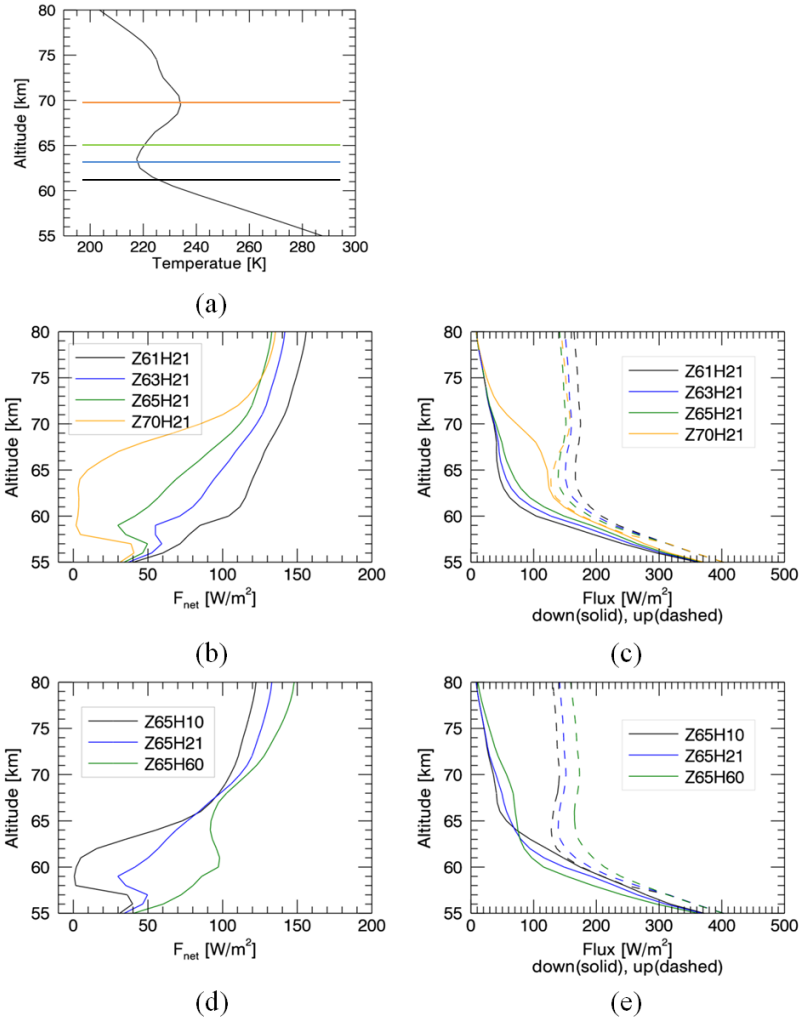
Figure 4.9: Integrated flux profiles at the cold collar. (a) Temperature profile, and four cloud top altitudes are marked. (b) Net flux profiles, and (c) upward and downward flux profiles are calculated for each cloud top altitude: 61 km (black), 63 km (blue), 65 km (green), and 70 km (orange), with the fixed 2.1 km aerosol scale height. (d) and (e) are net flux profiles, and upward and downward flux profiles, respectively, calculated for three aerosol scale height: 1.0 km (black), 2.1 km (blue), and 6.0 km (green), with the fixed cloud top altitude as 65 km.

trum from large aerosol scale height (~6 km) in Fig. 4.8(b) has a similarity with that from low cloud top altitude (61 km) in Fig. 4.8(a). It implies that this large aerosol scale height does not have enough opacity, even with the 65 km cloud top altitude. However, the thermal emission at wavenumber < 500 cm^{-1} is weak (see, Appendix C) and cannot produce significant flux increase. Figure 4.8(b) shows that spectrum decreases and converges to the cloud top temperature (~220 K) as the aerosol scale height reduces from 6 km to 1 km. This figure, as earlier Fig. 4.6(b), again illustrates the rule that the brightness temperature of the outgoing radiation is roughly defined by the atmospheric temperature at the $\tau \sim 1$ level which altitude depends on wavenumber.

Figure 4.9 shows vertical profiles of the integrated fluxes. Descriptions are the same as Fig. 4.7. The net flux at 80 km altitude increases from 130 W/m^2 to 160 W/m^2 for the cloud top altitude change from 65 km to 61 km in Fig. 4.9(a). The flux dependence on the aerosol scale height at the cold collar is quite different from that at the low latitudes. The aerosol scale height changes the slope of net flux profile at the cloud top, as well as the net flux at 80 km altitude from ~120 W/m^2 for the 1 km aerosol scale height to ~150 W/m^2 for the 6 km aerosol scale height. This energy gain amount (~30 W/m^2) due to the aerosol scale heights is comparable to that due to the cloud top altitudes. The shape of net flux profile is sensitive to both cloud top parameters in Fig. 4.9(c) and (e). This implies that both cloud top parameters strongly affect thermal flux, when there is a temperature inversion layer near at the cloud top.

4.1.2.3   Polar region

Typical polar region temperature profile is characterized by a quasi-isothermal layer of 10–15 km thickness above the tropopause. The temperature at 70–75 km altitudes is around 10 K higher than that at the low latitudes. This results in no more than 5 K differences in the cloud top temperature when its altitude changes from 61 km to 70 km. Figure 4.10(a) shows the spectra calculated for the cloud top at 61 km, 63 km, and 70 km and the aerosol scale height of 1.7 km. 61 km and 70 km cloud top altitudes are selected to keep the continuity for the sensitivity to the cloud top altitude, as the lowest and the highest levels, respectively, which are done for the low latitudes and the cold collar, even though there are no significant temperature differences at the cloud tops. Figure 4.10(b) shows the outgoing spectra calculated for three aerosol scale heights: 1.0 km, 1.7 km, and 6.0 km with fixed cloud top altitude at 63 km. As same as the cloud top, 1.0 km and 6.0 km aerosol scale heights are selected for the continuity values as done for the low latitudes and the cold collar. Common feature in Fig. 4.10 is that all spectra are concentrated to the cloud top temperature (~240 K). It is obvious due to similar temperatures of all cloud top altitudes, even though there is almost 10 km difference of the cloud top altitudes. This indicates that the outgoing spectrum is not sensitive to the cloud top altitude in the polar region. Figure 4.10(b) represents the similar pattern as Fig. 4.10(a) does, convergence to the cloud top temperature and increasing brightness temperature at wavenumber $<$ 500 cm^{-1}.

Figure 4.11 shows temperature profile, net flux profile, and upward and downward flux profiles similar to Fig. 4.7 and Fig. 4.9. The comparison between Fig. 4.11(c) and (e) gives an interesting point: there is only negligible changes for upward fluxes ($<$10 W/m^2) in upward fluxes for all cloud top altitudes. The reason is related to the isothermal temper-
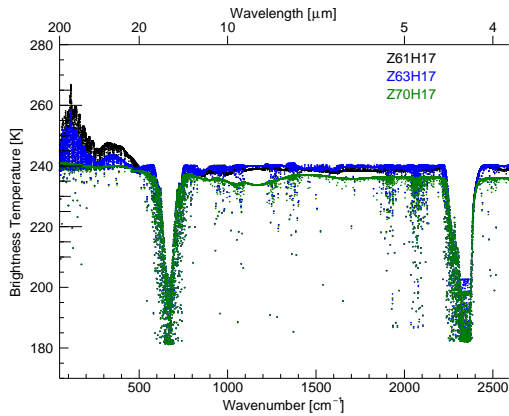
(a)
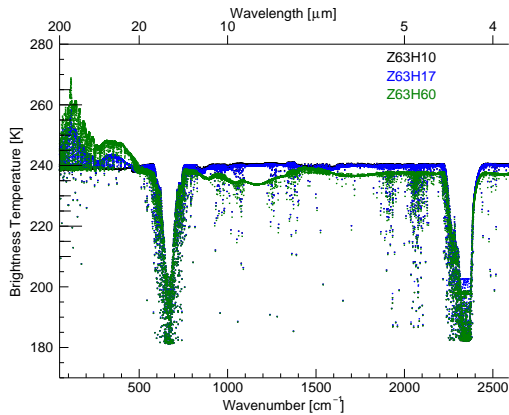
(b)

Figure 4.10: Brightness temperature spectra are calculated for the polar thermal structure with various cloud top parameters. Descriptions are the same as Fig. 4.6. (a) Three cloud top altitudes are compared: 61 km (black), 63 km (blue), and 70 km (green) with the fixed aerosol scale height as 1.7 km. (b) Three aerosol scale heights are compared: 1.0 km (black), 1.7 km (blue), and 6.0 km (green) with the fixed cloud top altitude as 63 km. 63 km cloud top altitude and 1.7 km aerosol scale height are the averaged cloud top parameters at the cold collar regions (Table 2.2).

(a)

(b)

(c)

(d)

(e)
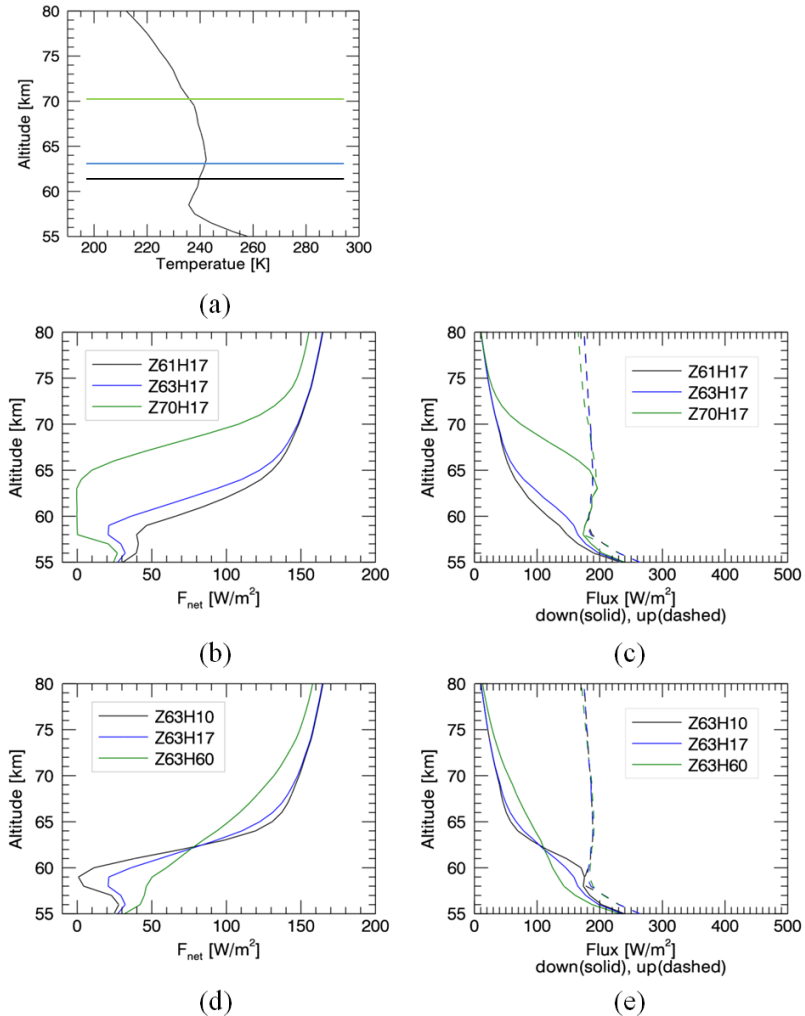
Figure 4.11: Integrated flux profiles in the polar region. (a) Temperature profile, and three cloud top altitudes are marked. (b) Net flux profiles, and (c) upward and downward flux profiles are calculated for three cloud top altitudes: 61 km (black), 63 km (blue), and 70 km (green), with the fixed 1.7 km aerosol scale height. (d) and (e) are net flux profiles, and upward and downward flux profiles, respectively, calculated for three aerosol scale height: 1.0 km (black), 1.7 km (blue), and 6.0 km (green), with the fixed cloud top altitude as 63 km.

ature structure at the cloud tops. Downward fluxes increase as cloud top altitude moves upward, while upward fluxes are almost constant in Fig. 4.11(c). The same trend is shown in Fig. 4.11(e), which shows almost constant for the upward fluxes while the aerosol scale height changes. This results in that net flux increases as the cloud top goes lower, even though the upward fluxes are nearly same for all cases.

4.1.3 Cooling rate in the mesosphere

Radiative energy loss results in cooling of atmosphere that affects the thermal structure of the atmosphere. In this chapter, we first introduce the cooling rate calculation. Then we will investigate sensitivity of cooling rate to the cloud top structure. Each parameter of the upper cloud structures shows different effects on the cooling rate depending on the temperature structure.

4.1.3.1 Cooling rate

Spectral integrated net flux profile contains information about energy deposition in each layer of the atmosphere. The radiative energy sources and sinks within a volume can be derived by the divergence of net flux (Goody and Yung 1989). In a stratified atmosphere, the divergence of net flux has only vertical axis and the cooling rate is expressed as follow:

$$
\begin{aligned}
\frac{dT}{dt} &= \frac{1}{\rho c_p}(\nabla \cdot F_{\text{net}}) \\
&= \frac{1}{\rho c_p}\left(\frac{dF_{\text{net}}}{dz}\right),
\end{aligned}
\tag{4.1}
$$

where dT/dt is the cooling rate in [K/Earth day], ρ is the density, and c_p is the heat capacity at constant pressure. Since net flux has one vertical dimension, the divergence of the net flux ($\nabla \cdot F_{\text{net}}$) can be expressed into (dF_{net}/dz). Although the atmosphere usually cools down in the thermal IR range, we note that thermal heating is also possible. Whether the atmosphere is heated or cooled by radiative energy exchange is defined by the sign of net flux derivative in Eq. 4.1, as the earlier studies of the Venus atmosphere calculated cooling rates (Rodgers and Walshaw 1966, Schofield and Taylor 1982, Revercomb et al. 1985, Haus and Goering 1990, Crisp 1989, Crisp and Titov 1997).

The specific heat at constant pressure (c_p, [J/(kg·K)]) as a function of temperature is taken from Crisp (1986):

$$
c_p(T) = 443.15 + 1.688T - 1.269 \times 10^{-3}T^2 + 3.47 \times 10^{-7}T^3.
\tag{4.2}
$$

This equation is a least-square fit to laboratory measurement of c_p, and neglects pressure dependence that provides <0.5% error in the 200–590 K temperature range, and <1% error at 170–200 K (Crisp 1986).

Density is derived from the ideal gas law

$$
\rho(z) = \frac{p(z)}{RT(z)},
\tag{4.3}
$$

where p is the pressure in [bar], T is the temperature in [K], and R is the universal gas constant which is 191.4 J/(kg·K) for the Venus atmosphere with the mean molecular weight

(a)

(b)

(c)

(d)

(e)

(f)
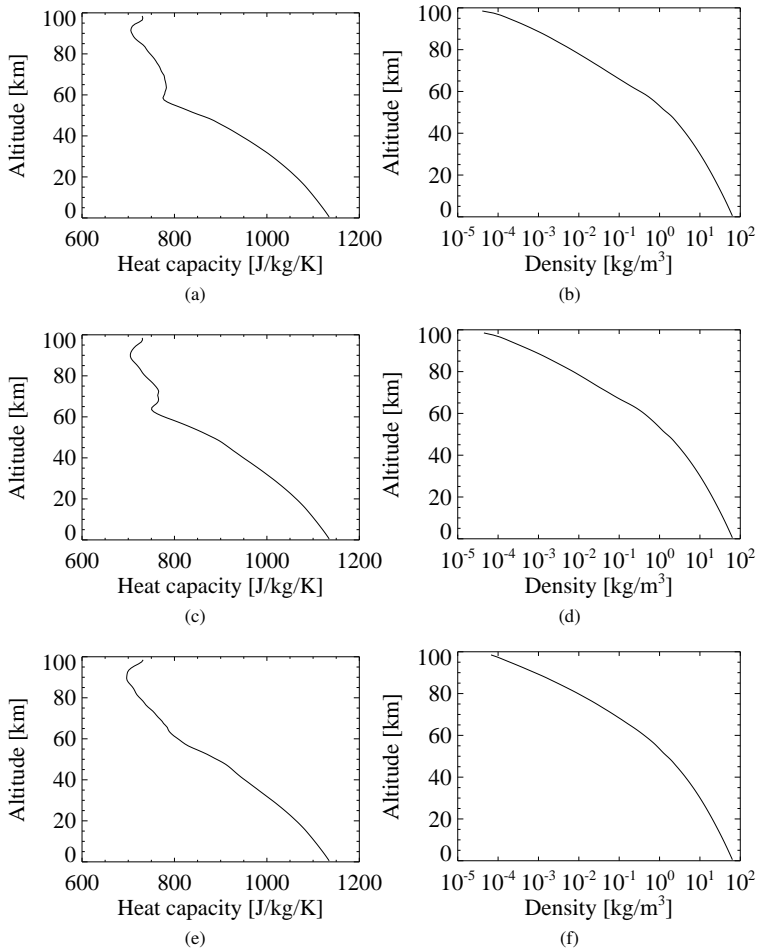
Figure 4.12: Heat capacity profiles from Eq. 4.2 and density profiles from Eq. 4.3. (a) and (b) are derived from polar temperature and pressure profiles, and likewise, (c) and (d) are from the cold collar, and (e) and (f) are from low latitude.

(a)   (b)
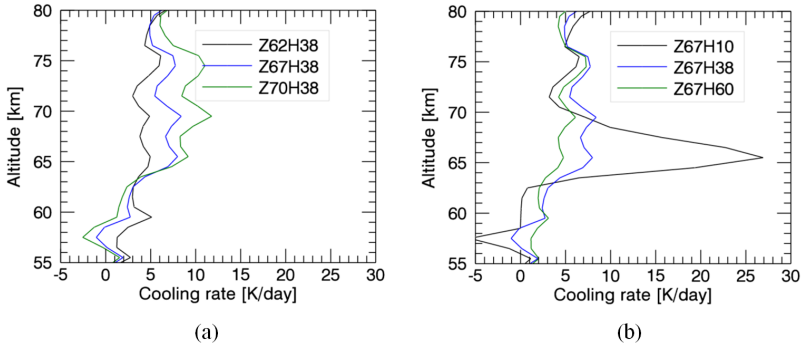
Figure 4.13: Cooling rate profiles are calculated for the low latitudes. (a) Three cloud top altitudes are compared: 62 km (black, *Z62H38*), 67 km (blue, *Z67H38*), and 70 km (green, *Z70H38*), with the 3.8 km-fixed aerosol scale height. (b) Three aerosol scale heights are compared: 1.0 km (black, *Z67H10*), 3.8 km (blue, *Z67H38*), and 6.0 km (green, *Z67H60*), with the 67 km-fixed cloud top altitude. 67 km cloud top altitude and 3.8 km aerosol scale height are the averaged cloud top parameters at the low latitude region (Table 2.2).

of 43.44 that corresponds to the composition of 96.5% CO_2, 3.5% N_2, 180 ppm SO_2, 60 ppm Ar, and 30 ppm CO (Seiff et al. 1985).

Heat capacity vertical profiles are shown in Fig. 4.12(a), (c), and (e). These figures show that heat capacity follows the temperature profile as shown in Fig. 3.1. Figure 4.12(b), (d), and (f) show density profiles.

4.1.3.2 Sensitivity of the cooling rate to the cloud top structure

Cooling rates are derived from the net flux profiles which have been derived in Sect. 4.1.2 and Eq. 4.1. Since the net flux profile significantly depends on both cloud top parameters and thermal structure, the cooling rate profiles are compared for the same atmospheric models as used in Sect. 4.1.2. Figure 4.13 shows the results for the low latitude case for three cloud top altitudes (Fig.(Cooling rate-low lat)a) and three aerosol scale heights (Fig. 4.13(b)). The calculations show cooling rate peaks at around 65 km, 70 km, and 75 km in the figure. The comparison of cooling rate profiles calculated for observed temperature profile to temperature structure with constant lapse rate shows that the peaks are caused peculiarities of temperature, like minor changes in lapse rate (see, Appendix D for more details). Moving of the cloud top from 62 km to 70 km altitude results in increasing of the cooling rate at the cloud tops from 3.0 K/day to 12 K/day (Fig. 4.13(a)).

A remarkable change is shown in Fig. 4.13(b). Decreasing of the aerosol scale height from 6.0 km to 1.0 km results in increasing of the cooling rate from 4.5 K/day to 27 K/day at the 65–68 km altitude range with a pronounced peak at the cloud top for $H = 1.0$ km. This comparison implies that small aerosol scale height is the condition for strong radiative cooling at the cloud top. Figure 4.13(a) shows the change of cooling rate profiles with cloud top altitudes. Cooling rate profiles in the 65–75 km altitude range, where the
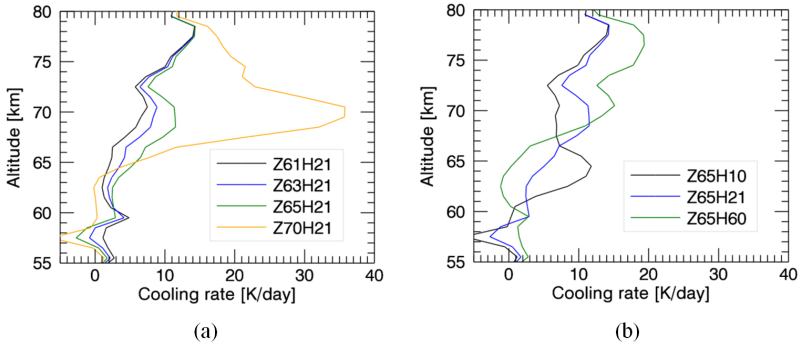
Figure 4.14: Cooling rate profiles are calculated for the cold collar condition. (a) compares four cloud top altitudes: 61 km (black, *Z61H21*), 63 km (blue, *Z63H21*), 65 km (green, *Z65H21*), and 70 km (orange, *Z70H21*) with the 2.1 km-fixed aerosol scale height. (b) compares three aerosol scale heights: 1.0 km (black, *Z65H10*), 2.1 km (blue, *Z65H21*), and 6.0 km (green, *Z65H60*) with the 65 km-fixed cloud top altitude. 65 km cloud top altitude and 2.1 km aerosol scale height are the averaged parameters at the cold collar region (Table 2.2).

cloud top is located, increase from 3–6 K/day for the 62 km cloud top altitude (*Z62H38*) to 8–12 K/day for the 70 km cloud top altitude (*Z70H38*). Thermal heating can be seen at the base of upper cloud layer (57–58 km altitude) caused by high opacity of the upper cloud layer due to either high cloud top altitude or small aerosol scale height.

Figure 4.14 shows the results for the cold collar case. Sub-plot (a) illustrates dependence of the cooling rate on the cloud top altitude. Four cloud top altitudes are selected for the comparison (see, Sect. 4.1.2.2). The cooling rates near the cloud tops increase from 1.3 K/day to 6.5 K/day during the cloud top moves from 61 km to 65 km. There is a strong cooling rate peak (36 K/day) for the 70 km cloud top altitude, and is caused by ~10–15 K warmer cloud top temperature (233 K) than others in the inversion layer (218–224 K). Less heat capacity and density at this high altitude also contribute for this extreme cooling rate. Figure 4.14(b) compares the cooling rate for three aerosol scale heights. In the 63–66 km altitude range, the cooling rate near the cloud top increases from 1.7 K/day to 12 K/day with decreasing aerosol scale height from 6.0 km to 1.0 km. The small aerosol scale height, 1.0 km (*Z65H10*), brings a strong cooling rate peak at the cloud top comparing to larger aerosol scale height. The large aerosol scale height cannot produce enough thermal opacity to block upward emission, and induces enhanced mesospheric cooling rate above 70 km altitude.

Another interesting thing is that thermal emission generates radiative cooling effects (~11 K/day) at 70 km, where is the temperature maximum of the inversion layer, for the averaged cloud top parameters (*Z65H21*). This implies that thermal emission of the averaged cloud condition can remove the temperature peak at the inversion layer. Particular cases were retrieved from the observation also, which have $H \leq 1.0$ km and $Z \sim 63$ km at the cold collar (*Z63H10*), as shown in Fig. 2.26. Figure 4.15 compares these two cases
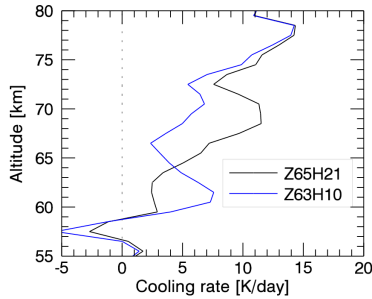
Figure 4.15: Cooling rate profiles are calculated for the averaged cloud top parameter (black solid line), $Z = 65$ km and $H = 2.1$ km (Table 2.2, *Z65H21*), and the particular case (blue solid line), $Z = 63$ km and $H = 1.0$ km (Sect. 2.2.4.2, *Z63H10*), at the cold collar.

(*Z65H21* and *Z63H10*), and shows the particular case can deepen the inversion layer even more by 6–7 K/day cooling at 60–63 km and reduced cooling (6.8 K/day) at 70 km. Since the solar heating can be significant at the cloud tops, it requires further study to evaluate net radiative effects of clouds at the cold collar.

Figure 4.16(a) shows the cooling rate profiles depending on the cloud top altitude for the polar region. The cooling rates at the cloud top altitudes increase from 7.3 K/day to 38 K/day during cloud top altitude increases from 61 km altitude ($T_{\text{cloudtop}} = 239$ K) to 70 km ($T_{\text{cloudtop}} = 235$ K). Although the net flux convergence is similar for each cloud top, low density at high altitudes results in a significant cooling rate peak for $Z = 70$ km. The small aerosol scale height of 1.7 km induces the pronounced peak of cooling rate at the cloud top (11 K/day), and it becomes even sharper for the 1.0 km aerosol scale height (16 K/day) (Fig. 4.16(b)). Large scale height of 6.0 km (*Z63H60*) smoothes the cooling rate peaks (~6 K/day) at the cloud top. This result emphasizes that small aerosol scale height results in effective cooling at the cloud tops.

Summary

The outgoing thermal emission is calculated based on the atmospheric temperature, gases, and cloud model described in Chapter 3. We calculated different opacity and temperature conditions, which are described in Table 4.1, and compared the radiative effects of each opacity agent on the thermal fluxes and spectral features. Thermal fluxes integrated over the narrow (10 cm^{-1}) range (Sect. 4.1.1.2), and the important results are the following: (1) the clouds are very effective in blocking thermal emission from deep atmosphere, (2) CO_2 strongly affects the thermal emission even above the cloud tops due to strong bands. Optical properties of agents are wavenumber dependent, therefore integrated fluxes over the sub-intervals reveal different radiative responses to each opacity agent. L2–3 sub-interval emits most of outgoing thermal flux, and L2–4 is sensitive to the clouds opacity.

We calculate the sensitivity of thermal emissions to the cloud tops for three typical temperature profiles: low latitude, the cold collar, and polar regions (Sect. 4.1.2). Both brightness temperature spectrum and vertical profiles of thermal IR fluxes show depen-
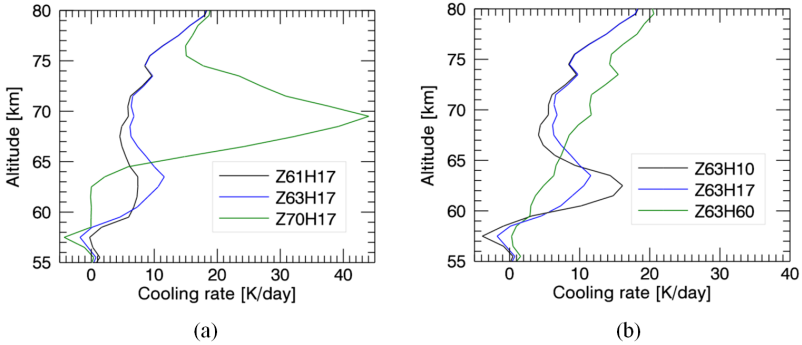
Figure 4.16: Cooling rate profiles are calculated for the polar condition. (a) compares three cloud top altitudes: 61 km (black, *Z61H17*), 63 km (blue, *Z63H17*), and 70 km (green, *Z70H17*) with the 1.7 km-fixed aerosol scale height. (b) compares three aerosol scale heights: 1.0 km (black, *Z63H10*), 1.7 km (blue, *Z63H17*), and 6.0 km (green, *Z63H60*) with the 63 km-fixed cloud top altitude. 63 km cloud top altitude and 1.7 km aerosol scale height are the averaged parameters in the polar region (Table 2.2).

dencies on the cloud top parameters. We compared the cloud top altitude and the aerosol scale height, and found the cloud top altitude is an important source to change the outgoing fluxes (up to 50 W/m^2), while the aerosol scale height changes the cooling rate at the cloud tops (up to 20 K/day) for the low latitude temperature profile. At the cold collar, both of cloud top parameters can change the outgoing fluxes (up to 30 W/m^2) and affect the cooling rate at the cloud tops. Polar region has the least sensitivity of thermal fluxes to the cloud top altitude changes (<10 W/m^2) due to the quasi-isothermal structure near the cloud tops during the smaller aerosol scale height strengthen the cooling rate at the cloud tops. The result shows that the cloud top parameters affect the outgoing flux and cooling rate, and the sensitivity of the thermal flux to the cloud top parameters is strongly affected by the temperature profiles.

4.2   Meridional trends of thermal emission in the Venus middle atmosphere

Thermal fluxes in the atmosphere depend on the temperature structure, gases composition, and aerosols opacities. Temperature profiles at the cloud top levels (60–70 km) has a strong latitude dependence and Venus Express observation suggest that the upper cloud structure also shows latitudinal trend. From equator to pole, the cloud top altitude decreases from ~68 km to ~62 km, while the aerosol scale heights decreases from ~4 km to less than 1–2 km (Chapter 2). The latitudinal changes of the temperature and cloud structure results in meridional trends of thermal emission. In this chapter, we present the results of thermal fluxes calculations as a function of latitudes, based on the temperature field from radio science experiment VeRa/Venus Express and VIRA model (Chapter 3),

observed upper cloud structure (Lee et al. 2012) (Fig. 2.22)), and gases and aerosol extinction data base (Chapter 3).

Table 4.3 shows the outgoing thermal fluxes from the top of the atmosphere (this study, it is 99 km altitude) over the latitudes. The peculiarity of the Venus atmosphere is the latitudinal pattern of the outgoing flux. The maxima are in the 80°–90°S and 0°–10°S bins (> 154 W/m^2), and the minimum is in the 60°–70°S bin (135 W/m^2), and this is quite different with the Earth atmosphere which shows a decreasing trend with latitude (Fig. 1.8). This result is comparable with VIRA, which shows the same trend (Table 4.3). The sensitivity of thermal flux to the cloud top altitude showed (Sect. 4.1.2) that the influence of cloud top altitude is a dominant factor to determine outgoing net flux at low latitudes and decreases toward the pole. Meanwhile, the temperature of cloud top is around 243 K in the polar region, which is even higher than that at low latitudes (238 K). It results in the maxima of outgoing flux at the equator and the pole. The cloud top temperature at the cold collar is almost 20 K colder than those in other regions and produces the minimum outgoing thermal flux, even though the averaged cloud top parameters are intermediate values between those at the pole and at the equator. This circumstance implies that the latitudinal distribution of outgoing net thermal emission depends on the temperatures of

Table 4.3: Outgoing thermal flux [W/m^2] from the equator to the pole. First column is the latitudinal bins of this study, and the second and the third columns are the results of this study. The fourth and the fifth columns are the values in VIRA (Moroz et al. 1985). Average over 10° latitude of this result is shown for the comparison with VIRA data, which has 10° latitudinal bin size.

Latitude(°)	This study		VIRA	
	Outgoing Net flux	10°-bin average	VIRA (zonal avg)	Night(18–06 h) average
0–5	151	154	161	161
5–10	157			
10–15	149	151	161	162
15–20	153			
20–25	144	146	161	162
25–30	148			
30–35	148	146	160	162
35–40	144			
40–46	147	148	158	158
46–50	149			
50–56	137	137	149	145
56–60	136			
60–65	136	135	137	136
65–70	133			
70–75	144	143	148	152
75–80	141			
80–85	157	164	161	161
85–90	171			
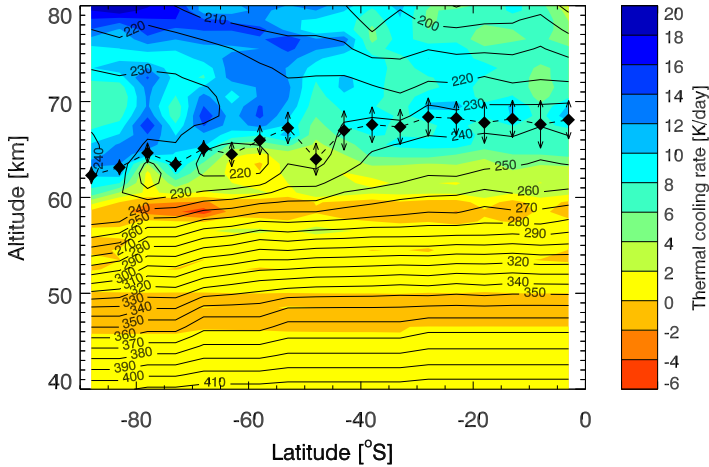
Figure 4.17: Cooling rate vertical profiles (40–80 km) with latitude. The cloud top altitudes are in black filled diamonds, and the aerosol scale heights are in vertical arrows (Chapter 2). Observed temperature is shown in black contours (Chapter 3).

cloud top strongly.

Altitude-latitude field of cooling rate is shown in Fig. 4.17. The radiative effect of clouds in the thermal IR range is two-fold. Firstly, the cloud produce strong cooling peak at the cloud tops. Secondly, they can cause heating near the cloud base due to the absorption of thermal emission below clouds. These two radiative effects of clouds can be found clearly in Fig. 4.17. Significant cooling rates (>5 K/day) are derived at the cloud top and above it. The mesospheric thermal cooling is produced by CO_2 emission. A steady heating rate (<−1 K/day) was found at the cloud base (47–48 km) at all latitudes.

Figure 4.17 shows the second region of thermal heating at 57–60 km, in the transition layer between the upper and middle cloud layers (Sect. 3.1.2). The sharp boundary of the upper cloud base absorbs upward flux strongly at this level and results in the thermal heating (~1 K/day) at all latitudes. This thermal heating at the transition layer shows strong value (~5 K/day) in the 65–70°S bin (Fig. 4.18(b)). It is caused by combined effects of enhanced upper cloud layer opacity and increased upward flux compared to both beside bins.

Figure 4.18 compares selected cooling rate profiles from Fig. 4.17 for the three typical latitudinal thermal structures. Since the middle and lower cloud layers has latitude independent structure in this study, Fig. 4.18 show the similar cooling rates below 60 km
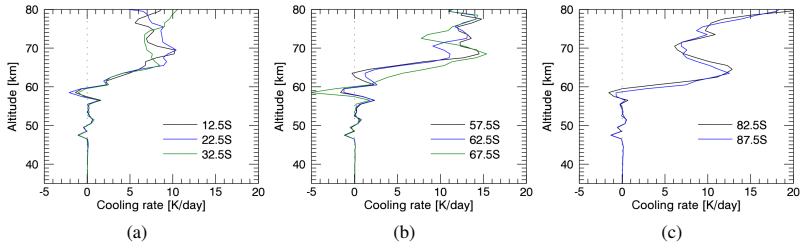
Figure 4.18: Selected profiles from Fig. 4.17 are compared. (a) Three profiles from the low latitudes, (b) three profiles from the cold collar, and (c) two profiles from the polar region are shown.

from (a) to (c). The cooling rates at the cloud tops are significant ($\sim$10 K/day) in the polar region (Fig. 4.18(c)), compared to these in low latitudes and the cold collar regions ($\sim$5–8 K/day), due to small aerosol scale height. Figure 4.18 shows the cooling rates at above 70 km, caused by CO_2 emission, are 5–10 W/m^2 at low latitudes, which are less than that at the high latitudes ($>$ 10 W/m^2). The warmer temperature over the high latitudes at this level results in this cooling rate gradient with latitude. Below the cloud deck, cooling rates are nearly zero, even though net flux divergence $\sim$4 W/m^2/km, due to large heat capacity and density in the deep atmosphere.

Summary

The cooling rate profiles are calculated based on the observed thermal structure and cloud top parameters from Venus Express (Chapter 2). The meridional trend of cooling rate can be divided into three vertical regions. First, within the cloud deck, cooling rates at the cloud tops increase from 5–8 K/day at low-middle latitudes to $\sim$10 K/day at the pole. There are thermal heatings ($\sim$1 K/day) at the bases of the lower and upper cloud layers at all latitudes. Second, below cloud layers, very large thermal opacity of atmospheric gases results in almost zero net flux. Heat inertia (the multiplication of heat capacity and density) in the deep atmosphere is also too large to generate radiative forcing from small net flux divergence. Third, CO_2 emission is the major factor of the mesospheric cooling above clouds.

The meridional trends of the outgoing net flux shows the maxima at the equator and the pole (154 and 164 W/m^2, respectively) and decreases to the cold collar region (135 W/m^2). It is a significant difference of the Venus atmosphere compared to that of the Earth atmosphere, which has a decreasing trend of outgoing flux with latitude.

5 Discussion and conclusions

5.1 Radiative energy balance in the Venus clouds and mesosphere

The thermal fluxes in the Venus lower atmosphere are calculated in Chapter 4. The simulations are based on the temperatures derived from the radio-occultation experiment VeRa onboard Venus Express. The cloud top structure is retrieved from the joint analysis of VeRa soundings and thermal IR spectroscopy by VIRTIS (Chapter 2) (Lee et al. 2012). The calculations show that the structure of the upper cloud determines radiative cooling effects to a large extent (Chapter 4). Also, the unknown UV absorber in the upper cloud layer deposits almost half of the incoming solar energy (Chapter 1). Therefore, the upper cloud layer plays an important role for the radiative balance in the mesosphere. In this chapter, we show the radiative energy balance, which compares the thermal cooling rate from Chapter 4 with the solar heating rate from Tomasko et al. (1985) in the 55-85 km altitude range. Then we discuss the relation with the opacity variations of the middle and lower clouds, atmospheric dynamics, and climates. We end with a comparison of the radiative forcing by the Venus clouds and atmospheric gases with that in other planetary atmospheres.

5.1.1 Comparison with the heating rate in the cloud layers and mesosphere

The solar flux radiometer (LSFR) onboard Pioneer Venus measured the broad band flux of sunlight. Tomasko et al. (1980, 1985) used this flux profile to derive a cloud structure that fits the observations. Unity optical depth of their cloud model is around 28 mbar ($\sim$71 km altitude) at 0.63 μm wavelength. Four modes are used for cloud size distributions, and the UV absorbing region is at the 28–75 mbar pressure level ($\sim$65–71km altitude). Tomasko et al. (1985) calculated the zonal average of the heating rate with this cloud model from 0.18 μm to 4.6 μm. They adopted a model for polar clouds (70–90°) at less than 40 mbar pressure from Kawabata et al. (1980). This polar cloud model has the cloud tops at $\sim$67–68 km altitude.

Since the calculation of the solar heating rates is beyond the scope of this thesis, we compare the thermal cooling rate from this study (Chapter 4) to the solar heating rate from Tomasko et al. (1985) to evaluate the radiative energy balance. The solar heating rate calculation used 11 levels in the 55–85 km altitude range, 10° bins for latitudes smaller than 70°, and 4° latitude bins in the polar region. Although it has coarser vertical and
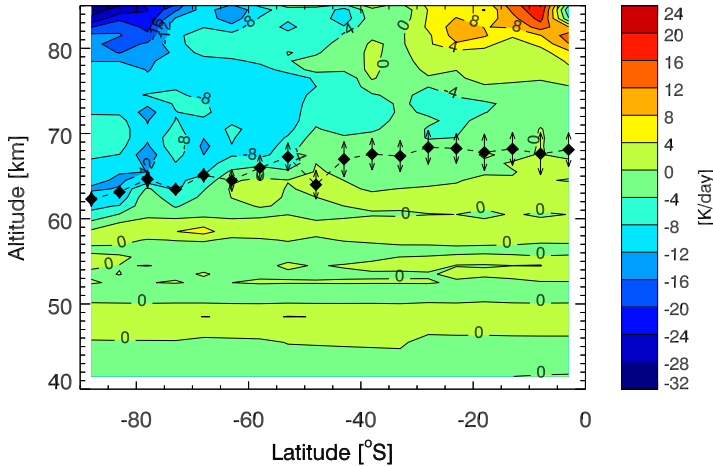
Figure 5.1: Net radiative heating rate (K/day) in the altitude-latitude field. The colors indicate the net radiative forcing. The thermal cooling rate is taken from Chapter 4, which is based on the observed thermal structure and cloud top parameters from Venus Express (Lee et al. 2012). The cloud top altitudes are shown as black filled diamonds with black dashed line, and the aerosol scale heights are shown in the vertical arrows. The solar heating rate is taken from Tomasko et al. (1985), and is based on the flux measurements of Pioneer Venus.

latitudinal grid resolution than our thermal cooling rate calculation, it provides a good approximation for the latitudinal distribution of the solar heating rate. Figure 5.1 shows the net radiative heating rate, which is the difference between the solar heating rate and the thermal cooling rate.

Figure 5.1 shows that the atmosphere is in radiative equilibrium within ~5 K/day below the cloud tops. A net heating is significant in the equatorial mesosphere above 75 km altitude. Solar heating and thermal cooling balance each other at middle latitudes (40°–50°). At higher latitudes, the entire mesosphere above the clouds shows a strong net cooling. The observed temperature at 70–80 km altitude over the polar region is ~10 K higher than at the equator. However, Fig. 5.1 suggests that the net radiative cooling should reduce the atmospheric temperature to the same levels. Moreover, it should break the isothermal profile at the pole and the temperature inversion at the cold collar. This implies the existence of an additional mechanism of transporting energy to maintain the observed temperature field. Mesospheric circulation, characterized by rising motion at

low latitudes, poleward flow, and subsidence at the high latitudes, has been suggested as a possible mechanism (Crisp 1989, Titov et al. 2007).

We note however that this comparison should be viewed with care, since the atmospheric models used to calculate the cooling and heating rates are different. Calculating solar heating rates for the same cloud model is a subject for future work.

5.1.2   Variation of lower and middle cloud layers of Venus

Recent Venus Express observations in the atmospheric "windows" reveal strong opacity variations in the middle and lower cloud layers. Figure 5.2 shows the emissions in the 2.3 μm "window". Spatial variation of the lower and middle cloud opacities produce the radiation contrasts seen in Fig. 5.2. The VIRTIS/Venus Express mosaic of the southern hemisphere (Fig. 5.2(a)) shows a factor of 5–7 decrease of the flux from the low and middle latitudes to the polar regions, which corresponds to the increasing of the cloud opacity due to either particle size and/or number density changes (Carlson et al. 1991, 1993, Cardesín Moinelo et al. 2008). The earlier NIMS/Galileo image (Fig. 5.2(b)) of the Venus equatorial region shows patchy morphology of the deep cloud. Two possible cloud particle properties over the poles have been proposed in the lower and middle clouds from observations. A comparison of observations in two spectral "windows" at 1.74 μm and 2.30 μm from VIRTIS/Venus Express and the Galileo near-IR spectrometer suggested larger mean radius particles or variations of H_2SO_4 concentrations in cloud aerosol particles (Carlson et al. 1993, Wilson et al. 2008). This anomalous cloud particle can result

(a)   (b)
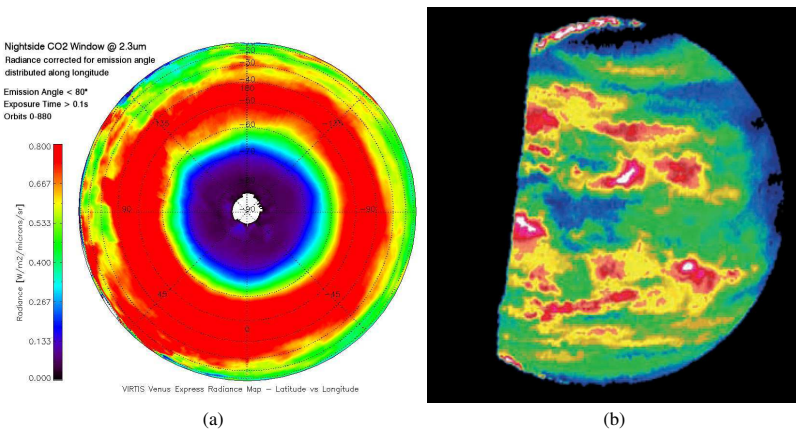
Figure 5.2: The thermal outgoing emission in the 2.3 μm "window" observed by VIRTIS/Venus Express (left) (from Cardesín Moinelo (2010)) and NIMS/ Galileo (right) (from Carlson et al. (1991)). False colors mark the variations of brightness produced by spatial inhomogeneity of the total cloud opacity. Red – high flux and low cloud opacity, blue – low flux and high cloud opacity.

in the change of the cloud opacities. Thermal emission leaking from below the clouds to space is weakened through absorption by the thick cloud layers, and has only a minor contribution to the global radiative energy balance. However, the radiative effects of the deep atmospheric thermal emission in the lower cloud layer could be much stronger. From a calculation of Crisp and Titov (1997) (Fig. 1.9), an increase or decrease of the opacity in the middle and lower clouds can change the thermal cooling rate by (-1.5)–$(+0.3)$ K/day, which are large amounts considering the huge thermal inertia in the deep atmosphere. For simplicity, this study uses a latitude independent opacity profile for the lower and middle cloud. This limits the realism of our simulation of radiative effects in the clouds. The inhomogeneous low and middle cloud morphology needs to be considered.

5.1.3   Implications for the dynamics of the Venus atmosphere

Figure 5.1 shows a strong net cooling (up to 32 K/day) above 70 km altitude poleward of ~60° latitude. It is caused by the reduced solar heating at high latitudes, which is not enough to compensate for thermal cooling from the cloud tops and mesospheric CO_2. Below ~30° latitude, solar heating exceeds thermal cooling above 75 km, where the net heating rate reaches ~18 K/day. A thermally direct circulation, Hadley-like circulation, which transports energy from equator to pole is required to compensate for the radiative energy unbalance condition. Crisp (1989) concluded that an upward velocity of 1.5 cm/s in the tropics and a downward flow of ~2.5 cm/s at high latitudes would be required to produce a net cooling/heating effect that compensates for the radiative disequilibrium and maintains the observed temperature field. This is a higher ascending velocity than that of the Earth Hadley cell in the tropics: ~0.3 cm/s for ~5 K/day heating (James 1994). However, there are uncertainties concerning the vertical profile of meridional winds and the latitudinal location of downwelling (Esposito et al. 2007). Also, it is not clear whether two or more Hadley cells are "stacked" above and below each other (Schubert et al. 2007).

The solar energy deposition in the cloud tops (60–70 km altitudes) are almost half of the total incoming solar flux. The solar heating rate is ~25 K/day at the subsolar point, 12.6 K/day for 60° degree solar zenith angle, and almost zero at the terminator near the cloud tops (Tomasko et al. 1985), which is nearly proportional to the cosine of the solar zenith angle. The differences of solar energy absorption along the solar local time (from the noon, through evening or morning terminators, to the night time) produce thermal tides. These atmospheric waves at the cloud tops propagate upward and downward (Gierasch et al. 1997). These atmospheric waves are evident in the temperature at isobaric level vs. local time from Venera and Vega missions (Zasova et al. 2007). The dissipation of thermal tides is one of the mechanisms which support the superrotation in the 60–90 km altitude range (Gierasch et al. 1997, Schubert et al. 2007).

5.1.4   Cloud effects on the climate evolution in the Venus atmosphere

Clouds play two opposite roles in the Venus climate: Firstly, they change the thermal opacity and generate thermal warming (greenhouse) effects. Although clouds are the second-most effective driver of the greenhouse effect after CO_2, they still have a huge thermal opacity. The thermal radiative forcing of clouds derived in this study is 219 W/m^2 for the low latitude condition (Table 4.2), which is seven times stronger than that of the

Earth clouds ($\sim$31 W/m^2) (Ramanathan et al. 1989). Secondly, clouds reduce the amount of solar energy absorption by reflecting incoming solar radiation: Venus is fully covered by thick clouds, and as a result, it has an albedo of $\sim$0.76. The combination of these two opposite radiative effects of clouds can be a trigger for a feedback mechanism that changes the climate. Bullock and Grinspoon (2001) investigated the clouds' effect on the Venus climate with a radiative-convective equilibrium model. They varied the abundance of SO_2 and H_2O which make up the Venus clouds. Decreasing SO_2 and H_2O suppresses cloud formation and results in thinner clouds. The reduced cloud albedo increases solar influx, and the less cloud opacity decreases thermal absorption by the clouds. The model results show that the deep atmosphere becomes hotter due to a reduction of the cloud albedo. The warmer atmosphere shifts the base of clouds upward, which leads to thinner clouds. This feedback can remove clouds entirely. The surface temperature rises up to $\sim$800 K when clouds are decreasing. The temperature of the surface becomes 725 K when there are no clouds at all, and it is caused by a lower IR gaseous opacity by reduced H_2O and SO_2, the absent of greenhouse effect by clouds, and relatively high albedo (0.4) due to Rayleigh scattering. Increasing H_2O and SO_2 enhances cloud opacities, and result in a higher albedo. The higher albedo can cool the surface temperature below 700 K. However, the higher H_2O abundance can generate strong greenhouse effects in the Venus atmosphere. When H_2O is increased to more than 50 time the current value, the surface temperature rises to $\sim$900 K by strong greenhouse effects. The high surface temperature erodes the base of clouds and leads to thinner and higher clouds. The radiative forcing of clouds on the Venus climate is a critical factor due to their huge opacity and high albedo.

5.2   Role of clouds and gases in the planetary atmosphere

The role of the atmosphere on the radiative forcing is different for each of the terrestrial planets in our solar system. Generally, there are two incoming energy sources: the absorbed flux from solar radiation and the heat flux from the interior of planet. Since the terrestrial planets have negligible internal heat flux, the incoming solar radiation is in balance with the outgoing thermal infrared flux. Therefore the effect of atmosphere on the radiative balance can become significant in the terrestrial planets through greenhouse effects and clouds, which reduce incoming solar radiation and affects outgoing flux. In the absence of an atmosphere, the surface temperature will be near the effective temperature (T_{eff}, Eq. 1.2). The internal heat flux of the gaseous giant planets is comparable to the incoming solar flux, and therefore has a strong effect on the atmospheric temperature (Sánchez-Lavega et al. 2004).

The atmosphere of Venus has an enormous greenhouse effects and the full cloud coverage over the globe. Mars and the Earth have only partial cloud coverage in much thinner atmospheres. The atmosphere of Mars is even thinner and colder than that of the Earth (5.6 mbar surface pressure and 210.1 K surface temperature (Kieffer et al. 1992), versus 1013 mbar and 288 K). Mars has water-ice clouds near $\sim$10 km altitude and CO_2-ice clouds near $\sim$50 km (de Pater and Lissauer 2001). However, the thin and cold atmosphere can only hold little amounts of water vapor, and this forms clouds in particular regions: in the vicinity of Olympus Mons and Tharsis, where orographic heating during the day makes the air rise up along the slope leading to cloud formation by condensation (Zurek

et al. 1992). Observations of clouds and theoretical calculations reveal that the radiative effects of condensate clouds are likely to be most important in the winter polar region (Zurek et al. 1992). In the lower atmosphere of Mars (<45 km), airborne dust generates strong radiative heating. This dust exceeds a few tenths of an optical depth, and absorbs both incoming solar radiation and thermal emission from the surface. This can reduce or even reverse the temperature lapse rate, producing a stably stratified atmosphere (Zurek et al. 1992). There are high spatial and temporal variations of airborne dust and it can be sustained in the atmosphere for long periods (Kahn et al. 1992). The radiative effects of suspended dust on the atmosphere are important. It alters the thermal structure and can encircle the whole globe during storms. However, the general dust distribution and the optical properties of the particles are not well known (Zurek et al. 1992, Kahn et al. 1992).

The Earth atmosphere maintains a mean surface temperature of ~15°C through greenhouse effects, mainly from H_2O, CO_2, and clouds (T_e is −18°C). The incoming solar radiation is 341 W/m^2 for the annual global mean. It is absorbed by the surface and atmosphere (161 W/m^2 and 78 W/m^2, respectively), as well as reflected by surface and atmosphere (102 W/m^2) (Trenberth et al. 2009). The radiative energy balance is sustained by the outgoing flux of 239 W/m^2. The actual surface emission is 396 W/m^2, but the outgoing radiation is trapped by atmospheric gases and clouds, and only 40 W/m^2 can escape to space directly (Trenberth et al. 2009). The major greenhouse agents in the Earth atmosphere are H_2O, which accounts for 75 W/m^2 of the total clear sky greenhouse effect, and CO_2, the second-most important greenhouse gas with 32 W/m^2 radiative forcing (Kiehl and Trenberth 1997). The clouds of the Earth have been studied through intensive observations. The cloud net radiative forcing (defined as the difference between all-sky condition and cloud-free condition) varies from −80 W/m^2 to +20 W/m^2 over the globe in the annual mean (Loeb and Wong 2007). It depends on the cloud amount, cloud water contents, cloud height, cloud droplet size, location, etc. The study of radiative effects of clouds on the Earth climate has a high priority in climate research (Loeb and Wong 2007), because clouds can change albedo and thereby affect absorption of solar and thermal radiation. For example, Ramanathan et al. (1989) showed that thermal radiative forcing of clouds is strongest in the tropics. Thick clouds in the deep convective regions over the tropic reach to high altitudes, and reduce outgoing emission by low cloud top temperature. However, the thick tropical clouds reflect solar radiation effectively, which results in a reduced solar influx. As a result, the net radiative forcing of clouds becomes close to zero in tropical region. The strongest net cooling effects are detected for low stratiform clouds over the west coast of America and Africa, and the southern oceans between 30°S and 60°S (Loeb and Wong 2007).

There is another interesting radiative forcing agent in the Earth atmosphere: the volcanic sulfuric acid aerosol. An increase of volcanic sulfuric acid aerosols can cause global mean temperature changes. After the large volcanic eruptions of El Chicon in 1982 and Pinatubo in 1991, volcanic gases formed sulfuric acid aerosols in the stratosphere. They covered the whole globe and stayed for several years. Observations showed stratospheric warming (~0.7–1.2°C) and tropospheric cooling (0.3–0.7°C) for the two-year global mean temperature (Hansen et al. 1996, Free and Angell 2002). However, several volcanic aerosol effects collude: warming of the tropical lower stratosphere, ozone depletion at high latitudes, tropical surface cooling, and mid-latitude surface warming. They are also associated with a strong polar vortex (Robock 2002). Quantifying the ra-

diative forcing of clouds and aerosols on climate is a difficult problem, because it can result in cooling and/or warming effects. The strong relation between clouds and atmospheric chemical/dynamical processes is another complexity, in addition to the change of albedo and amount of absorption.

The temperature of the atmosphere varies according to the energy sources and sinks at each level. One of the energy sources is the latent heat of cloud formation. The convective adjustment temperature decreases with altitude by the dry adiabatic lapse rate below the clouds, and by the wet adiabatic lapse rate above the clouds. The latter considers the latent heat released by condensation. The wet adiabatic lapse rate is lower than the dry adiabatic lapse rate in most planetary clouds (Sánchez-Lavega et al. 2004). However, the two can be equal in the Venus upper cloud layer, which means condensation does not affect the temperature profile (clouds are formed by photochemical reactions, see Sect. 1.1.2). Latent heat is important for the energy transportation in the Earth atmosphere, which has a latent heat energy budget of 80 W/m^2 (Trenberth et al. 2009). The water-ice clouds of Mars have negligible latent heating compared to the radiative effects because of very low amounts of water vapor in the thin atmosphere (Zurek et al. 1992).

The atmosphere of the Earth has a unique thermal structure, the stratosphere, which temperature increases with altitude from ~10 km to ~50 km altitude due to the ozone layer. The ozone layer is located mainly at 20–30 km altitudes, and absorbs 97–99% of solar UV radiation. Ozone layers have also been identified in the Mars and Venus atmospheres. However, the ozone layer of Mars is more than 300 times less dense than that of the Earth (Zurek 1992), while that of Venus is a thousand times less dense (Montmessin et al. 2011).

5.3   Summary and further study

This thesis investigates the Venus upper clouds, from observation to the thermal cooling rate calculation. We merge two codes, the fast line-by-line calculation and a radiative transfer model, and prepare gaseous absorption coefficient databases, which required careful consideration of the high pressure and temperature in the lower atmosphere of Venus. Then we retrieve the upper cloud vertical structure as a function of latitude from observations by Venus Express. Our new results on the upper cloud structure are used as input for the calculation of the thermal flux and cooling rate profile below 100 km altitude. We calculated the thermal radiative forcing as a function of latitude, and evaluate the radiative energy balance in the upper cloud layer and mesosphere by a comparison between the thermal cooling and the solar heating. We can summarize the results as follows:

1. The first part of the thesis (Chapter 2) focuses on the retrieval of the upper cloud structure through a new technique, a joint analysis of data from the radio science experiment VeRa and thermal IR spectrometer VIRTIS onboard Venus Express (Lee et al. 2012). We retrieve the cloud top altitude and the aerosol scale height. The thermal emission in the 4.4–5.0 μm wavelength rage has been considered for this analysis.

   - Our research reveals that the cloud top altitude and the aerosol scale height tend to decrease with increasing latitude. The cloud top altitude decreases

from ~68 km at low latitudes to ~62 km at the pole, and the aerosol scale height changes from ~4 km to ~1–2 km in poleward direction.

- At the cold collar, a peculiar cloud top structure is necessary to reproduce the spectral inversion as observed. Here, the cloud tops are located at the temperature minimum of the inversion layer (~62–63 km), with a sharp cloud top boundary (H<1–2 km).

- A comparison of our results with observations at 8.2 μm wavelength (Zasova et al. 2007) indicates a larger mean size for the aerosol particles in the upper cloud layer at high latitudes.

2. The second part of the thesis (Chapters 3 and 4) investigates the role of clouds in the radiative energy balance in the Venus atmosphere. We focus in particular on thermal IR fluxes and cooling rate calculations using the latitude dependent model for the upper cloud from Chapter 2. The upward and downward thermal IR flux profiles are calculated in a broad band (50–2590 cm^{-1} or 3.86–200.0 μm).

- The cloud top altitude affects the outgoing flux at low latitudes, but the sensitivity of outgoing flux to the cloud top altitude decreases towards the pole due to the temperature structure. The latitudinal distribution of the outgoing flux shows a minimum (137 W/m^2) at the cold collar and increases to 161 W/m^2 at the equator and 164 W/m^2 at the pole.

- The cooling rate at the cloud top is ~6 K/day at low latitudes, and increases to ~10 K/day at the pole due to thermal structure and decreasing aerosol scale height with latitude. The small aerosol scale height results in a strong cooling rate at the cloud top.

- Thermal warming happens at the cloud base (~1 K/day) and at the base of the upper cloud layer (1–4 K/day), while thermal cooling happens near the tops of each cloud layer, particularly strong near the top of the upper cloud layer (>5 K/day).

3. We compare the thermal cooling rate from this study with the solar heating rate from Tomasko et al. (1985) to find the latitudinal distribution of net radiative forcing. Our results support the existence of general circulation from the equator to the pole, a Hadley-like cell, to compensate for the radiative energy unbalance.

Further studies will include the following:

1. New calculations of the solar heating rate based on the same thermal structure and cloud top structures as used in those of the thermal cooling rate. It is because of that the solar heating rate from Tomasko et al. (1985) is derived from different temperature fields and cloud top structures. A more accurate net radiative forcing can be evaluated for various cloud top structures.

2. Studies of the relation between the radiative energy balance, the cloud opacity variability, and atmospheric dynamics:

- How much radiative forcing can result from the various opacity distributions of the middle and lower clouds? We can use the same calculation methods to consider diverse optical depths and vertical ranges of the lower and middle cloud layers, which can change the strength of thermal warming and its location within the clouds.

- The net radiative forcing suggests a global sized circulation. Will it be possible to estimate solar energy deposition for various clouds top structures? Since the absorbed solar energy at the cloud tops supports the superrotation and the polar vortex, the solar heating distribution requires further study to understand the energy unbalance at the cloud top altitudes.

A   The spherical harmonics discrete ordinate method (SHDOM)

SHDOM is an algorithm, which is developed by Evans (1998), to solve the radiative transfer equation in three dimensions media. It combines two methods; spherical harmonics for computing the source functions and discrete ordinate method for integrating transfer equations spatially. [The following is an excerpt from Evans (1998)]. A method of finding solution is a Picard iteration in the following four steps: 1) the spherical harmonics source function is transformed to discrete ordinates, 2) the source function is integrated to obtain the radiance field, 3) the radiance field is transformed to spherical harmonics, and 4) the source function is computed from the radiance field in spherical harmonics.

$$I(s) = \exp\left[-\int_0^s k(s')ds'\right]I(0) + \int_0^s \exp\left[-\int_{s'}^s k(t)dt\right]J(s')k(s')ds', \qquad (A.1)$$

is the integral form of the radiative transfer equation which is used to calculate the radiance I along the discrete ordinates from the source function J with distance s, in the 2) step. The volume extinction coefficient k and the source function product (Jk) are approximated linear in distance s across a grid cell.

Although discrete ordinate method is good for representing the streaming of radiation, using spherical harmonics gives efficient computing for the scattering integral in the radiative transfer equation, and requires less storage than pure discrete ordinate approach. Another innovation of SHDOM is an adaptive grid cell, which provides extra resolution where they are most needed. A regular base grid is defined at the start, and grid cells may be split into half to achieve higher spatial resolution, and even extra cells may be split to make a 'smoother' adaptive grid, as the iterative solution method proceeds. The criterion for dividing is based on the change of the source function across a cell. The tree structure is used for the adaptive data structure starting at each base grid.

SHDOM can perform 1D, 2D, and 3D unpolarized radiative transfer with general medium properties. The medium properties are specified at every grid point. The source of radiation may be collimated solar and/or thermal emission. The horizontal boundary conditions may be either periodic or open. The output consists of radiance, hemispheric flux, net flux, or net flux convergence.

B   Atmospheric structure

Table B.1: The atmospheric structure model of the deep atmosphere from VIRA (0–32 km) for all latitudes.

Alt (km)	T (K)	P (mbar)	Alt (km)	T (K)	P (mbar)	Alt (km)	T (K)	P (mbar)
0	735.3	92100	11	650.6	44160	22	564.3	19170
1	727.7	86450	12	643.2	41120	23	556.0	17660
2	720.2	81090	13	635.5	38260	24	547.5	16250
3	712.4	76010	14	628.1	35570	25	539.2	14930
4	704.6	71200	15	620.8	33040	26	530.7	13700
5	696.8	66650	16	613.3	30660	27	522.3	12560
6	688.8	62350	17	605.2	28430	28	513.8	11490
7	681.1	58280	18	597.1	26330	29	505.6	10500
8	673.6	54440	19	589.3	24360	30	496.9	9581.0
9	665.8	50810	20	580.7	22520	31	488.3	8729.0
10	658.2	47390	21	572.4	20790	32	479.9	7940.0

Table B.2: The models of three latitudinal bins (above 32 km altitude): polar region (85–90°S), the cold collar (60–65°S), and low latitude (15–20°S). VeRa and VIRA are combined in this table (Sect. 3.1.1).

Alt (km)	85–90°S		60–65°S		15–20°S	
	T (K)	P (mbar)	T (K)	P (mbar)	T (K)	P (mbar)
33	470.2	7210.0	471.7	7211.0	471.7	7211.0
34	461.5	6534.0	463.4	6537.0	463.4	6537.0
35	452.6	5911.0	455.0	5916.0	455.5	5917.0
36	443.7	5336.0	446.7	5344.0	448.0	5346.0
37	434.8	4808.0	438.5	4819.0	439.9	4822.0
38	426.0	4323.0	430.4	4337.0	432.5	4342.0
39	416.8	3878.0	422.0	3896.0	425.1	3903.0
40	407.8	3471.0	414.2	3492.0	417.6	3501.0
41	399.2	3099.0	406.4	3123.0	410.0	3135.0
42	390.4	2760.0	399.4	2788.0	403.5	2802.0
43	381.8	2452.0	391.4	2483.0	397.1	2499.0
44	372.7	2173.0	384.5	2208.0	391.2	2226.0
45	363.4	1919.0	377.7	1959.0	385.4	1979.0

Continued on Next Page. . .

Table B.2 – Continued

Alt (km)	85–90°S		60–65°S		15–20°S	
	T (K)	P (mbar)	T (K)	P (mbar)	T (K)	P (mbar)
46	354.0	1690.0	370.7	1733.0	379.7	1756.0
47	345.5	1490.3	363.8	1537.7	373.1	1562.3
48	336.8	1304.3	356.9	1355.0	366.0	1381.3
49	324.9	1098.9	348.3	1158.2	357.1	1190.5
50	312.5	914.36	339.0	981.34	347.7	1018.5
51	299.6	749.05	329.0	822.87	338.3	864.36
52	289.4	636.07	320.1	709.58	330.4	750.48
53	279.1	540.38	310.3	612.57	320.7	650.93
54	268.8	456.26	300.5	526.32	310.7	562.10
55	257.9	382.64	290.4	449.91	300.4	483.00
56	247.6	318.52	280.3	382.45	290.0	412.84
57	240.7	264.46	270.0	323.20	281.9	351.07
58	235.2	220.57	259.4	271.28	275.7	297.27
59	236.2	182.26	248.6	226.03	270.2	250.85
60	238.3	149.14	237.6	186.80	265.0	210.99
61	239.8	120.56	228.9	153.12	258.8	176.76
62	239.7	98.572	221.0	124.85	253.7	147.56
63	242.8	81.497	215.7	100.71	249.6	122.73
64	241.8	67.516	213.8	81.343	246.2	101.79
65	241.8	55.501	216.5	65.336	245.0	84.288
66	240.7	45.618	221.8	52.878	243.3	69.746
67	240.0	37.601	226.2	43.020	238.2	57.547
68	238.5	30.985	227.4	35.053	235.5	47.310
69	238.9	25.515	227.7	28.593	233.1	38.819
70	236.7	21.010	226.1	23.312	228.3	31.745
71	233.8	17.258	225.8	18.998	225.3	25.881
72	231.9	14.141	228.2	15.486	221.6	21.024
73	230.6	11.574	227.3	12.638	219.2	17.048
74	228.9	9.4622	224.9	10.299	214.7	13.768
75	226.1	7.7314	221.8	8.3734	210.5	11.085
76	223.6	6.2872	218.4	6.7859	205.9	8.8753
77	221.5	5.0906	214.9	5.4820	203.0	7.0664
78	218.6	4.1279	210.7	4.3852	200.5	5.6175
79	215.5	3.3403	206.7	3.5232	197.2	4.4499
80	212.1	2.6724	203.0	2.8221	193.4	3.5093
81	208.7	2.1564	199.6	2.2185	189.9	2.7533
82	206.0	1.7125	197.1	1.7675	187.3	2.1534
83	203.8	1.3671	195.1	1.3889	185.6	1.6791
84	201.3	1.0837	192.4	1.0912	184.0	1.3128
85	196.6	0.85816	189.5	0.85454	181.7	1.0172
86	191.7	0.67631	186.3	0.66593	178.8	0.77714
87	187.3	0.52497	182.6	0.51814	175.4	0.60016

Continued on Next Page. . .

Table B.2 – Continued

Alt (km)	85–90°S		60–65°S		15–20°S	
	T (K)	P (mbar)	T (K)	P (mbar)	T (K)	P (mbar)
88	183.8	0.41086	179.6	0.39929	172.7	0.45985
89	181.7	0.31445	177.7	0.30808	171.1	0.34738
90	180.1	0.24431	177.1	0.23537	171.1	0.26399
91	178.0	0.18729	177.7	0.18088	171.6	0.19999
92	178.3	0.14308	179.1	0.13772	172.0	0.15251
93	179.6	0.11100	181.6	0.10602	173.3	0.11598
94	181.9	0.08269	184.5	0.08107	176.3	0.08827
95	188.4	0.06530	188.6	0.06273	181.2	0.06795
96	196.5	0.05006	194.1	0.04915	187.4	0.05215
97	199.6	0.03728	198.6	0.03572	195.3	0.04094
98	198.3	0.02149	198.2	0.02211	198.7	0.03059
99	197.6	0.00925	198.1	0.01164	200.4	0.02050

C Flux spectra calculated from the Planck function

The Planck theory gives the thermal emission B_λ (radiance, W/m^2/m/ster) at θ (temperature, K) and λ (wavelength, m) with

$$B_\lambda(\theta) = \frac{C_1 \lambda^{-5}}{\pi(\exp(C_2/\lambda\theta) - 1)} \qquad \text{(C.1)}$$

where $C_1 = 2\pi hc^2 = 3.741832 \times 10^{-16}$ W/m^2 and h is the Planck's constant, and $C_2 = hc/k = 1.4387863 \times 10^{-2}$ mK and k is the Boltzmann's constant (Goody and Yung 1989).
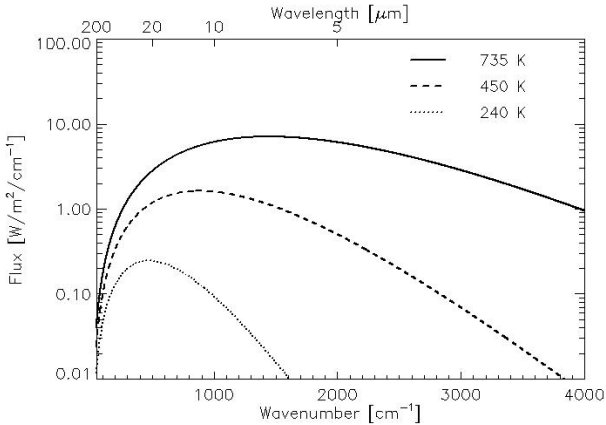

Figure C.1: Flux spectrum calculated from the Planck function (Eq. C.1). Temperatures are selected based on the Venus atmosphere. 735 K is the surface temperature (solid line), 450 K is the value at ~35 km (dashed), and 240 K is near to the cloud top (dotted). Radiance is multiplied by π to get the flux, under the assumption of an isotropic emission.

The equation is also used to convert a radiance to a brightness temperature (T_B)

$$T_B = \left(\frac{C_2}{\lambda}\right) \cdot \left(\ln\left(\frac{C_1 \lambda^{-5}}{B_\lambda \pi} + 1\right)\right)^{-1}. \qquad \text{(C.2)}$$

It should be noted that the brightness temperature (T_B) is widely used due to its convenience which helps to estimate the altitude level of emission, however, it cannot give the information of energy amount at a given wavelength.

Figure C.1 shows energy distributions as a function of wavenumber and temperature (wavelength unit is indicated in the upper label). The emission energy decreases logarithmically with temperatures. 735 K, 450 K, and 240 K correspond to the surface, ~35 km altitude, and around the cloud top, respectively. The decreasing temperature profile with altitude shifts the peak location of emission energy from large to small wavenumber. The 1000–2000 cm^{-1} wavenumber range emits the strongest thermal emission flux at the surface temperature, and then decreases three orders of magnitude at the cloud top temperature. The 300–500 cm^{-1} wavenumber range emits most thermal emission at the temperature of the cloud tops. The thermal emission is wavenumber and temperature dependent, and results in the different slopes of thermal fluxes as shown in Figs. 4.2 and 4.3 in Chapter 4. Since the surface emits the largest energy in the 1000–2000 cm^{-1} range and quickly decreases with altitude due to temperature, the flux profile at the 1600–1610 cm^{-1} wavenumber range has the steepest decline slope, from ~70 W/m^2 to less than 0.01 W/m^2. The slope is much less at the 250–260 cm^{-1} wavenumber range relatively, which decreases only one order of magnitude, from ~10 W/m^2 at surface to ~2 W/m^2 at cloud top.

D   The effects of temperature and CO$_2$ emissions to the cooling rate profile

The cooling rate depends on both cloud structure and temperature profile, which is followed by CO$_2$ emission. The cooling rate profile for model *L-Z71H40* in Fig. D.1(b) shows that there are three small peaks at around 65, 70, and 75 km altitudes. These humps are shown in Fig. 4.13 (Chapter 4.1.3). These little peaks of the cooling rate are related to the temperature perturbations and CO$_2$ emissions.

Firstly, three altitudes of cooling rate humps overlap with the temperature fluctuations. Figure D.1(a) compares the observed temperature profile at low latitude and a linear temperature profile, which has a constant lapse rate. The observed temperature shows fluctuations at the same altitudes as the little peaks of the cooling rates for *L-Z71H40*. To identify the temperature effect, two cases are compared: the observed temperature profile with clouds (*L-Z71H40*) and the linear temperature profile with the same clouds (*C1*).

<div align="center">(a)</div>

<div align="center">(b)</div>
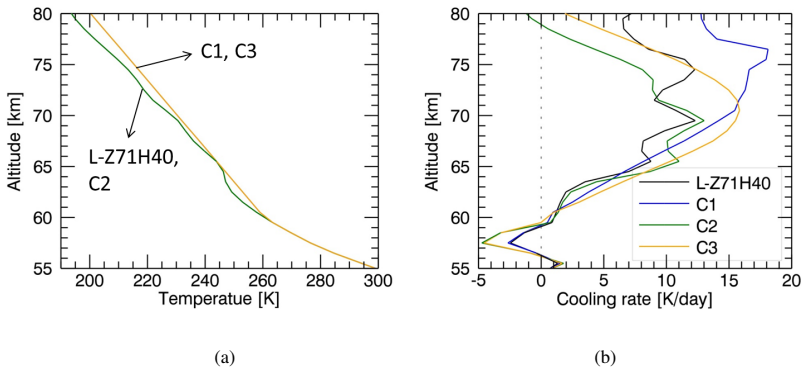
Figure D.1: (a) The temperature profiles: (green) the observed temperature profile at 25°–30°S latitudes and (yellow) the linear temperature profile that connectes temperatures at 60 km and 85 km altitudes. (b) Cooling rate profiles from different conditions. (black) *L-Z71H40* is calculated for the observed temperature profile with clouds, (blue) *C1* is for the linear temperature profile with clouds, (green) *C2* is for the observed temperature profile with clouds but without gases, and (orange) *C3* is for the linear temperature profile with clouds but without gases. All cases use the same cloud top structure (Z = 71 km and H = 4.0 km).
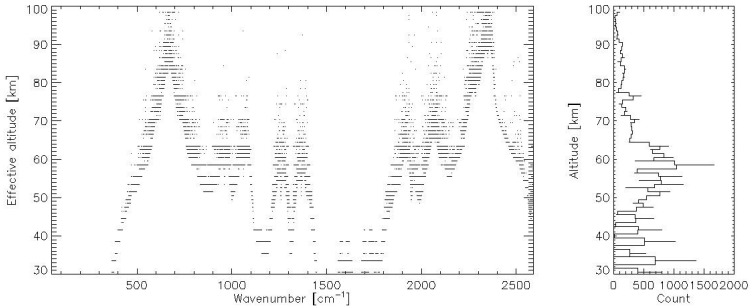
Figure D.2: (Left) the peak altitudes of the CO_2 weighting function for the linear temperature profile, as shown in Fig. D.1(a), assumed 96.5% CO_2 composition. (Right) the vertical number counting of the peak altitudes over all wavenumbers (from the (left) figure).

The linear temperature profile (*C1*) removes two little peaks at around 65 km and 70 km (more discussion about the peak at 76 km altitude is followed).

Secondly, the 76–77 km altitude range is one of the most effective emission altitudes of CO_2 for the linear temperature profile. The weighting function (w) of CO_2 absorption is calculated to get the information of CO_2 emission altitude. It is defined as the vertical derivative of the transmittance ($T_{trans} = e^{-\tau}$) of the overlying layer, and represents the radiative contribution from a layer (Wallace and Hobbs 2006)

$$w = \frac{dT_{trans}}{dz}. \tag{D.1}$$

The level of main radiance contribution ('effective altitude') can be derived as the maximum of the weighting function. It has been used as a remote sensing technique (Schofield and Taylor 1983, Zasova et al. 1999, Wilson et al. 1981, Haus and Arnold 2010) to find the most influence altitude of thermal emissions. Figure D.2 shows the spectrum of effective altitudes of CO_2 absorption for the linear temperature profile. The number of counts of the effective altitudes is shown in Fig. D.2(right), and reveals that it has also little peak at ~76–77 km altitudes. This altitude is the same location of the little peak of *C1* (Fig. D.1(b)). *C3* demonstrates a gas-free condition, but the same clouds and the same linear temperature profile is used as *C1*. The cooling rate of *C3* shows smooth curve, with only one peak caused by the cloud top (71 km).

Additional *C2* case is tested. *C2* is calculated for the observed temperature profile with the same clouds, but for gas-free condition. Figure D.1(b) shows that *C2* still has two little humps at around 65 and 70 km altitudes, and reduced little hump at ~75 km altitude. The reduced cooling rate peak at 75 km in *C2* may be related to the lack of CO_2, because the effective altitudes is changeable according to the temperature structure and the number of counts of effective altitudes shows the little peak at around 75 km for the observed temperature profile. The CO_2 absence in *C2* results in the reduced cooling rate peak at 75 km altitude. Therefore, the comparison of models *L-Z71H40*, *C1*, *C2*, and *C3*

implies that the analysis of cooling rate profile requires a care on the temperature profile and CO_2 emissions.

Bibliography

Allen, C. W., 1964, Astrophysical Quantities, Athlone Press, London, 2nd edn.

Allen, D. A., Crawford, J. W., 1984, Cloud structure on the dark side of Venus, Nature, 307, 222–224

Armstrong, B., 1967, Spectrum line profiles: The Voigt Function, Journal of Quantitative Spectroscopy and Radiative Transfer, 7, 61 – 88, ISSN 0022-4073

Barabash, S., Sauvaud, J.-A., Gunell, H., Andersson, H., Grigoriev, A., Brinkfeldt, K., Holmström, M., Lundin, R., Yamauchi, M., Asamura, K., Baumjohann, W., Zhang, T. L., Coates, A. J., Linder, D. R., Kataria, D. O., Curtis, C. C., Hsieh, K. C., Sandel, B. R., Fedorov, A., Mazelle, C., Thocaven, J.-J., Grande, M., Koskinen, H. E. J., Kallio, E., Säles, T., Riihela, P., Kozyra, J., Krupp, N., Woch, J., Luhmann, J., McKenna-Lawlor, S., Orsini, S., Cerulli-Irelli, R., Mura, M., Milillo, M., Maggi, M., Roelof, E., Brandt, P., Russell, C. T., Szego, K., Winningham, J. D., Frahm, R. A., Scherrer, J., Sharber, J. R., Wurz, P., Bochsler, P., 2007, The Analyser of Space Plasmas and Energetic Atoms (ASPERA-4) for the Venus Express mission, Planetary and Space Science, 55, 1772–1792

Bertaux, J.-L., Nevejans, D., Korablev, O., Villard, E., Quémerais, E., Neefs, E., Montmessin, F., Leblanc, F., Dubois, J., Dimarellis, E., Hauchecorne, A., Lefèvre, F., Rannou, P., Chaufray, J., Cabane, M., Cernogora, G., Souchon, G., Semelin, F., Reberac, A., Van Ransbeek, E., Berkenbosch, S., Clairquin, R., Muller, C., Forget, F., Hourdin, F., Talagrand, O., Rodin, A., Fedorova, A., Stepanov, A., Vinogradov, I., Kiselev, A., Kalinnikov, Y., Durry, G., Sandel, B., Stern, A., Gérard, J., 2007, SPICAV on Venus Express: Three spectrometers to study the global structure and composition of the Venus atmosphere, Planetary and Space Science, 55, 1673–1700, ISSN 0032-0633

Bézard, B., Tsang, C. C. C., Carlson, R. W., Piccioni, G., Marcq, E., Drossart, P., 2009, Water vapor abundance near the surface of Venus from Venus Express/VIRTIS observations, Journal of Geophysical Research (Planets), 114, E00B39

Brown, L. R., Humphrey, C. M., Gamache, R. R., 2007, CO_2-broadened water in the pure rotation and ν_2 fundamental regions, Journal of Molecular Spectroscopy, 246, 1–21

Bullock, M. A., 1997, The Stability of Climate on Venus, Ph.D. thesis, University of Colorado at Boulder

Bullock, M. A., Grinspoon, D. H., 2001, The Recent Evolution of Climate on Venus, Icarus, 150, 19–37

Burch, D. E., Gryvnak, D. A., Patty, R. R., Bartky, C. E., 1969, Absorption of Infrared Radiant Energy by CO_2 and H_2O. IV. Shapes of Collision-Broadened CO_2 Lines, Journal of the Optical Society of America (1917-1983), 59, 267

Cardesín Moinelo, A., 2010, Study and Implementation of the End-to-End Data Pipeline for the Virtis Imaging Spectrometer Onboard Venus Express: "From Science Operations Planning to Data Archiving and Higher Lever Processing", Ph.D. thesis, Università degli Studi di Padova

Cardesín Moinelo, A., Piccioni, G., Migliorini, A., Drossart, P., 2008, Global Mapping of Venus' Atmosphere Using Accumulated Projections of Virtis Venus Express Observations, AGU Fall Meeting Abstracts, p. A4

Carlson, R. W., Baines, K. H., Kamp, L. W., Weissman, P. R., Smythe, W. D., Ocampo, A. C., Johnson, T. V., Matson, D. L., Pollack, J. B., Grinspoon, D., 1991, Galileo infrared imaging spectroscopy measurements at Venus, Science, 253, 1541–1548

Carlson, R. W., Kamp, L. W., Baines, K. H., Pollack, J. B., Grinspoon, D. H., Encrenaz, T., Drossart, P., Taylor, F. W., 1993, Variations in Venus cloud particle properties: A new view of Venus's cloud morphology as observed by Galileo Near-Infrared Mapping Spectrometer, Planetary and Space Science, 41, 477–485

Chapman, S., 2007, Fortran 95/2003 for scientists and engineers, McGraw-Hill Science/Engineering/Math, 3rd edn., ISBN 9780073191577

Colin, L., 1983, Basic facts about Venus, in Venus, (Ed.) Hunten, D. M. and Colin, L. and Donahue, T. M. and Moroz, V. I., pp. 10–26, The University of Arizona Press, Tucson

Crisp, D., 1986, Radiative forcing of the Venus mesosphere. I - Solar fluxes and heating rates, Icarus, 67, 484–514

Crisp, D., 1989, Radiative forcing of the Venus mesosphere. II - Thermal fluxes, cooling rates, and radiative equilibrium temperatures, Icarus, 77, 391–413

Crisp, D., Titov, D., 1997, The Thermal Balance of the Venus Atmosphere, in Venus II: Geology, Geophysics, Atmosphere, and Solar Wind Environment, (Ed.) S. W. Bougher and D. M. Hunten and R. J. Phillips, pp. 353–384, The University of Arizona Press, Tucson

Crisp, D., McMuldroch, S., Stephens, S. K., Sinton, W. M., Ragent, B., Hodapp, K.-W., Probst, R. G., Doyle, L. R., Allen, D. A., Elias, J., 1991, Ground-based near-infrared imaging observations of Venus during the Galileo encounter, Science, 253, 1538–1541

Cruikshank, D. P., 1983, The development of studies of Venus, in Venus, (Ed.) Hunten, D. M., Colin, L., Donahue, T. M., & Moroz, V. I., pp. 1–9, The University of Arizona Press, Tucson

de Bergh, C., Moroz, V. I., Taylor, F. W., Crisp, D., Bézard, B., Zasova, L. V., 2006, The composition of the atmosphere of Venus below 100 km altitude: An overview, Planetary and Space Science, 54, 1389–1397

de Pater, I., Lissauer, J. J., 2001, Planetary Sciences, Cambridge University Press, Cambridge, UK, ISBN 0521482194

Drossart, P., Piccioni, G., Adriani, A., Angrilli, F., Arnold, G., Baines, K. H., Bellucci, G., Benkhoff, J., Bézard, B., Bibring, J.-P., Blanco, A., Blecka, M. I., Carlson, R. W., Coradini, A., di Lellis, A., Encrenaz, T., Erard, S., Fonti, S., Formisano, V., Fouchet, T., Garcia, R., Haus, R., Helbert, J., Ignatiev, N. I., Irwin, P. G. J., Langevin, Y., Lebonnois, S., Lopez-Valverde, M. A., Luz, D., Marinangeli, L., Orofino, V., Rodin, A. V., Roos-Serote, M. C., Saggin, B., Sanchez-Lavega, A., Stam, D. M., Taylor, F. W., Titov, D., Visconti, G., Zambelli, M., Hueso, R., Tsang, C. C. C., Wilson, C. F., Afanasenko, T. Z., 2007, Scientific goals for the observation of Venus by VIRTIS on ESA/Venus express mission, Planetary and Space Science, 55, 1653–1672

Esposito, L. W., Knollenberg, R. G., Marov, M. I., Toon, O. B., Turco, R. P., 1983, The clouds are hazes of Venus, in Venus, (Ed.) Hunten, D. M., Colin, L., Donahue, T. M., & Moroz, V. I., pp. 484–564, The University of Arizona Press, Tucson

Esposito, L. W., Bertaux, J.-L., Krasnopolsky, V., Moroz, V. I., Zasova, L. V., 1997, Chemistry of Lower Atmosphere and Clouds, in Venus II: Geology, Geophysics, Atmosphere, and Solar Wind Environment, (Ed.) S. W. Bougher and D. M. Hunten and R. J. Phillips, pp. 415–458, The University of Arizona Press, Tucson

Esposito, L. W., Stofan, E. R., Cravens, T. E., 2007, Exploring venus: Major scientific issues and directions, in Exploring Venus as a terrestrial planet, (Eds.) L. Esposito, E. R. Stofan, T. E. Cravens, Geophysical monograph series, pp. 1–6, American Geophysical Union, ISBN 9780875904412

Evans, K. F., 1998, The Spherical Harmonics Discrete Ordinate Method for Three-Dimensional Atmospheric Radiative Transfer, Journal of Atmospheric Sciences, 55, 429–446

Fedorova, A., Korablev, O., Vandaele, A.-C., Bertaux, J.-L., Belyaev, D., Mahieux, A., Neefs, E., Wilquet, W. V., Drummond, R., Montmessin, F., Villard, E., 2008, HDO and H_2O vertical distributions and isotopic ratio in the Venus mesosphere by Solar Occultation at Infrared spectrometer on board Venus Express, Journal of Geophysical Research (Planets), 113, E00B22

Fjeldbo, G., Kliore, A. J., Eshleman, V. R., 1971, The neutral atmosphere of Venus as studied with the Mariner V radio occultation experiment, Astronomical Journal, 76, 123–140

Formisano, V., Angrilli, F., Arnold, G., Atreya, S., Baines, K. H., Bellucci, G., Bezard, B., Billebaud, F., Biondi, D., Blecka, M. I., Colangeli, L., Comolli, L., Crisp, D., D'Amore, M., Encrenaz, T., Ekonomov, A., Esposito, F., Fiorenza, C., Fonti, S., Giuranna, M., Grassi, D., Grieger, B., Grigoriev, A., Helbert, J., Hirsch, H., Ignatiev, N., Jurewicz, A., Khatuntsev, I., Lebonnois, S., Lellouch, E., Mattana, A., Maturilli, A., Mencarelli, E., Michalska, M., Lopez Moreno, J., Moshkin, B., Nespoli, F., Nikolsky, Y., Nuccilli, F., Orleanski, P., Palomba, E., Piccioni, G., Rataj, M., Rinaldi, G., Rossi, M., Saggin, B., Stam, D., Titov, D., Visconti, G., Zasova, L., 2006, The planetary fourier spectrometer

(PFS) onboard the European Venus Express mission, Planetary and Space Science, 54, 1298–1314

Free, M., Angell, J. K., 2002, Effect of volcanoes on the vertical temperature profile in radiosonde data, Journal of Geophysical Research (Atmospheres), 107, 4101

Gamache, R., 1995, CO_2-Broadening of Water-Vapor Lines, Journal of Molecular Spectroscopy, 170, 131–151

Gierasch, P. J., Goody, R. M., Young, R. E., Crisp, D., Edwards, C., Kahn, R., Rider, D., del Genio, A., Greeley, R., Hou, A., Leovy, C. B., McCleese, D., Newman, M., 1997, The General Circulation of the Venus Atmosphere: an Assessment, in Venus II: Geology, Geophysics, Atmosphere, and Solar Wind Environment, (Ed.) S. W. Bougher and D. M. Hunten and R. J. Phillips, pp. 459–500, The University of Arizona Press, Tucson

Gilli, G., López-Valverde, M. A., Drossart, P., Piccioni, G., Erard, S., Cardesín Moinelo, A., 2009, Limb observations of CO_2 and CO non-LTE emissions in the Venus atmosphere by VIRTIS/Venus Express, Journal of Geophysical Research (Planets), 114, E00B29

Goody, R. M., Yung, Y. L., 1989, Atmospheric radiation : theoretical basis, Oxford University Press, New York, 2nd edn., ISBN 0195051343

Grassi, D., Drossart, P., Piccioni, G., Ignatiev, N. I., Zasova, L. V., Adriani, A., Moriconi, M. L., Irwin, P. G. J., Negrão, A., Migliorini, A., 2008, Retrieval of air temperature profiles in the Venusian mesosphere from VIRTIS-M data: Description and validation of algorithms, Journal of Geophysical Research (Planets), 113, E00B09

Grassi, D., Migliorini, A., Montabone, L., Lebonnois, S., Cardesìn-Moinelo, A., Piccioni, G., Drossart, P., Zasova, L. V., 2010, Thermal structure of Venusian nighttime mesosphere as observed by VIRTIS-Venus Express, Journal of Geophysical Research (Planets), 115, E09007

Hansen, J., Sato, M., Ruedy, R., Lacis, A., Asamoah, K., Borenstein, S., Brown, E., Cairns, B., Caliri, G., Campbell, M., Curran, B., de Castro, S., Druyan, L., Fox, M., Johnson, C., Lerner, J., McCormick, M., Miller, R., Minnis, P., Morrison, A., Pandolfo, L., Ramberran, I., Zaucker, F., Robinson, M., Russell, P., Shah, K., Stone, P., Tegen, I., Thomason, L., Wilder, J., Wilson, H., 1996, A pinatubo climate modeling investigation, in The Mount Pinatubo eruption: effects on the atmosphere and climate, (Eds.) G. Fiocco, D. Fuà, G. Visconti, N. A. T. O. S. A. Division, NATO ASI series. Series I, Global environmental change ; vol. 42, pp. 233–272, Springer, ISBN 9783540612810

Hansen, J. E., Travis, L. D., 1974, Light scattering in planetary atmospheres, Space Science Review, 16, 527–610

Haus, R., Arnold, G., 2010, Radiative transfer in the atmosphere of Venus and application to surface emissivity retrieval from VIRTIS/VEX measurements, Planetary and Space Science, 58, 1578–1598

Haus, R., Goering, H., 1990, Radiative energy balance of the Venus mesosphere, Icarus, 84, 62–82

Häusler, B., Pätzold, M., Tyler, G. L., Simpson, R. A., Bird, M. K., Dehant, V., Barriot, J.-P., Eidel, W., Mattei, R., Remus, S., Selle, J., Tellmann, S., Imamura, T., 2006, Radio science investigations by VeRa onboard the Venus Express spacecraft, Planetary and Space Science, 54, 1315–1335

Holton, J. R., 1992, An introduction to dynamic meteorology, Academic Press, San Diego, 3rd edn., ISBN 012354355

Ignatiev, N. i., Moroz, V. i., Zasova, L. V., Khatuntsev, I. v., 1999, Water vapour in the middle atmosphere of Venus:An improved treatment of the Venera 15 ir spectra, Planetary and Space Science, 47, 1061–1075

Ignatiev, N. I., Titov, D. V., Piccioni, G., Drossart, P., Markiewicz, W. J., Cottini, V., Roatsch, T., Almeida, M., Manoel, N., 2009, Altimetry of the Venus cloud tops from the Venus Express observations, Journal of Geophysical Research (Planets), 114, E00B43

James, I. N., 1994, Introduction to circulating atmospheres, Cambridge University Press, Cambridge, ISBN 052141895 0521429358

Kahn, R. A., Martin, T. Z., Zurek, R. W., Lee, S. W., 1992, The Martian dust cycle, in Mars, (Ed.) George, M., pp. 1017–1053, The University of Arizona Press, Tucson

Kamp, L. W., Taylor, F. W., 1990, Radiative-transfer models of the night side of Venus, Icarus, 86, 510–529

Kawabata, K., Coffeen, D. L., Hansen, J. E., Lane, W. A., Sato, M., Travis, L. D., 1980, Cloud and haze properties from Pioneer Venus polarimetry, Journal of Geophysical Research, 85, 8129–8140

Kieffer, H. H., Jakosky, B. M., Snyder, C. W., 1992, The planet Mars - From antiquity to the present, in Mars, (Ed.) Kieffer, H. H. and Jakosky, B. M. and Snyder, C. W. and Matthews, M. S., pp. 1–33, The University of Arizona Press, Tucson

Kiehl, J. T., Trenberth, K. E., 1997, Earth's Annual Global Mean Energy Budget., Bulletin of the American Meteorological Society, 78, 197–197

Kliore, A. J., Moroz, V. I., Keating, G. M., 1985, The Venus International Reference Atmosphere, Advances in Space Research, 5

Knollenberg, R. G., Hunten, D. M., 1980, The microphysics of the clouds of Venus - Results of the Pioneer Venus particle size spectrometer experiment, Journal of Geophysical Research, 85, 8039–8058

Kondratev, K. I., 1969, Radiation in the atmosphere, Academic Press, New York

Lee, Y. J., Titov, D. V., Tellmann, S., Piccialli, A., Ignatiev, N., Pätzold, M., Häusler, B., Piccioni, G., Drossart, P., 2012, Vertical structure of the Venus cloud top from the VeRa and VIRTIS observations onboard Venus Express, Icarus, 217, 599–609

Lellouch, E., Clancy, T., Crisp, D., Kliore, A. J., Titov, D., Bougher, S. W., 1997, Monitoring of Mesospheric Structure and Dynamics, in Venus II: Geology, Geophysics, Atmosphere, and Solar Wind Environment, (Ed.) S. W. Bougher and D. M. Hunten and R. J. Phillips, pp. 295–324, The University of Arizona Press, Tucson

Levoni, C., Cervino, M., Guzzi, R., Torricella, F., 1997, Atmospheric aerosol optical properties: a database of radiative characteristics for different components and classes, Applied Optics, 36, 8031–8041

Limaye, S. S., 2007, Venus atmospheric circulation: Known and unknown, Journal of Geophysical Research (Planets), 112, E04S09

Limaye, S. S., Kossin, J. P., Rozoff, C., Piccioni, G., Titov, D. V., Markiewicz, W. J., 2009, Vortex circulation on Venus: Dynamical similarities with terrestrial hurricanes, Geophysical Research Letters, 36, L04204

Loeb, N. G., Wong, T., 2007, Clouds and the earth's radiation budget, in Our changing planet : the view from space, (Ed.) M. D. King, Cambridge University Press, ISBN 9780521828703

Marcq, E., Encrenaz, T., Bézard, B., Birlan, M., 2006, Remote sensing of Venus' lower atmosphere from ground-based IR spectroscopy: Latitudinal and vertical distribution of minor species, Planetary and Space Science, 54, 1360–1370

Markiewicz, W. J., Titov, D. V., Ignatiev, N., Keller, H. U., Crisp, D., Limaye, S. S., Jaumann, R., Moissl, R., Thomas, N., Esposito, L., Watanabe, S., Fiethe, B., Behnke, T., Szemerey, I., Michalik, H., Perplies, H., Wedemeier, M., Sebastian, I., Boogaerts, W., Hviid, S. F., Dierker, C., Osterloh, B., Böker, W., Koch, M., Michaelis, H., Belyaev, D., Dannenberg, A., Tschimmel, M., Russo, P., Roatsch, T., Matz, K. D., 2007a, Venus Monitoring Camera for Venus Express, Planetary and Space Science, 55, 1701–1711

Markiewicz, W. J., Titov, D. V., Limaye, S. S., Keller, H. U., Ignatiev, N., Jaumann, R., Thomas, N., Michalik, H., Moissl, R., Russo, P., 2007b, Morphology and dynamics of the upper cloud layer of Venus, Nature, 450, 633–636

Marov, M. Y., 2005, Mikhail Lomonosov and the discovery of the atmosphere of Venus during the 1761 transit, in IAU Colloq. 196: Transits of Venus: New Views of the Solar System and Galaxy, (Ed.) D. W. Kurtz, pp. 209–219

McGouldrick, K., Toon, O. B., Grinspoon, D. H., 2011, Sulfuric acid aerosols in the atmospheres of the terrestrial planets, Planetary and Space Science, 59, 934–941

Meadows, V. S., Crisp, D., 1996, Ground-based near-infrared observations of the Venus nightside: The thermal structure and water abundance near the surface, Journal of Geophysical Research, 101, 4595–4622

Mills, F. P., Esposito, L. W., Yung, Y. L., 2007, Atmospheric composition, chemistry, and clouds, in Exploring Venus as a terrestrial planet, (Eds.) L. Esposito, E. R. Stofan, T. E. Cravens, Geophysical monograph series, American Geophysical Union, ISBN 9780875904412

Moissl, R., 2008, Morphology and dynamics of the Venus atmosphere at the cloud top level as observed by the Venus monitoring camera, Ph.D. thesis, Technische Universität Carolo-Wilhelmina zu Braunschweig, Germany

Montmessin, F., Bertaux, J.-L., Lefèvre, F., Marcq, E., Belyaev, D., Gérard, J.-C., Korablev, O., Fedorova, A., Sarago, V., Vandaele, A. C., 2011, A layer of ozone detected in the nightside upper atmosphere of Venus, Icarus, 216, 82–85

Moroz, V. I., 2002, Estimates of visibility of the surface of Venus from descent probes and balloons, Planetary and Space Science, 50, 287–297

Moroz, V. I., Ekonomov, A. P., Moshkin, B. E., Revercomb, H. E., Sromovsky, L. A., Schofield, J. T., 1985, Solar and thermal radiation in the Venus atmosphere, Advances in Space Research, 5, 197–232

Moskalenko, N. I., Parzhin, S. N., 1981, Investigation of absorption spectra of carbon dioxide under high pressures. Proceedings of the 6th All-Union Symposium on the Propagation of the Laser Radiation in the Atmosphere, IOA SO AN SSSR, Tomsk, pp. 110–113, in Russian

Owen, T., 1978, Abundances of isotopes in planetary atmospheres, Moon and Planets, 19, 297–303

Pätzold, M., Häusler, B., Bird, M. K., Tellmann, S., Mattei, R., Asmar, S. W., Dehant, V., Eidel, W., Imamura, T., Simpson, R. A., Tyler, G. L., 2007, The structure of Venus' middle atmosphere and ionosphere, Nature, 450, 657–660

Piccialli, A., 2010, Cyclotrophic wind in the mesosphere of Venus from Venus Express observations, Ph.D. thesis, Technische Universität Carolo-Wilhelmina zu Braunschweig, Germany

Piccioni, G., Drossart, P., Cosi, M., Ammannito, E., Berlin, R., occaccini, A., G., B., Bouye, M., Capaccioni, F., Cherubini, G., Dami, M., Dupuis, O., Fave, A., Filacchione, G., Hello, Y., Henry, F., Hofer, S., Huntzinger, G., Melchiorri, R., Parisot, J., Pasqui, C., Peter, G., Pompei, C., Réss, J. M., Semery, A., Soufflot, A., the VIRTIS Co-I team, 2006, VIRTIS: The Visible and Infrared Thermal Imaging Spectrometer, vol. SP-1295, ESA, Noordwijk, The Netherlands

Piccioni, G., Drossart, P., Sanchez-Lavega, A., Hueso, R., Taylor, F. W., Wilson, C. F., Grassi, D., Zasova, L., Moriconi, M., Adriani, A., Lebonnois, S., Coradini, A., Bézard, B., Angrilli, F., Arnold, G., Baines, K. H., Bellucci, G., Benkhoff, J., Bibring, J. P., Blanco, A., Blecka, M. I., Carlson, R. W., di Lellis, A., Encrenaz, T., Erard, S., Fonti, S., Formisano, V., Fouchet, T., Garcia, R., Haus, R., Helbert, J., Ignatiev, N. I., Irwin, P. G. J., Langevin, Y., Lopez-Valverde, M. A., Luz, D., Marinangeli, L., Orofino, V., Rodin, A. V., Roos-Serote, M. C., Saggin, B., Stam, D. M., Titov, D., Visconti, G., Zambelli, M., Ammannito, E., Barbis, A., Berlin, R., Bettanini, C., Boccaccini, A., Bonnello, G., Bouye, M., Capaccioni, F., Cardesin Moinelo, A., Carraro, F., Cherubini, G., Cosi, M., Dami, M., de Nino, M., Del Vento, D., di Giampietro, M., Donati, A., Dupuis, O., Espinasse, S., Fabbri, A., Fave, A., Veltroni, I. F., Filacchione, G.,

Garceran, K., Ghomchi, Y., Giustini, M., Gondet, B., Hello, Y., Henry, F., Hofer, S., Huntzinger, G., Kachlicki, J., Knoll, R., Driss, K., Mazzoni, A., Melchiorri, R., Mondello, G., Monti, F., Neumann, C., Nuccilli, F., Parisot, J., Pasqui, C., Perferi, S., Peter, G., Piacentino, A., Pompei, C., Reess, J.-M., Rivet, J.-P., Romano, A., Russ, N., Santoni, M., Scarpelli, A., Semery, A., Soufflot, A., Stefanovitch, D., Suetta, E., Tarchi, F., Tonetti, N., Tosi, F., Ulmer, B., 2007, South-polar features on Venus similar to those near the north pole, Nature, 450, 637–640

Pollack, J. B., 1967, Rayleigh scattering in an optically thin atmosphere and its application to Martian topography, Icarus, 7, 42–46

Pollack, J. B., Toon, O. B., Boese, R., 1980a, Greenhouse models of Venus' high surface temperature, as constrained by Pioneer Venus measurements, Journal of Geophysical Research, 85, 8223–8231

Pollack, J. B., Toon, O. B., Whitten, R. C., Boese, R., Ragent, B., Tomasko, M., Eposito, L., Travis, L., Wiedman, D., 1980b, Distribution and source of the UV absorption in Venus' atmosphere, Journal of Geophysical Research, 85, 8141–8150

Pollack, J. B., Dalton, J. B., Grinspoon, D., Wattson, R. B., Freedman, R., Crisp, D., Allen, D. A., Bezard, B., de Bergh, C., Giver, L. P., Ma, Q., Tipping, R., 1993, Near-infrared light from Venus' nightside - A spectroscopic analysis, Icarus, 103, 1–42

Press, W. H., Teukolsky, S. A., Vetterling, W. T., Flannery, B. P., 1992, Numerical recipes in FORTRAN. The art of scientific computing, Cambridge University Press, New York, NY, 2nd edn.

Ragent, B., Esposito, L. W., Tomasko, M. G., Marov, M. I., Shari, V. P., 1985, Particulate matter in the Venus atmosphere, Advances in Space Research, 5, 85–115

Ramanathan, V., Cess, R. D., Harrison, E. F., Minnis, P., Barkstrom, B. R., Ahmad, E., Hartmann, D., 1989, Cloud-Radiative Forcing and Climate: Results from the Earth Radiation Budget Experiment, Science, 243, 57–63

Revercomb, H. E., Sromovsky, L. A., Suomi, V. E., Boese, R. W., 1985, Net thermal radiation in the atmosphere of Venus, Icarus, 61, 521–538

Robock, A., 2002, The climatic aftermath, Science, 295, 1242–1244, {http://www.sciencemag.org/content/295/5558/1242.full.pdf}

Rodgers, C. D., Walshaw, C. D., 1966, The computation of infra-red cooling rate in planetary atmospheres, Quarterly Journal of the Royal Meteorological Society, 92, 67–92

Roos-Serote, M., Drossart, P., Encrenaz, T., Lellouch, E., Carlson, R. W., Baines, K. H., Taylor, F. W., Calcutt, S. B., 1995, The thermal structure and dynamics of the atmosphere of Venus between 70 and 90 KM from the Galileo-NIMS spectra, Icarus, 114, 300–309

Rothman, L. S., Rinsland, C. P., Goldman, A., Massie, S. T., Edwards, D. P., Flaud, J.-M., Perrin, A., Camy-Peyret, C., Dana, V., Mandin, J.-Y., Schroeder, J., McCann, A., Gamache, R. R., Wattson, R. B., Yoshino, K., Chance, K., Jucks, K., Brown, L. R., Nemtchinov, V., Varanasi, P., 1998, The HITRAN Molecular Spectroscopic Database and HAWKS (HITRAN Atmospheric Workstation): 1996 Edition, Journal of Quantitative Spectroscopy and Radiative Transfer, 60, 665–710

Rothman, L. S., Gordon, I. E., Barbe, A., Benner, D. C., Bernath, P. F., Birk, M., Boudon, V., Brown, L. R., Campargue, A., Champion, J.-P., Chance, K., Coudert, L. H., Dana, V., Devi, V. M., Fally, S., Flaud, J.-M., Gamache, R. R., Goldman, A., Jacquemart, D., Kleiner, I., Lacome, N., Lafferty, W. J., Mandin, J.-Y., Massie, S. T., Mikhailenko, S. N., Miller, C. E., Moazzen-Ahmadi, N., Naumenko, O. V., Nikitin, A. V., Orphal, J., Perevalov, V. I., Perrin, A., Predoi-Cross, A., Rinsland, C. P., Rotger, M., Šimečková, M., Smith, M. A. H., Sung, K., Tashkun, S. A., Tennyson, J., Toth, R. A., Vandaele, A. C., Vander Auwera, J., 2009, The HITRAN 2008 molecular spectroscopic database, Journal of Quantitative Spectroscopy and Radiative Transfer, 110, 533–572

Sánchez-Lavega, A., Pérez-Hoyos, S., Hueso, R., 2004, Clouds in planetary atmospheres: A useful application of the Clausius-Clapeyron equation, American Journal of Physics, 72, 767–774

Sánchez-Lavega, A., Hueso, R., Piccioni, G., Drossart, P., Peralta, J., Pérez-Hoyos, S., Wilson, C. F., Taylor, F. W., Baines, K. H., Luz, D., Erard, S., Lebonnois, S., 2008, Variable winds on Venus mapped in three dimensions, Geophysical Research Letters, 35, L13204

Schofield, J. T., Taylor, F. W., 1982, Net global thermal emission from the Venusian atmosphere, Icarus, 52, 245–262

Schofield, J. T., Taylor, F. W., 1983, Measurements of the mean, solar-fixed temperature and cloud structure of the middle atmosphere of Venus, Quarterly Journal of the Royal Meteorological Society, 109, 57–80

Schubert, G., 1983, General circulation and the dynamical state of the Venus atmosphere, in Venus, (Ed.) Hunten, D. M., Colin, L., Donahue, T. M., & Moroz, V. I., pp. 681–765, The University of Arizona Press, Tucson

Schubert, G., Bougher, S. W., Covey, C. C., Del Genio, A. D., Grossman, A. S.and Hollingsworth, J. L., Limaye, S. S., Young, R. E., 2007, Venus atmosphere dynamics: A continuing enigma, in Exploring Venus as a terrestrial planet, (Eds.) L. Esposito, E. R. Stofan, T. E. Cravens, Geophysical monograph series, pp. 101–120, American Geophysical Union, ISBN 9780875904412

Seiff, A., 1983, Thermal structure of the atmosphere of Venus, in Venus, (Ed.) Hunten, D. M., Colin, L., Donahue, T. M., & Moroz, V. I., pp. 215–279, The University of Arizona Press, Tucson

Seiff, A., Schofield, J. T., Kliore, A. J., Taylor, F. W., Limaye, S. S., 1985, Models of the structure of the atmosphere of Venus from the surface to 100 kilometers altitude, Advances in Space Research, 5, 3–58

Svedhem, H., Titov, D. V., Taylor, F. W., Witasse, O., 2007, Venus as a more Earth-like planet, Nature, 450, 629–632

Svedhem, H., Titov, D., Taylor, F., Witasse, O., 2009, Venus Express mission, Journal of Geophysical Research (Planets), 114, E00B33

Tanaka, M., Yamanouchi, T., 1977, Absorption properties of the near infrared CO_2 bands, Journal of Quantitative Spectroscopy and Radiative Transfer, 17, 421–432

Taylor, F., Grinspoon, D., 2009, Climate evolution of Venus, Journal of Geophysical Research (Planets), 114, E00B40

Taylor, F. W., 1998, Remote sensing of planetary atmospheres: Venus, Advances in Space Research, 21, 409–418

Taylor, F. W., 2006, Venus before Venus Express, Planetary and Space Science, 54, 1249–1262, ISSN 0032-0633

Taylor, F. W., Crisp, D., Bézard, B., 1997, Near-Infrared Sounding of the Lower Atmosphere of Venus, in Venus II: Geology, Geophysics, Atmosphere, and Solar Wind Environment, (Ed.) S. W. Bougher and D. M. Hunten and R. J. Phillips, pp. 325–352, The University of Arizona Press, Tucson

Tellmann, S., Pätzold, M., Häusler, B., Bird, M. K., Tyler, G. L., 2009, Structure of the Venus neutral atmosphere as observed by the Radio Science experiment VeRa on Venus Express, Journal of Geophysical Research (Planets), 114, E00B36

Titov, D. V., Haus, R., 1997, A fast and accurate method of calculation of gaseous transmission functions in planetary atmospheres, Planetary and Space Science, 45, 369–377

Titov, D. V., Svedhem, H., Koschny, D., Hoofs, R., Barabash, S., Bertaux, J.-L., Drossart, P., Formisano, V., Häusler, B., Korablev, O., Markiewicz, W. J., Nevejans, D., Pätzold, M., Piccioni, G., Zhang, T. L., Merritt, D., Witasse, O., Zender, J., Accomazzo, A., Sweeney, M., Trillard, D., Janvier, M., Clochet, A., 2006, Venus Express science planning, Planetary and Space Science, 54, 1279–1297

Titov, D. V., Bullock, M. A., Crisp, D., Renno, N. O., Taylor, F. W., Zasova, L. V., 2007, Radiation in the Atmosphere of Venus, in Exploring Venus as a terrestrial planet, (Eds.) L. Esposito, E. R. Stofan, T. E. Cravens, Geophysical monograph series, American Geophysical Union, ISBN 9780875904412

Titov, D. V., Taylor, F. W., Svedhem, H., Ignatiev, N. I., Markiewicz, W. J., Piccioni, G., Drossart, P., 2008, Atmospheric structure and dynamics as the cause of ultraviolet markings in the clouds of Venus, Nature, 456, 620–623

Titov, D. V., Markiewicz, W. J., Ignatiev, N. I., Song, L., Limaye, S. S., Sanchez-Lavega, A., Hesemann, J., Almeida, M., Roatsch, T., Matz, K.-D., Scholten, F., Crisp, D., Esposito, L. W., Hviid, S. F., Jaumann, R., Keller, H. U., Moissl, R., 2012, Morphology of the cloud tops as observed by the Venus Express Monitoring Camera, Icarus, 217, 682–701

Tomasko, M. G., Smith, P. H., Suomi, V. E., Sromovsky, L. A., Revercomb, H. E., Taylor, F. W., Martonchik, D. J., Seiff, A., Boese, R., Pollack, J. B., Ingersoll, A. P., Schubert, G., Covey, C. C., 1980, The thermal balance of Venus in light of the Pioneer Venus mission, Journal of Geophysical Research, 85, 8187–8199

Tomasko, M. G., Doose, L. R., Smith, P. H., 1985, The absorption of solar energy and the heating rate in the atmosphere of Venus, Advances in Space Research, 5, 71–79

Tonkov, M. V., Filippov, N. N., Bertsev, V. V., Bouanich, J. P., van-Thanh, N., Brodbeck, C., Hartmann, J. M., Boulet, C., Thibault, F., Le Doucen, R., 1996, Measurements and empirical modeling of pure CO_2 absorption in the 2.3- m region at room temperature: far wings, allowed and collision-induced bands, Applied Optics, 35, 4863–4870

Trenberth, K. E., Fasullo, J. T., Kiehl, J., 2009, Earth's Global Energy Budget, Bulletin of the American Meteorological Society, 90, 311

Wallace, J. M., Hobbs, P. V., 2006, Atmospheric Science, An Introductory Survey, Academic Press, 2nd edn.

Wilson, C. F., Guerlet, S., Irwin, P. G. J., Tsang, C. C. C., Taylor, F. W., Carlson, R. W., Drossart, P., Piccioni, G., 2008, Evidence for anomalous cloud particles at the poles of Venus, Journal of Geophysical Research (Planets), 113, E00B13

Wilson, W. J., Klein, M. J., Kahar, R. K., Gulkis, S., Olsen, E. T., Ho, P. T. P., 1981, Venus. I - Carbon monoxide distribution and molecular-line searches, Icarus, 45, 624–637

Winters, B., Silverman, S., Benedict, W. S., 1964, Line shape in the wing beyond the band head of the 4.3 μ band of CO_2, Journal of Quantitative Spectroscopy and Radiative Transfer, 4, 527–537

Zasova, L. V., Moroz, V. I., Esposito, L. W., Na, C. Y., 1993, SO_2 in the Middle Atmosphere of Venus: IR Measurements from Venera-15 and Comparison to UV Data, Icarus, 105, 92–109

Zasova, L. V., Khatountsev, I. A., Moroz, V. I., Ignatiev, N. I., 1999, Structure of the Venus middle atmosphere: Venera 15 fourier spectrometry data revisited, Advances in Space Research, 23, 1559–1568

Zasova, L. V., Moroz, V. I., Formisano, V., Ignatiev, N. I., Khatuntsev, I. V., 2004, Infrared spectrometry of Venus: IR Fourier spectrometer on Venera 15 as a precursor of PFS for Venus express, Advances in Space Research, 34, 1655–1667

Zasova, L. V., Ignatiev, N., Khatuntsev, I., Linkin, V., 2007, Structure of the Venus atmosphere, Planetary and Space Science, 55, 1712–1728

Zhang, T. L., Baumjohann, W., Delva, M., Auster, H.-U., Balogh, A., Russell, C. T., Barabash, S., Balikhin, M., Berghofer, G., Biernat, H. K., Lammer, H., Lichtenegger, H., Magnes, W., Nakamura, R., Penz, T., Schwingenschuh, K., Vörös, Z., Zambelli, W., Fornacon, K.-H., Glassmeier, K.-H., Richter, I., Carr, C., Kudela, K., Shi, J. K., Zhao, H., Motschmann, U., Lebreton, J.-P., 2006, Magnetic field investigation of the

Venus plasma environment: Expected new results from Venus Express, Planetary and Space Science, 54, 1336–1343

Zurek, R. W., 1992, Comparative aspects of the climate of Mars - an introduction to the current atmosphere, in Mars, (Ed.) George, M., pp. 799–817, The University of Arizona Press, Tucson

Zurek, R. W., Barnes, J. R., Haberle, R. M., Pollack, J. B., Tillman, J. E., Leovy, C. B., 1992, Dynamics of the atmosphere of Mars, in Mars, (Ed.) George, M., pp. 835–933, The University of Arizona Press, Tucson

Acknowledgements

It was possible to manage my studies and PhD thesis through the help of many people. First of all, I deeply appreciate the clear ideas and concrete suggestions of Dr. Titov, my supervisor. The discussions with him motivated me to study more on my research topic. I also appreciate help of Dr. Ignatiev for the data and for discussions, which solved most of my problems. I would like to thank the IMPRS school and the MPI for Solar System Research for providing me the PhD opportunity and the three-year-fellowship to support my stay in Germany. I would like to thank Dr. Schmitt, IMPRS coordinator, for his consideration and help. My PhD course was possible thanks to Prof. Hördt, and I would like to thank him for accepting me as his PhD student in TU Braunschweig. I appreciate Prof. Sánchez-Lavega in Bilbao, Spain, for being the second referee of my thesis, and Prof. Glassmeier and Dr. Narita for becoming members of my thesis committee.

This work is based on observational data and modeling calculations. Therefore, I deeply thank Dr. Tellmann, Prof. Pätzold, Dr. Piccioni and Dr. Drossart for providing their data from VeRa and VIRTIS/Venus Express. I am very thankful to Dr. Piccialli for her help at my starting point. I thank Dr. Evans for helpful responses to my questions on the SHDOM model. Scientific stimulation is another big factor to keep interest in my research topic. For this, I am grateful to Dr. Markiewicz for showing his interest in my work and for giving kind help. I thank the Venus group in MPS for the great stimulation by presenting new results and methods during group meetings. I thank Dr. Rengel for being my thesis advisory commission member and for her support. Many friends helped me for writing my thesis as well. I am deeply grateful to Dr. Schröder for reading most of my thesis patiently and for helpful discussions, also I thank Dr. Bugiolacchi, Dr. Machtoub, Dr. Tiwari, Peter, and Lúcia for reading each chapter.

My dear friends in Lindau solved my stress from works and problems, and filled me with joy. I sincerely thank all of them for their kindness, especially the Yamada family, Li, Megha, and Supriya for their care during my starting time. Many parties, organized by Philippe and many others, were good time to know people, and thanks for all these opportunities. Thanks to Wieland for organizing football playing, which I enjoyed a lot after coming to Germany, Antoine for nice experiences in India and Paris, and Neda for her steady warm greetings. Compared to the exciting first year, the second and third years were a period of deepening life in Lindau. I deeply grateful for the sincere support from many friends; Elena and Thomas for great times of dinners and parties together, Sebastian for organizing board game plays, Juanjo and Maria for enjoyable trips, my wonderful office mates, Peter and Nagaraju, for making a good atmosphere in our office, Oksana and Zhenya for their kind care, Kumiko for her tranquil mood which I'd like to learn, Takeshi for showing his talent of cooking, Navdeep for her great cheers and tea times which released me from the strong tension of the PhD study, Lucia for her considerations

Curriculum Vitae

Persönliche Daten

Name	Yeon Joo Lee
Geburtsdatum	02. April 1983
Geburtsort	Seoul, Republik Korea
Staatsangehörigkeit	Koreanisch

Studium

2006   B.S. in Atmosphärenforschung,
Yonsei Universität, Seoul, Republik Korea

2008   M.S. in Atmosphärenforschung,
Yonsei Universität, Seoul, Republik Korea

2009–2012   Promotion,
MPI für Sonnensystemforschung, Katlenburg-Lindau
TU Carolo-Wilhelmina zu Braunschweig, Braunschweig
Germany

Berufserfahrung

2007–2008   Wissenschaftliche Mitarbeiterin für das Ozonüberwachungsprogramm,
Yonsei Uni. (WMO Global Ozone Observing System #252)
Korea Meteorological Administration, Republik Korea

07–09/2008   Wissenschaftliche Mitarbeiterin für
die Machbarkeitsstudie des 'Earth environment satellite',
Ministerium für Umwelt, Republik Korea